Investigation of the nonlinear phase of edge-localized-modes on the DIII-D tokamak

Matthias Knölker

München 2019

Investigation of the nonlinear phase of edge-localized-modes on the DIII-D tokamak

Matthias Knölker

Dissertation
an der Fakultät für Physik
der Ludwig-Maximilians-Universität
München

vorgelegt von
Matthias Knölker
aus Bergisch Gladbach

München, den 25.01.2019

durchgeführt am DIII-D Tokamak der Firma General Atomics in San Diego, CA, USA

Dissertation

an der Fakultät für Physik
der Ludwig-Maximilians-Universität München
vorgelegt von Matthias Knölker
am 25.Januar 2019

Erstgutachter: Prof. Dr. Hartmut Zohm
Zweitgutachter: Prof. Dr. Harald Lesch

Tag der mündlichen Prüfung: 24. April 2019

Der Blick über die Welt hinaus ist der einzige, der die Welt versteht.

Only the glance beyond the world understands the world.

Richard Wagner

Zusammenfassung

Als eine der Herausforderungen künftiger Kernfusionskraftwerke gelten sogenannte Edge localized modes (ELMs). Bei diesen Störungen am Plasmarand handelt es sich um magnetohydrodynamische Instabilitäten, die zum Teilchen- und Energieauswurf aus dem heißen und eingeschlossenen Plasma führen. Einerseits tragen sie so zur Dichtekontrolle und zum Abtransport von Verunreinigungen, wie der Heliumasche, aus der Kernzone des Plasmas bei, andererseits verschlechtern sie den Plasmaeinschluss und können zu Erosion und partiellem Schmelzen der exponierten Komponenten (vor allem des Divertors) führen. Daher ist es von großer Relevanz, die Ursache und den Verlauf von ELMs besser zu verstehen. Zwar wurde die Verkleinerung und völlige Unterdrückung von ELMs auf mehreren Forschungsanlagen demonstriert und Reaktorszenarien ohne ELMs entwickelt, jedoch sind all diese nur unter bestimmten operationellen Voraussetzungen realisierbar. Es gilt somit als fraglich, ob sie uneingeschränkt auf die gerade in Frankreich im Bau befindliche ITER Anlage oder künftige Fusionskraftwerke übertragbar sind. Während die lineare ELM Phase, d.h. das Auftreten der Instabilität, gut durch das so genannte Peeling-Ballooning-Modell erklärt werden kann, sind noch viele Fragen im Bereich der nichtlinearen ELM Dynamik offen, die im Fokus dieser Arbeit stehen, wie beispielsweise Größe und Verlauf.

Mittels Infrarotthermografie, Röntgenstrahlapparaturen und Magnetspulen werden ELM-Ausbrüche auf dem DIII-D Tokamak charakterisiert und in einer Datenbank katalogisiert. Mit ihrer Hilfe wird der Einfluss von Parametern am Plasmarand (wie Druck und Temperatur) auf die Wärmebelastung am Divertor untersucht und mit gegenwärtigen Modellen verglichen. Dabei kann neben bisher bekannten vor allem die Nähe zur LH-Schwelle (nötige Heizleistung um die H-mode zu erreichen, einen Operationsmodus mit verbessertem Teilcheneinschluss) als entscheidender Faktor ermittelt werden. Im schwellennahen Operationsgebiet, das auch für ITER vorgesehen ist, sinkt die Frequenz der ELMs und ihre Größe nimmt zu. Dies kann zu hoher Divertorbelastung führen und damit einem Trend, der nicht von den Modellen erwartet wird. Mit Hilfe linearer Stabilitätsanalyse wird zudem eine inverse Proportionalität zwischen der Modenzahl und der ELM Energiedichte (Zeitintegral des Wärmeflusses) nachgewiesen.

Während der ELMs fließen Ströme in die Divertorziegel, die mit Hilfe einer dafür installierten Diagnostik gemessen werden. Diese Ströme oszillieren zu Beginn der nichtlinearen Phase und weisen eine beachtliche Stärke auf. Die Amplitude der Stromstärke weist geringe Korrelation mit der ELM Größe auf. Ein Modell zur Erklärung dieser Ströme basierend auf thermoelektrischen Effekten wird entwickelt, das im Stromfluss durch den Plasmarand eine Ursache für das explosive Wachstum der Instabilität ausmacht. Modellvorhersagen der Spitzenströme stimmen mit den experimentellen Messergebnissen überein. Wenn Dynamik und zeitlicher Verlauf der ELM Ströme durch Simulationen mit großen, nichtlinearen Codes reproduziert werden können, ergibt sich hier eine Möglichkeit, die Größe der ELMs allgemein zu mindern: Durch Anlegen von Spannung an Divertorziegel oder Treiben helikaler Ströme würden die ELM Ströme gedämpft und das Wachstum der Instabilität begrenzt.

Abstract

Edge-Localized-Modes (ELMs) are a magnetohydrodynamic (MHD) plasma instability and pose a major challenge for future fusion power plants. While providing impurity transport and density control in fusion plasmas operating in the standard high-confinement mode (H-mode), ELMs decrease confinement and emit pulsed heat loads that can cause material erosion and partial melting in the divertor. Thus, understanding the cause and nature of ELMs is crucial to the success of any future fusion reactor. Although promising approaches in dealing with ELMs, foremost mitigation or suppression by magnetic perturbations and operating in naturally ELM free H-modes, such as the quiescent H-mode (QH-mode), are being explored, an in-depth understanding of ELMs is still highly desirable due to operational limits of controlled ELM regimes. The peeling-ballooning model can robustly predict the linear phase of type-I ELMs determining the onset of the instability. As a step beyond, this thesis explores physics of the nonlinear ELM phase on the DIII-D tokamak determining the size of the transient among others. Fast magnetics, soft x-ray (SXR) and infrared thermography (IR) are used to characterize ELM crashes, allowing the creation of a database to determine the parametric dependencies of ELM energy and particle losses on the plasma conditions and to connect these to the corresponding nonlinear signatures. While collisionality does not play a decisive role, the ratio of heating power to the H-mode power threshold is identified as parameter determining the agreement with the model, with discharges marginally above the threshold showing the largest scatter in the database and exceeding the predicted ELM energy up to twofold. Operation close to the H-mode power threshold is accompanied by low ELM frequency and large ELM heat loads. Using linear stability calculations, ELM energy densities are shown to be inversely proportional to the most unstable linear mode number before the ELM crash. Between mode onset and the subsequent increase in divertor heat flux, large currents flowing into the divertor floor have been measured by an array of shunt current resistors. Rapid oscillations in these currents are seen before the divertor deuterium radiation peaks. Typically, the current measured by a single tile during an ELM can reach 500 A. Assuming representativeness of divertor tiles with current sensor this would amount to a current of up to 20 kA flowing into a concentric circle near the strike point. Toroidal mode number analysis of the divertor currents appears consistent with a mix of low-n modes ($n<4$). The peak amplitude of the tile currents correlates weakly with the thermal energy loss during ELMs. An ELM current model (ECM) is developed based on a thermoelectric origin of the tile currents with flow through regions inside of the nominal separatrix and found consistent with the current measurements. A current flow through the confined plasma would lead to increased stochasticity at the plasma edge, explosive growth of the instability and thus contribute to particle and energy transport during the ELM. Further ELM current research has the potential for manipulating the ELM character by perturbations through non-axisymmetric divertor bias or tile insulation in the long run.

CONTENTS

1. Introduction

Fusion is powering the sun and stars of our universe. Ever since this scientific discovery the venture of mankind began aiming to replicate and harness the stellar energy source on earth. Driven by the ambitious desire to advance our human civilization to the first Kardashev level [1] – defined by the ability of using and storing all of the energy arriving from the parent star – and the long-term practical need for a clean, reliable and safe energy source, the promise of controlled nuclear fusion on earth has tantalized researchers. This chapter will outline the basics of fusion energy, introduce the tokamak as mainline reactor concept and one of its grand challenges, the heat loads produced by edge-localized-modes.

1.1. Nuclear fusion as promising energy source

While building a fusion power plant has proven to bear many more challenges than originally expected, the concept of nuclear fusion is readily explained: Due to the mass defect combining light nuclei to heavier nuclei sets free energy according to Einstein's famous $\Delta E=\Delta mc^2$ (if the reactants are lighter than iron, the most stable nucleus). Fusing a kilogram of hydrogen to helium can theoretically yield up to $6 \cdot 10^{14}$ Joule, covering the energy need of New York City for about two weeks and provide the equivalent of burning 14000 tons of oil. On earth, the most promising reaction in terms of energy yield and cross section for an achievable temperature range is based on fusing hydrogen's isotopes deuterium (D) and tritium (T) to helium (He)

$$^{2}_{1}\mathrm{D} + {}^{3}_{1}\mathrm{T} \rightarrow {}^{4}_{2}\mathrm{He} + \mathrm{n} + 17.6\ \mathrm{MeV}$$

Deuterium can be extracted from natural water, and tritium is bred in a lithium blanket in the reactor. Lithium itself is abundant in the sands of the earth, making fusion a quasi-inexhaustible energy source. Due to the Coulomb barrier between the hydrogen isotopes collision energies are too small at lower temperatures to get the distance between reactants in the range of the strong force. The temperature required for the fusion process to take place is on the order of tens of million Kelvin [2], where particles will form a plasma. Plasma is the fourth state of matter [3] and in the ideal, hot variant atoms are fully ionized. Nevertheless the electron and ion fluids still show collective behavior facilitating various innate plasma phenomena, among them a zoo of waves [4]. To achieve and maintain required plasma temperatures for ignition and sustain the fusion reaction, the heat must be confined long enough, so that the produced fusion

energy exceeds radiation and conduction losses. Under stationary plasma energy conditions, the confinement time τ is hereby defined as ratio of thermal energy stored in the plasma W and external heating power P_{heat}

$$\tau = \frac{W}{P_{heat}} \tag{1.1}$$

The quantitative requirements to sustain the fusion reaction were investigated by Lawson [5] and later resulted in the 'Lawson criterion', stating that based on the alpha particle production rate, the minimum product of temperature T, density n and τ ('triple-product') needs to exceed

$$nT\tau \geq 3 \cdot 10^{21} \frac{keV\ s}{m^3} \tag{1.2}$$

The product of density and temperature constitutes the plasma pressure p. While the ignition conditions are provided by gravitational compression in the core of stars, the main approaches on earth are compressing mixed deuterium/tritium pellets to achieve high densities for a short time using lasers (inertial confinement fusion) or using magnetic fields to confine the charged particles for a longer time at low densities (magnetic confinement fusion). In case of the latter, the magnetic field supports the plasma confinement as follows: Charged particles experience the Lorentz force on the plane perpendicular to the field leading to circling around field lines ('gyration'). To achieve confinement parallel to the magnetic field lines, two approaches have been pursued. Linear devices use special field configurations as for instance magnetic mirrors at the open field line endings. Performance problems - among others due to weak particle confinement - led to termination of most large-scale mirror programs [6]. The second approach consisting of toroidal assemblies with helically twisted magnetic fields has demonstrated good confinement. There are two main designs for toroidal assemblies: stellarator [7] and tokamak[1] [8]. Stellarators produce both magnetic fields (toroidal and poloidal) through complexly wound external coils, whereas tokamaks generate the poloidal field through a toroidal current. The contemporary focus is primarily on tokamaks as the ITER tokamak [9], the first fusion experiment designed to produce more power than it consumes is presently being built in Cadarache, France.

1.2. The tokamak path to fusion

The first torus shaped fusion machine, the Russian T-1, was built in 1957 [10]. The victory of the tokamak concept began in the 1960s when T-3 (a successor of T-1) produced very high electron temperatures leading to a Sputnik-like shock in the western fusion research hemisphere [11]. While there have since been noteworthy and considerable efforts in exploring alternative concepts, such as the recently launched

[1] Tokamak is a Russian acronym for toroidal chamber and magnetic coil.

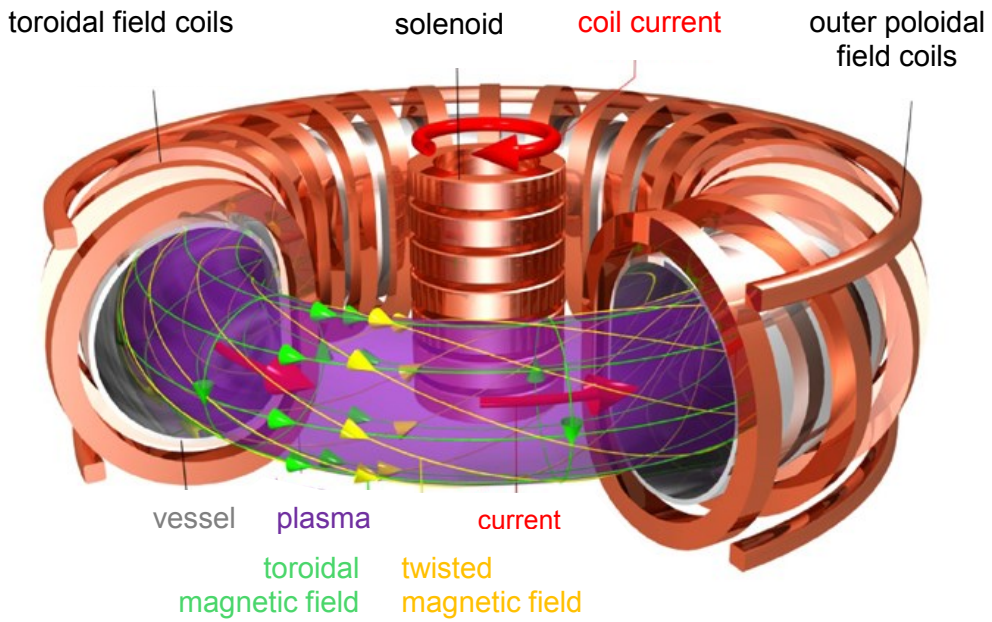

Figure 1 Basic construction of a tokamak, adapted reproduction from [174]

Wendelstein 7-X stellarator in Germany [12,13], the main effort was dedicated to tokamaks, due to the superior nTτ performance. The general construction is shown in figure 1. Tokamaks are axisymmetric with a central solenoid in the middle of the torus. The plasma (here in purple) can be thought of as a cylinder bent into a torus. While radial and poloidal component are the same, the height coordinate is being replaced by the toroidal angle. Large poloidal coils produce the toroidal magnetic field (green). A current through the solenoid induces current in the plasma acting as a secondary loop in this transformer (red) and the current flow in the plasma is generating the poloidal field, which is significantly weaker than the toroidal field. A helical field structure with nested flux surfaces is created (yellow), where the magnetic force balances the plasma pressure creating an equilibrium. Since the ohmic heating efficiency of the plasma current strongly drops with temperature, auxiliary heating becomes necessary, most notably in form of injection of a hot neutral particle beam (NBI) [14] and electron cyclotron heating (ECH) [15]. As current induction through the solenoid requires a current change limiting the plasma operation to one cycle, present day tokamaks are operated in pulsed mode. Every experiment consists of a repetition of discharges (shots): Depending on discharge design and the physics to be addressed, heating powers, shapes and currents among others are varied while measurements are taken with diagnostics. Achieving the goal of steady-state run requires super conducting coils, and additional heating and current drive provided by external systems.

As direct contact between confined plasma and wall has many disadvantages regarding impurity control and confinement ('limiter configuration'), additional poloidal field coils (top, bottom of figure 1) modify the poloidal magnetic field generated by the plasma current. Moreover, they provide stability against plasma expansion through the hoop force (similar to the rubber tire tube force this force results from a larger area on the outer side of the plasma torus compared to the inside at fixed pressure). Configuration dependent the poloidal field coils produce one or two points with zero poloidal field, termed the X-point(s), as shown in figure 2. The particles on nested flux surfaces inside of the X-point are confined as magnetic field lines are per definition bound to the closed flux surfaces, whereas field lines outside are intersecting on strike lines with the vessel (or strike points in plain geometry), in a component called the divertor. The divertor is the main plasma-material boundary and tasked with power handling and fueling economy.

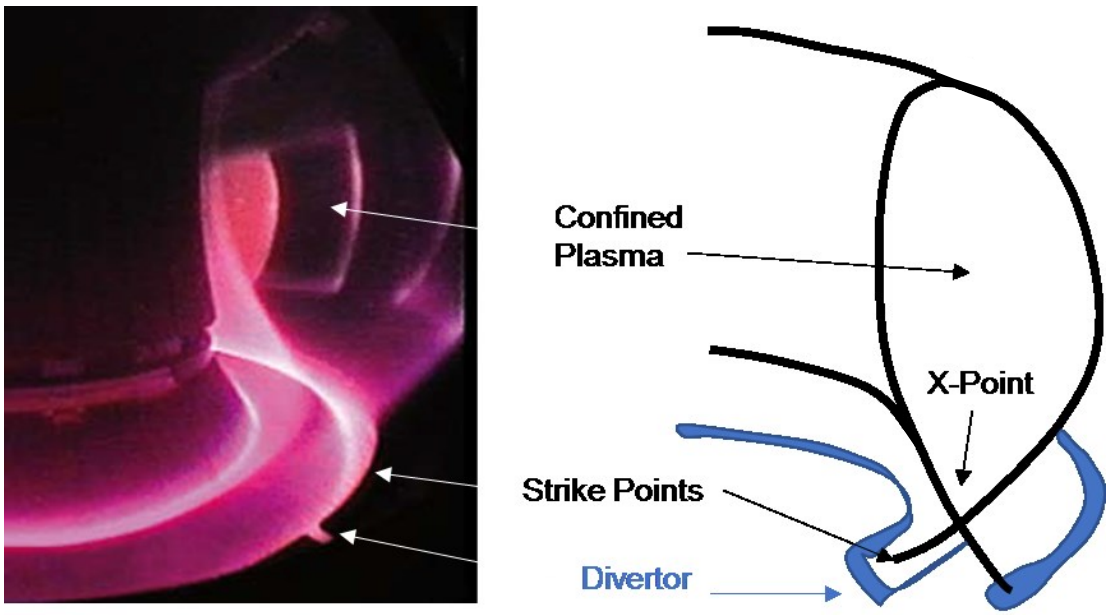

Figure 2 Diverted tokamak plasma cross section with visible light camera picture from the ASDEX-Upgrade tokamak (left), modified from [175] and schematic drawing (right). The confined plasma is so hot that it radiates only in the ultra-violet part of the spectrum and cannot be seen on camera, but the divertor strike lines are clearly recognizable.

The ratio of fusion power to externally injected heating power is termed gain Q and has constantly progressed. The highest gain of 0.62 achieved to date of this thesis occurred on the JET tokamak in a 26 MW heated discharge, that produced additional 16 MW of fusion power [16]. The work reported in this thesis was conducted at the DIII-D tokamak in San Diego, CA. DIII-D can be categorized as a mid-size tokamak (R = 1.67 m, a = 0.67 m) - presently the largest in the United States – with a maximum toroidal field of 2.2 T and plasma currents of up to 2.2 MA. A typical discharge lasts 5.0 s. Eight neutral beams produce up to 20 MW of injected power and additional power is provided

by electron cyclotron heating with up to 4 MW. The tokamak is known for its excellent plasma edge and divertor diagnostics.

1.3. Transient heat load challenge

There is agreement within the fusion community that the upcoming tokamak devices will operate in the so called H-mode, short for high confinement mode [17]. The better confinement compared to L-mode (low confinement mode) is achieved through a transport barrier provided by turbulence suppression through rotational shear at the plasma edge. This barrier comes at a price, as a stable H-mode is coupled to an inherent phenomenon in this region, labelled edge-localized-mode (ELM) [18,19]. ELMs are repetitive edge pressure gradient collapses expelling energy and particles reminiscent of solar flares on the sun. Without ELMs, density and radiated power of the plasma would monotonically increase - leading, finally, to a radiative collapse [20]. The ELMs are beneficial for the density control as well as for transport and exhaust of impurities like the helium ash out of the plasma core, but at the same time they can cause erosion on plasma facing components through heat and particle loads in the pulsed working mode. In forefront, the divertor of ITER and future reactors is a component of great concern as transient ELM heat loads are expected on this component far exceeding any known material handling capability on earth, which could lead to melting [21]. At a predicted natural ELM frequency of 1 Hz for ITER [21], significant damage and divertor life time reduction will be the consequence, also threatening economic viability of future fusion power plants.
There are different approaches to mitigate, avoid or suppress ELMs by using resonant magnetic perturbations through external coils (RMP) [22,23], artificially triggering ELMs by pellet injection [24] or using inherently ELM free regimes as QH-mode [25]. While these are proven concepts of ELM avoidance or suppression, they do have – even on current research reactors – operational limitations as for instance a torque threshold for the RMP [26] and are not guaranteed to work fully reliable on ITER. Hence, a more in-depth ELM understanding is crucial for successful ITER scenario design and operation.

1.4. Thesis outline

This thesis is dedicated to the nonlinear ELM phase, determining amount and scaling of loss energies and heat loads on the DIII-D tokamak. While there have been ELM studies before (e.g. [27,28]), the novelty of this work consists of a systematic study of the dependence of ELM divertor heat loads at both strike points on plasma parameters. Beyond the analysis of ELM size dependencies an ELM current model (ECM) is developed providing a deeper understanding of the role of the currents flowing during ELMs and illumination of how they drive nonlinear growth of the instability. The scientific achievement roots in the enhancement of conceptual ELM models to connect current measurements with theoretic predictions and computational results. As ELM

heat loads are considered a great challenge of future fusion power plants and ITER due to their damage potential for plasma facing components, this work aims to make a small contribution in addressing and exploring the relevant physics.

The remainder of the thesis is structured as follows:

- **Chapter 2** introduces the relevant physics of the H-mode and edge-localized-modes

- **Chapter 3** gives an overview of the hardware of the DIII-D tokamak and the diagnostics used in this work

- **Chapter 4** is dedicated to the analysis of ELM heat loads and their scaling with plasma parameters

- **Chapter 5** demonstrates the relevance of ELM currents and develops a model for understanding their role

- **Chapter 6** discusses the results, draws conclusions and gives an outlook into future work

The thesis uses SI units throughout except for particle temperatures which are being expressed in eV - suppressing the Boltzmann constant - as usual in plasma physics (1 eV = 11605 K). Some equations of the model developed in chapter 5 are based on research in the 1980s executed in the cgs system, which is kept for continuity and comparison.

2. Basics

Despite their name, edge-localized-modes are an instability affecting the whole tokamak. Born in the plasma edge, they can extend into the plasma core and expel energy out into the divertor. Hence, they have encouraged collaboration and integration of physics between different areas of fusion research. This chapter introduces the fundamental physics governing each region and typical plasma profiles to understand the basics of tokamaks and the nature of the ELMs.

2.1. Magnetohydrodynamic equilibrium

As stated previously, electrons and ions in a hot plasma show collective behavior. For magnetized plasmas as occur in space or tokamaks, the treatment of the system as single or two fluid has prevailed and became known as magnetohydrodynamics (MHD). MHD theory has led to the Nobel prize awarded discovery of Alfven waves [29]. While the MHD treatment of fusion plasma is valid along a broad temporal and spatial parameter range, covering the applications discussed in this thesis, limitations requiring more in-depth treatments will be pointed out: For instance, the MHD assumption of a thermal equilibrium obliges that the particles' mean free path is small compared to the system size (e.g. the plasma radius). Non-Maxwellian distributions require a kinetic treatment. If the particle gyroradius (also known as Larmor radius), i.e. the radius of the circular motion of charged particles in presence of a uniform magnetic field, is no longer small compared to the scale length of gradients (e.g. pressure gradient scale length at the plasma edge) a gyrofluid treatment is necessary as orbit effects come into play. In fusion research, finite Larmor radius effects concern - among others - the description of turbulence, while for instance transport along magnetic field lines requires kinetic treatment due to the long mean free path.
A basic MHD application in tokamak plasmas consists of the reconstruction the plasma equilibrium providing the magnetic field topology, i.e. the local magnetic field strength and flux surfaces. Together with density and temperature measurements the magnetic topology is necessary to analyze plasma stability. An in-depth MHD treatment is beyond the frame of this thesis, the interested reader is referred to extensive work [30–32], parts of this chapter are based upon. In simplified single fluid MHD (assuming quasi-neutrality with ion charge Z=1 so ion and electron densities are equal $n_I = n_e = n$, mass and momentum are dominated by ions), which suffices for many tokamak applications, the governing equations are

Continuity $$\frac{\partial \rho}{\partial t} + \nabla(\rho \vec{v}) = 0 \quad (2.1)$$

Momentum $$\rho \frac{\partial \vec{v}}{\partial t} + \rho(\vec{v} \cdot \nabla)\vec{v} + \nabla p = \vec{j} \times \vec{B} \quad (2.2)$$

with adiabatic closure $$\frac{d}{dt}\left(\frac{p}{\rho^{\gamma}}\right) = 0 \quad (2.3)$$

Maxwell $$\frac{\partial \vec{B}}{\partial t} = -\nabla \times \vec{E} \quad (2.4)$$

$$\nabla \vec{B} = 0 \quad (2.5)$$

$$\nabla \times \vec{B} = \mu_0 \vec{j} \quad (2.6)$$

Ohm's Law $$\vec{j} = \sigma(\vec{E} + \vec{v} \times \vec{B}) \quad (2.7)$$

with ion mass density $\rho = nm_i$, velocity v, pressure p, current density j, adiabatic coefficient γ (generally assumed to be 5/3) and conductivity σ.
As illustrated in the introduction (1.3), the poloidal field in tokamaks is produced by the plasma current. Since the field acts on the charge carriers with the Lorentz force,

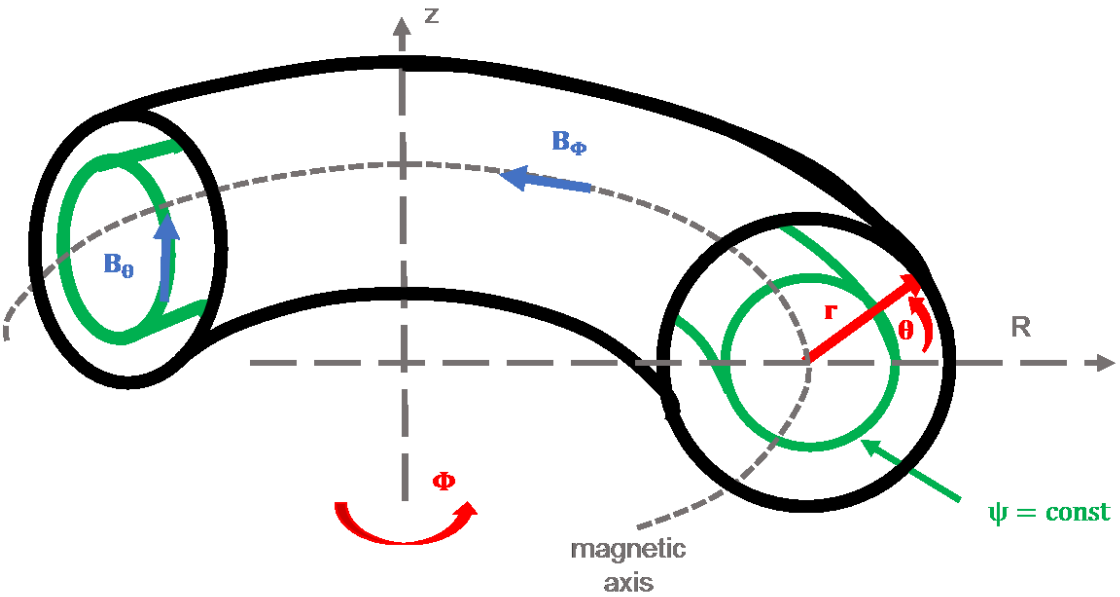

Figure 3 Schematic drawing of a nested flux surfaces in a tokamak equilibrium, with right hand coordinate system (red): radial component r (outwards from the magnetic axis in the center), toroidal component **ϕ** (360° around the torus) and poloidal coordinate **θ** (±180° from the midplane)

this will change the field producing current distribution, so that a self-consistent solution needs to be found.
In an equilibrium state, all time derivatives of the MHD equations disappear, hence equation 2.2 becomes (see figure 3 for illustration of the coordinates)

$$\nabla p = \vec{j} \times \vec{B} = j_\phi B_\theta \overrightarrow{e_\phi} \times j_\theta B_\phi \overrightarrow{e_\theta} = (j_\phi B_\theta - j_\theta B_\phi)\overrightarrow{e_r} \tag{2.8}$$

with $\overrightarrow{e_\phi}, \overrightarrow{e_\theta}$ and $\overrightarrow{e_r}$ denoting unity vectors in toroidal, poloidal and radial direction, respectively. From this equation it becomes apparent that the magnetic field vector is perpendicular to isobar surfaces (p=const). These are labelled flux surfaces as upon them not only the pressure but also the poloidal flux ψ is constant. The latter is calculated as

$$\psi = \int B_\theta \overrightarrow{e_\theta} \cdot \overrightarrow{dA} \tag{2.9}$$

with $\overrightarrow{dA}$ denoting the normal vector of an area differential. Figure 3 shows examples of nested flux surfaces (green and black). By defining f as a flux function for the poloidal current (in a similar way as pressure is a flux function) so that

$$j_\theta \overrightarrow{e_\theta} = \frac{1}{\mu_0} \nabla \times B = \frac{1}{R} \nabla f \times \overrightarrow{e_\phi} \tag{2.10}$$

one yields - after applying vector identities – the following equation

$$j_\phi = R \frac{\partial p}{\partial \psi} + \frac{\mu_0}{R} f \frac{\partial f}{\partial \psi} \tag{2.11}$$

With the operator $\Delta^* \psi \equiv R \nabla \cdot (\frac{1}{R} \nabla \psi)$, known as Grad-Shafranov operator, one yields

$$\Delta^* \psi = -\mu_0 R j_\phi \tag{2.12}$$

and finally

$$\Delta^* \psi = -\mu_0 R^2 \frac{\partial p}{\partial \psi} - f \frac{\partial f}{\partial \psi} \tag{2.13}$$

This equation is called ‘Grad-Shafranov equation’ [33,34]. For analysis of tokamak discharges it is typically solved by an interpretive code as EFIT [35] on DIII-D or CLISTE [36] on ASDEX-Upgrade (AUG). Both codes include currents in the shaping coils, affecting mainly the poloidal shape and magnetic field. Using measurements from magnetic probes and other diagnostics in the vessel the equilibrium is reconstructed in

an iterative process, matching diagnostic measurements with the calculated current and fields until the error is reasonably small (assuming perfect toroidal axisymmetry).
The obtained equilibrium is labelled 'standard'. As will be shown in the following segments, for the full or 'kinetic' solution, it is necessary to include corrections for the fast ion pressure and an additional edge current, labelled bootstrap current. This equilibrium is the base for all plasma stability analysis pursued in this thesis. As plasma contributions to the toroidal field are small, and the external toroidal field is generated by non-flexible coils its strength can be expressed assuming axisymmetry and using Ampere's Law as

$$B_T = \frac{B_{T0} \cdot R_{mag}}{R_{mag} + r\cos\theta} \tag{2.14}$$

Hence, B_T only depends on the radial distance from the magnetic axis creating a high- and a low field side. Hereby R_{mag} is the radius of the magnetic axis (from the center of the solenoid), r is the distance of a given point from the magnetic axis and θ is the angle between that line and the midplane (plane with z=0, see figure 3). The field value at the magnetic axis B_{T0} (r=0) is the value used to compare different discharges and for notation simplicity conventionally referred to as B_T.
An important parameter as measure of the confinement quality is the plasma beta, the ratio of the mean plasma pressure $\langle p \rangle$ to central magnetic field pressure

$$\beta = \frac{\langle p \rangle}{\frac{B^2}{2\mu_0}} \tag{2.15}$$

In tokamaks β is limited to single digit percentage range due to stability restrictions [32]. For comparison between machines, a slightly different parameter is used, termed β_N (N for normalized), defined as

$$\beta_N = \beta \cdot \frac{aB_T}{I_P} \tag{2.16}$$

with a the minor plasma radius and plasma current I_P in MA. β_N is expressed in percentage and covers a range from 0-4[2]. This normalization was introduced since $\frac{I_P[MA]}{a[m]\cdot B_T[T]} = 2.8\,\%$ has empirically been shown to be an ideal MHD stability limit for most tokamaks (above which deleterious modes destabilize or destroy the plasma) and became known as the Troyon limit [37]. In a similar fashion, the so called Greenwald density limit n_G [38] describes an empirically observed operation limit for the line-averaged density in tokamaks

$$n_G = 10^{14}\mathrm{m}^{-3} \cdot \frac{I_p}{\pi a^2} \tag{2.17}$$

[2] The percentage sign is not noted.

Another useful parameter for stability considerations is the safety factor q, defined as the number of toroidal turns n a confined particle completes for a given number of poloidal turns m ($q = \frac{m}{n}$) and assuming cylindric cross section can be calculated as

$$q = \frac{r}{R} \cdot \frac{B_T}{B_p} \tag{2.18}$$

All field and length quantities in equation 2.18 refer to their specific value at the desired location. Of particular interest are rational surfaces (q=1,3/2,2….), i.e. surfaces encompassing field lines closing on themselves, as modes tend to be localized on or near these surfaces. Due to the vanishing poloidal field at the X-point, q diverges at the boundary of open and closed flux surfaces, so that the value near the pedestal top $q_{95} = q(\psi_N = 0.95)$ is conventionally used for comparisons.
Closely related to the safety factor, the magnetic shear s informs about the gradient of the field ratios.

$$s = \frac{r}{q} \cdot \frac{dq}{dr} \tag{2.19}$$

A final normalized quantity is the ion Larmor radius, measuring how closely ions gyrate around field lines relative to the system size of the tokamak. It is defined as

$$\rho^* = \frac{\rho_i}{a} = \frac{\sqrt{3 m_i T_i}}{ZeB_T a} \tag{2.20}$$

with Z and m_i the ion charge and mass and T_i the ion temperature, which is typically referring to the respective values at half radius in inter tokamak comparisons.

2.2. Plasma shape and quantities

It will be shown in the following sections that the shape of the plasma has large influence on its stability. Hence, certain geometric quantities and ratios received their own label [39]. A reconstructed DIII-D equilibrium (‘kinetic EFIT’) is depicted in figure 4. The green lines resemble equidistant flux surfaces based on ψ_N the normalized poloidal flux of a given location x:

$$\psi_N = \frac{\psi_x - \psi_{mag}}{\psi_{sep} - \psi_{mag}} \tag{2.21}$$

with ψ_{sep},ψ_{mag} and ψ_x the poloidal fluxes at the separatrix (bold solid line), the magnetic axis (center of the flux surfaces) and the desired location x, respectively. The separatrix[3] is the flux surface with the X-point(s) and forms the boundary between

[3] In case of plasmas limited by material objects (limiter/wall instead of divertor) there is no separatrix, the boundary is then just called last closed flux surface.

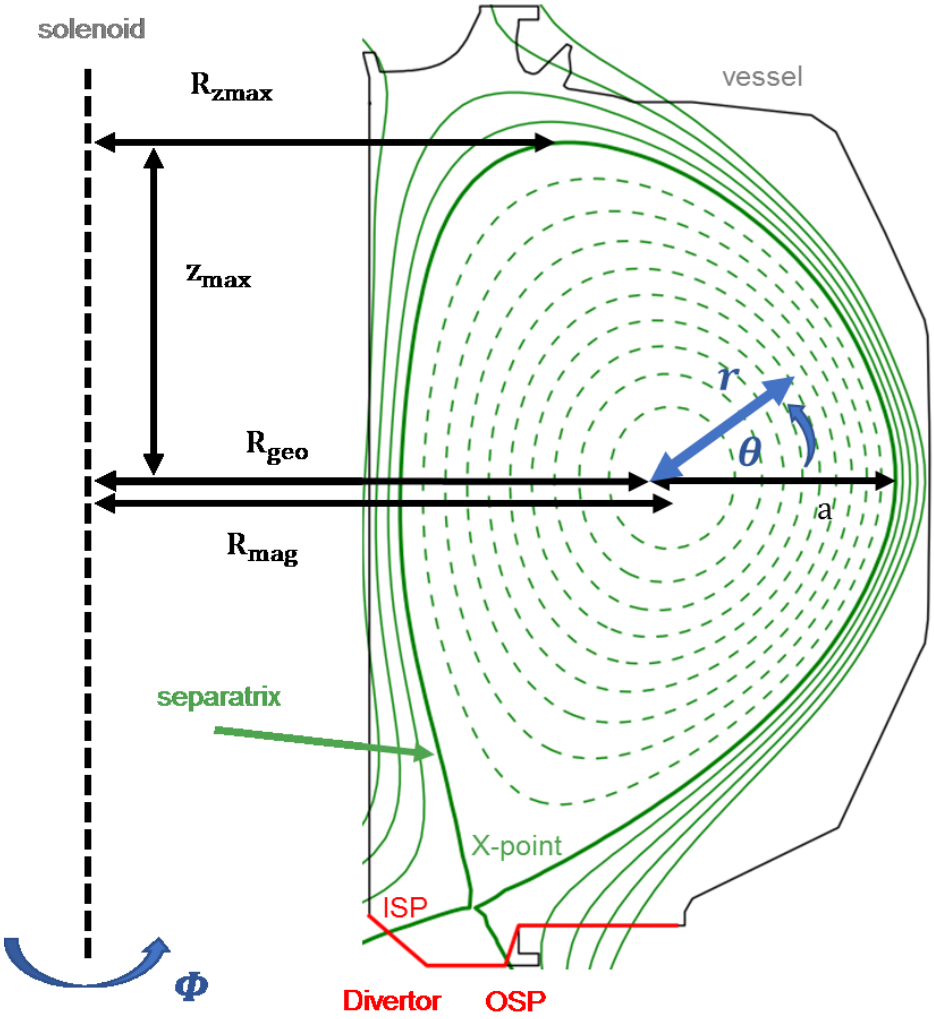

Figure 4 Example for a DIII-D plasma shape with flux surfaces, geometric quantities and divertor

confined and open flux surfaces. ψ_N has a value of 0 at the magnetic axis and from there extends to 1 at the separatrix. The region outside of the separatrix is labelled Scrape-Off-Layer (SOL). While the confined flux surfaces are symbolized by dashed green lines in $\Delta\psi_N$=0.1 steps, the open SOL field is represented with solid lines of the same step size. As plasmas do not generally have the same volume, ψ_N greatly helps to compare physics processes confined to certain zones. In plane geometry the intersections of the separatrix with the divertor form inner and outer strike point (ISP/OSP), the region in between is named private flux region. The black surrounding line represents the vessel, the intersection with the plasma is on the inner wall and divertor (red line). Figure 4 also shows the standard coordinate set (ϕ, r, θ) used in tokamaks in blue. All radii are measured from the toroidal axis in the center of the solenoid. The radii of the furthest and nearest confined field line labelled as R_{max} and R_{min} determine the radius of the geometric center of the plasma R_{geo} and the plasma minor radius a as

$$a = \frac{R_{max} - R_{min}}{2} \tag{2.22}$$

$$R_{geo} = \frac{R_{max} + R_{min}}{2} \tag{2.23}$$

Due to various shifts and shaping, R_{geo} generally differs from the magnetic axis radius R_{mag}. z_{min} and R_{zmin} are the coordinates of the lowest point in the confined plasma, (z_{max} and R_{zmax} are set by the highest confined point) which is the lower x-point in this example. This shape is called a lower single null (LSN), a double null (DN) comes with two x-points and an upper single null (USN) plasma only with an X-point near the top of the vessel and strike points on the upper divertor. The elongation κ - known from the elliptic definition - is the ratio of larger to smaller radius

$$\kappa = \frac{z_{max} - z_{min}}{2a} \tag{2.24}$$

The aspect ratio ϵ is defined as

$$\epsilon = \frac{R_{geo}}{a} \tag{2.25}$$

Seeking higher order shape similarities, the upper (u) and lower (l) triangularity are calculated as

$$\delta_{u/l} = \frac{R_{geo} - R_{zmax/zmin}}{a} \tag{2.26}$$

The mean of upper and lower value is usually referred to as triangularity δ. The squareness is defined as ratio of the length of the diagonal over the confined plasma to its full length in an inscribed box over each quadrant [40].
Note that the equilibrium in figure 4 is reconstructed under the assumption of perfect axisymmetry. However, small intrinsic error fields in tokamaks can have effects on stability and lead to the need of three dimensional equilibria provided by codes as VMEC [41].
Following the geometric and magnetic topology overview a brief introduction into plasma profiles and tokamaks operation scenarios is given in the next chapter.

2.3. Standard H-mode

Discovered on the ASDEX tokamak in Germany in 1982 the high confinement mode (H-mode) is considered the standard fusion reactor operating regime for ITER and

future reactors [17,42]. Its stored energy[4] calculated as volume integral over confined particle temperatures and densities

$$W_{MHD} = \sum_X \int \frac{3}{2} n_X T_X \, dV \tag{2.27}$$

- with X denoting electrons and ion species- is generally around twice as large as in the low confinement mode (L-mode) as shown in the profiles in figure 5. The abscissa is

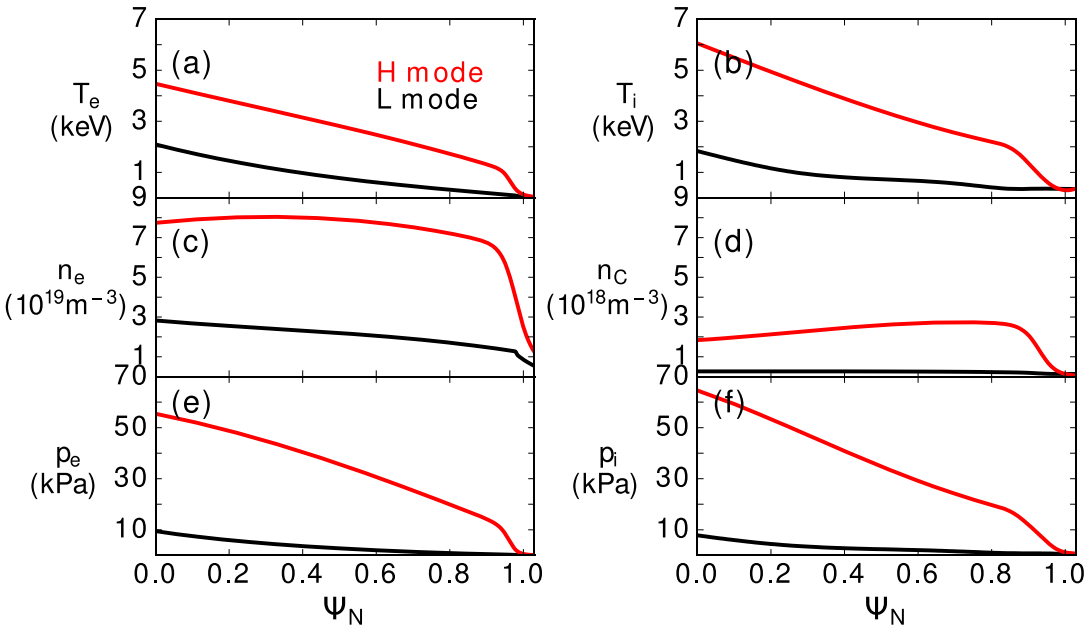

Figure 5 Profiles of electron temperature (a), density (c) pressure (e) during L-mode (black) and H-mode (red) and corresponding ion profiles (b, d, f). The total pressure is the sum of the partial pressures of electrons and all ion species (Deuterium and Carbon on DIII-D)

the normalized poloidal flux ψ_N. Electron profiles of temperature (a), density (c) and their resulting pressure $n_e T_e$ (e) are shown in the left column and corresponding ion profiles on the right column. As will be explained in section 3.2.2 the main ion density is not measured directly but inferred from impurity density measurement (d) under assumption of quasi-neutrality. Being wall and divertor material, Carbon is the dominant impurity on DIII-D. Similarly, Deuterium and Carbon ion temperature are assumed to be equal (b) to calculate the ion pressure (f). In this example, the plasma core extends from the center out to ψ_N=0.95, the remainder is the plasma edge. One can see that the gradients of the electron and ion temperature profiles for the plasma core in (a, b) appear similar, whereas the gradients in the edge region are much stronger during H-mode. Note that both temperature and density drop by several orders of

[4] The stored energy is generally labelled as W (as in equation 1.1), however the preferred DIII-D notation is W_{MHD} and will be kept throughout this thesis.

magnitude in the H-mode edge region. In the portrayed example the electron temperature falls from approximately 1.5 keV at the top to 100 eV at the separatrix. The improved confinement during H-mode is achieved by an edge transport barrier (ETB) which reduces heat and particle transport perpendicular to the magnetic flux surfaces and thereby forms larger gradients in radial direction [43,44]. While the formation of the ETB is not fully understood yet, a prominent theory is based on the decrease of turbulence eddy size and correlation length due to velocity shear [45]: During H-mode a radial electric field well is formed in the plasma edge, causing a strong drift velocity (so called ExB drift) and sheared rotation profiles in poloidal direction suppressing turbulence. Another suggested mechanism includes zonal flows at the edge that decrease the energy of smaller eddies and stretches them leading to their disappearance [46,47].

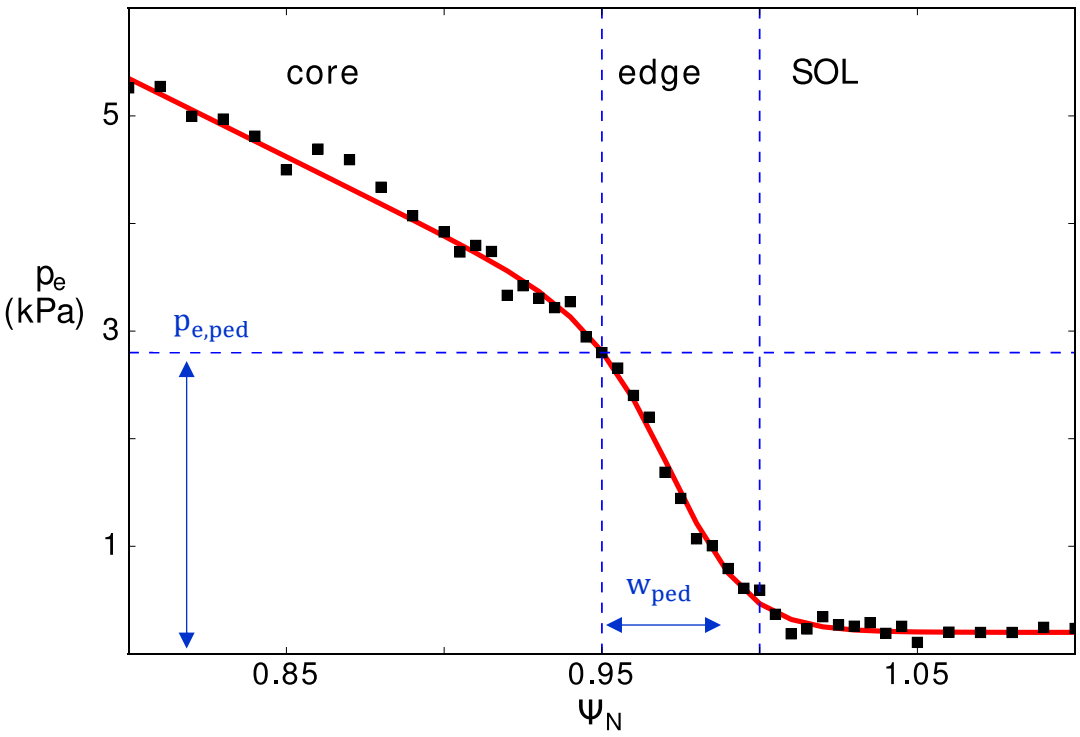

Figure 6 Electron pressure profile around the plasma edge region with tanh-fit (red), electron pedestal pressure and width in blue. The gradient in the edge is much steeper than in core or Scrape-Off-Layer.

Operationally, the access to H-mode requires higher auxiliary heating power, so that most discharges are started up in L-mode and then quickly forced into H-mode by a sharp increase in injected power. The plasma edge (or pedestal) is a region with a size on the order of centimeters in real space (figure 6). On the outer side the pedestal is limited by the separatrix and the whole plasma is surrounded by the SOL. Even though the volumetric fraction of the pedestal region is small, it governs important confinement properties of the plasma: Achievable density and temperature gradients are limited

inside of the steep edge region (plasma core), a phenomenon that became known as profile resilience [48]. Consequently, many characteristics of the plasma depend on properties of the pedestal. Two very important quantities are the pedestal width w_{ped} and pressure at the top[5] p_{ped}, since they determine the edge gradients. For instance, transport codes predict the fusion power of a tokamak to approximately scale with the square of the pedestal pressure [49]. On DIII-D, in most cases both quantities can be calculated from parameters of a special hyperbolic tangent based fit [50] as shown for an electron pressure profile in figure 6. The respective diagnostics for measuring density and temperatures are introduced in chapter 3.
During H-mode the sharp density and temperature gradients at the edge drive a current in co-Ip direction on the low field side (LFS), termed the bootstrap current [51,52]. While in standard scenarios the current density is largest by far in the plasma center, steady-state scenarios aim to create an off-axis peak by maximizing the bootstrap current to reduce the need for ohmic drive and enhance discharge duration to infinity with auxiliary current drive. The bootstrap current can be calculated using neoclassical (comprising all physics effects due to the torus geometry) codes as NEO [53], or estimated based on approximations as the Sauter model [51]. An important parameter in this regard is the electron collisionality ν_e^*, a measure for how often electrons at the plasma edge collide. In general, it is compared at the pedestal top and calculated via [51]

$$\nu_e^* = 6.921 \cdot 10^{-18} \cdot q_{95} \cdot R_{max} \cdot n_{e,ped} \frac{\left(1 + 30 \cdot \frac{n_{C,ped}}{n_{e,ped}}\right) \cdot (31.3 - \ln \frac{{n_{e,ped}}^{0.5}}{T_{e,ped}})}{{T_{e,ped}}^2 \cdot \left(\frac{a}{R_{Surf}}\right)^{1.5}} \tag{2.28}$$

where R_{Surf} is the major radius of the center of the outermost closed flux surface, and all quantities with subscript ped refer to the respective value at the pedestal top. For low collisionality plasma conditions, the Sauter formula is resulting in a local, poloidal flux dependent bootstrap current scaling with [51]

$$j_{bs} \sim I_P \cdot p \cdot \left(\frac{0.5}{n_e}\frac{\partial n_e}{\partial \psi} + \frac{0.15}{T_e}\frac{\partial T_e}{\partial \psi} + \frac{0.1}{T_i}\frac{\partial T_i}{\partial \psi}\right) \tag{2.29}$$

indicating that density gradients are more efficient in driving bootstrap currents in this evironment. Note that the bootstrap current will achieve its largest values in the steep gradient region of the plasma edge and modify the magnetic equilibrium.
Higher collisionality causes a decrease of the coefficients in equation 2.29 in a $1/(1+\sqrt{\nu_e^*})$ leading order relation and leads to a mitigation of the bootstrap current [54]. Additionally, the heating via NBI contributes to the current drive and builds up a fast-ion density population. Using a transport code as ONETWO [55] or TRANSP [56,57], the important fast ion properties can be calculated. The standard equilibrium together

[5] Also termed pedestal height

with the modified profiles and the edge current constraint are used to reconstruct the actual equilibrium, that is now labelled kinetic equilibrium (kinetic EFIT) and used as foundation for all stability analysis in this thesis.
This overview summarizes some of the basics of H-mode physics, which has been a focus of research for decades [58]. Only recently, the L to H transition was simulated with an exa-scale nonlinear code for the first time [59], indicating the complexity of the involved physics. For calculating the necessary power to access H-mode (L-H threshold power), an approximation based on a multi-machine-scaling is used throughout this thesis [60]

$$P_{LH} = 0.049\ \bar{n}^{0.72} B_T{}^{0.8} S^{0.94} \tag{2.30}$$

Here S stands for the plasma surface in m^2, $\bar{n}$ for the line-averaged electron density in $10^{20} m^{-3}$ and B_T is the central magnetic field strength in T. Note that the threshold power depends on the direction of the magnetic field [61] and that this formula is valid for the case where a drift of particles related to the curvature of the magnetic field points towards the dominant x-point (favorable $B \times \nabla B$ drift). An overview of DIII-D field configurations is given in appendix A.

2.4. Phenomenology of edge-localized-modes

Endemic to standard H-modes are edge-localized-modes. ELMs transfer particles and energy from the pedestal and core region to the SOL, wall and divertor by causing the H-mode transport barrier to briefly collapse. On DIII-D, an ELM usually takes less than two milliseconds and causes an energy loss of up to 15 % of the stored plasma energy, thereby decreasing confinement. ELMs are subdivided in three different categories [18]:

- type I: also known as giant ELMs, they are large in size (1-15% of stored energy) at low frequencies between 1-60 Hz on DIII-D. As their frequency increases with heating power, the characteristic behavior of type I ELMs is the reciprocal relationship of ELM frequency f_{ELM} and size W_{ELM} [18,62]

$$f_{ELM} \cdot W_{ELM} = c \cdot P_{SOL} \tag{2.31}$$

  with c=0.2-0.4 the proportionality constant and P_{SOL} the power in the SOL, usually approximated as difference between heating and radiation power. A pathological case of the type I ELM is the compound ELM, where the ELM energy loss in a weakly heated scenario suffices to enforce a transient return to L-mode.

- type II: occurring in highly shaped scenarios (large elongation and triangularity). The frequency is higher and the amplitude lower than for type I ELMs.
- type III: these ELMs decrease in repetition frequency with increasing auxiliary power, so they typically occur at the transition into H-mode, their size is smaller than type I

The critical ELMs for ITER and future power plants are the type I ELMs due to their large energy and their ubiquity in H-mode scenarios. This work is focused on natural type I- ELMs (i.e. no control or mitigation mechanisms as three-dimensional fields or pellet injection are applied) and unless explicitly stated otherwise, ELM and type I-ELM will be used synonymous throughout this work.

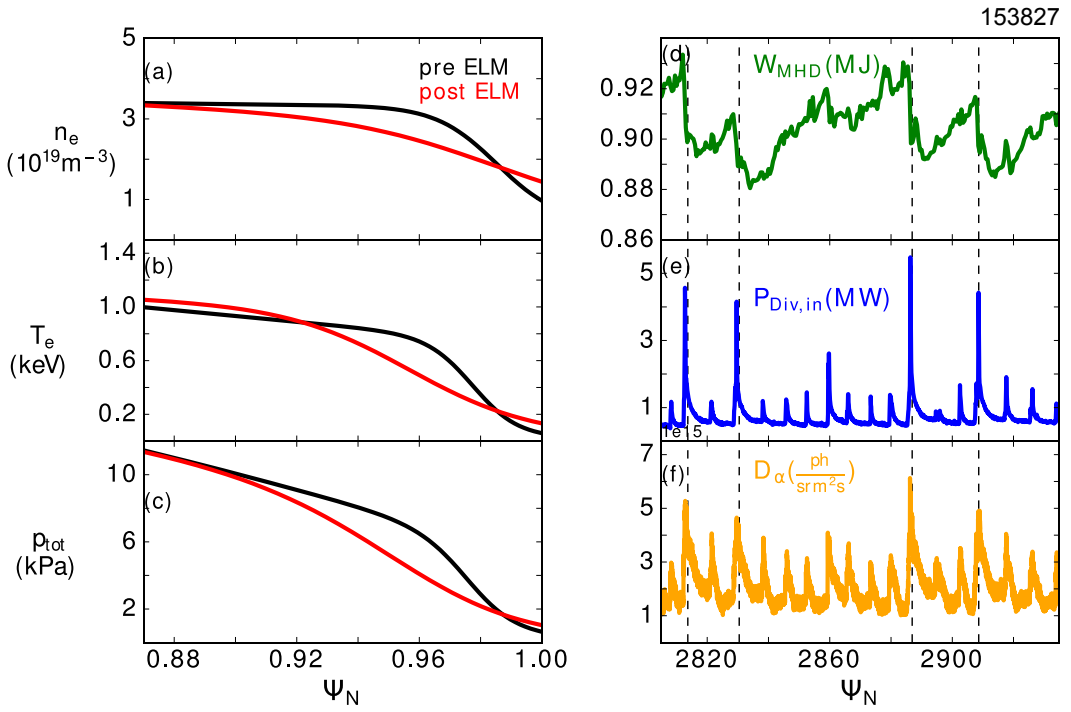

Figure 7 Impact of ELMs on DIII-D: Comparison of profiles of electron density (a), temperature (b) and total plasma pressure (c) before and after ELMs on discharge 153827. Discharge evolution with stored energy (d), power to the inner divertor (e) and D-α signal (f). Type I ELMs are marked by dashed lines.

Figure 7 shows the effects of ELMs in a standard H-mode plasma on DIII-D by comparing profiles of electron density (a) and temperature (b) as well as the total pressure (c) before and after ELMs. These are obtained by averaging respective measurements over multiple time windows between ELMs. For pre-ELM conditions measurements in the 80-99 % interval of the inter ELM time window (time between successive dashed lines in figure 7) are used, whereas post ELM conditions are obtained from the 0-20 % phase. While not shown here, both ion temperature and density profiles are affected in a similar manner [63]. The expulsion of particles and heat is

recognizable by the losses at the pedestal top and the transient increases of density and temperature at the separatrix. In this example, each of the ELMs causes an energy loss of about 30 kJ (d) and is detected with power spikes of up to 5 MW in the inner divertor (e). Note that the practical and qualitative ELM detection method on DIII-D is the measurement of deuterium radiation in the divertor (f). It originates from neutral atoms in the SOL excited by interaction with ELM expelled particles and energy. The transitions of those excited atoms from the n=3 to n=2 quantum level of deuterium (the Balmer-α-line, hence the filterscope is often referred to as D-α) are detected [64].
Regarding the linear phase, comparison to experimental data has led to wide acceptance of the peeling ballooning model in the community for explaining the ELM onset.

2.4.1. Peeling-ballooning model

This model describes ELMs as MHD instabilities that occur as soon as the relevant profiles (pressure, current) at the plasma edge hit a stability limit, labelled peeling-ballooning limit [65]. The ballooning instability causes a confinement degradation by perturbation of the magnetic field and leads to a formation of 'fingers' of the expelled plasma, i.e. localized radial structures. A special case is the interchange instability, the plasma equivalent of the Rayleigh-Taylor instability in a gravitational field. This instability occurs when the magnetized plasma system can gain energy by strengthening the magnetic field and simultaneous plasma expansion through outward particle transport (i.e. relaxation of the pressure profile). In the tokamak this is possible on the low field side, i.e. at high outer radii, because plasma particles and magnetic field need to move in opposite directions to minimize the system's energy. The normalized pressure gradient α is a good index in ballooning stability analysis. It is derived from the energy necessary for bending the magnetic field lines and the energy win from moving the plasma [66].

$$\alpha = \frac{\mu_0}{2\pi^2}\frac{\partial V}{\partial \psi}\left(\frac{V}{2\pi^2 R}\right)^{\frac{1}{2}}\frac{\partial p}{\partial \psi} \tag{2.32}$$

where μ_0 is the vacuum permeability, V is the volume enclosed by a flux surface with the poloidal flux ψ, R is the plasma major radius and p the pressure. The second component of the stability limit, the peeling mode is related to finite current at the plasma edge. An edge current perturbation changes the magnetic field topology leading to particle loss in a self-amplifying cycle. The linear Eigenfunctions of pure peeling modes have only a small radial extent (compared to ballooning modes with the same mode number) [49] and are most unstable if a rational surface is located just outside of the plasma, as stabilizing influences of magnetic perturbations in the vacuum are minimized. Stability criteria have been defined multiple times [67,68], based on the peeling mode stability criterion for a simplified cylindrical torus [65]

$$\sqrt{1 - D_M} > 1 + \frac{1}{\pi q'}\oint \frac{j_\parallel B}{R^2 B_p^3}\,dl \tag{2.33}$$

where $q' = \frac{dq}{d\psi}$, B_p the poloidal field strength and DM is the Mercier coefficient, a complex expression depending among others on the magnetic shear (equation 2.19) [69]. The integration is executed along a magnetic field line. Assuming the left side is relatively constant, equation 2.33 conveys that a large and peaked parallel edge density $j_{\parallel}$ will lead to a violation of the stability criterion and triggering of peeling modes. The peeling-ballooning model is based on the interplay of these two instabilities. A strong current density at the edge arising due to temperature and density gradients will drive peeling modes but at the same time reduce magnetic shear and thereby stabilize certain ballooning modes [70,71]. Hence, the pure edge ballooning mode limit under these operational conditions (so called second stability ballooning limit [72]) can be experimentally exceeded [73]. On the other hand, strong pedestal pressure drives ballooning modes but stabilizes peeling modes. This complex interdependent system is governing linear stability at the edge and requires computational efforts for proper evaluation and calculation of individual mode growth rates. Note that lower n peeling-ballooning modes penetrate deeper into the plasma than higher n modes. The established procedure in linear stability analysis is to first self-consistently vary the pedestal pressure profile (with matching equilibria) and edge current density of the respective equilibrium and calculate the stability for each of these profiles. In the final step, a stability map is produced marking the operational point in the surrounding pressure/current environment and indicating the relative stability. On DIII-D, ELITE [49] is the main code to determine linear edge stability. A schematic diagram of the analysis is in shown in figure 8. The x-axis represents α, the normalized pressure

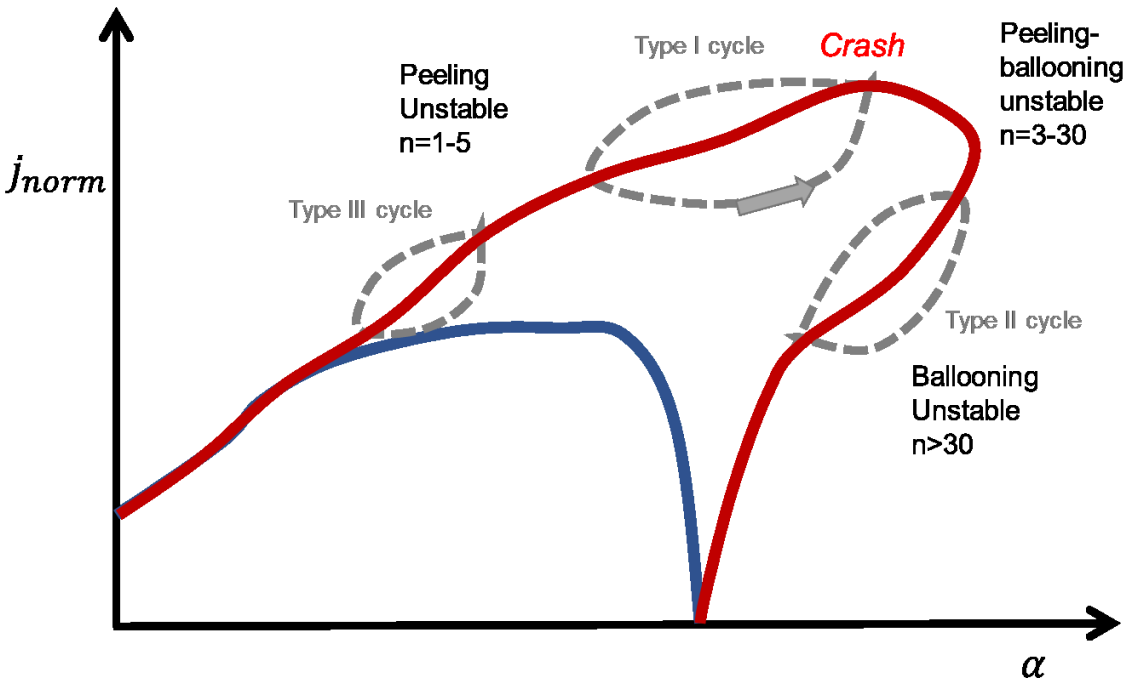

Figure 8 Peeling-ballooning diagram with location of various ELM cycles in j-α space. Stability limits for weakly (blue) and strongly (red) shaped plasma. Typical mode numbers of respective linear modes.

gradient, as defined in equation 2.32. The plotted value is the maximum of α in the plasma edge. The y-axis denotes the relative edge current density j_{norm}, defined by the ratio of the sum of the maximum current density in the edge region $j_{edge,max}$ and the separatrix current density j_{sep} to the normalized current density across the plasma j_{av}

$$j_{norm} = \frac{j_{edge,max} + j_{sep}}{2j_{av}} \tag{2.34}$$

The operational space is limited by the peeling stability in j_{norm} direction and by the ballooning limit in α direction. Increased shaping causes the coupling between these modes to improve and the nose of the diagram to be stronger (red vs blue curve) [65]. The difference between the empirically identified ELM types and their dependence on heating power that were introduced conceptually in the beginning of this chapter can be understood with this model [49]: Type-I ELMs are localized at the intersection of peeling and ballooning branches (in the nose of the diagram), type-III ELMs on the peeling and type II ELMs on the ballooning branch. As the pressure gradient grows on transport and the current on slower resistive timescales plasma heating will build up pressure gradients faster than current densities. Hence an increase in heating power will lead to a decrease in type III ELM frequency (pressure build up takes the operating point further away from the peeling stability boundary), whereas it causes type-I ELMs to exceed the ballooning limit faster, increasing their frequency. Higher collisionality (or density) is associated with higher n peeling-ballooning modes, as the bootstrap current scales inversely with collisionality over a wide range, improving peeling stability.

Due to the purely toroidal field at the X-point (leading to a diverging safety parameter among others), ELITE only integrates in the well-behaved parameter space to 99.5 % of normalized toroidal flux. For a nonlinear treatment including the X-point and resistive effects, nonlinear codes as JOREK [74] or M3D [75] are necessary. While nonlinear codes can show many interesting features of the ELM, as the conversion of higher n linear modes to low n modes in the nonlinear phase [76,77], they still face many challenges. Most important, linear simulations can be finished on the lab computer cluster in about a day, nonlinear simulations need run time on dedicated national servers for several weeks. To reproduce experimental ELM measurements, they may need to be initiated with a linearly unstable equilibrium and certain simulation parameters may need to be defined outside of experimental conditions (for instance resistivities or perpendicular heat diffusivities). As quantitative comparisons by JOREK, the most advanced nonlinear ELM code do not reproduce the experimental temporal heat flux profile of ELMs (in particular the large initial spike), an additional mechanism for the explosive growth in the nonlinear ELM phase is still sought for [78,79].To improve codes, experimental data of the nonlinear ELM phase is necessary for comparison. Most of the ELM data is collected in the SOL and the divertor, the basics of which will be explained in the following chapter.

2.4.2. ELM Scrape Off Layer physics

For the understanding of ELM heat load impact in SOL and divertor it is useful to consider the respective fundamental physics of the inter-ELM phase first. An upper limit to the power in the SOL can be deduced from a balance of heating power P_{heat}, change of plasma energy $\frac{dW_{MHD}}{dt}$ and radiative losses P_{rad}

$$P_{SOL,max} = P_{heat} - P_{rad} - \frac{dW_{MHD}}{dt} \tag{2.35}$$

While this approximation is used in ELM frequency calculations, effects as heating efficiency reduction due to neutral beam shine through or non-axisymmetric radiation require transport analysis. Due to higher conductivity parallel to the magnetic field than perpendicular to the field, the SOL power is spread out in a circle with a very thin radial layer λ_q [80] when exhausted from the plasma leading to an average poloidal heat flux of

$$q_{\perp,OMP} = \frac{P_{SOL}}{2\pi R_{out}\lambda_q} \tag{2.36}$$

at the outer midplane (OMP) with R_{out} the radius at the OMP.
A simple but very practical approach is based on linking the conditions at the OMP to the divertor and became known as the two-point-model [81]. An important result hereof is the strong dependence of P_{SOL} on the electron separatrix temperature $T_{e,sep}$

$$P_{SOL} \sim T_{e,sep}^{7/2} \tag{2.37}$$

as this illustrates why the separatrix temperature is a very rigid parameter in each fusion experiment and often treated as a boundary condition for kinetic EFITs (e.g. $T_{e,sep}$=70-100 eV on DIII-D).
Towards the divertor, the magnetic field weakens compared to the field at OMP due to fields produced by the poloidal coils, leading to an increase of area by the magnetic flux expansion f_x (conservation of enclosed flux by the SOL field lines).

$$f_x = \frac{B_{T,div}}{B_{T,OMP}} \cdot \frac{B_{p,div}}{B_{p,OMP}} \tag{2.38}$$

The flux expansion can be further increased by designing the divertor to have poloidal inclination with regards to the magnetic field lines. Without inclination, the area on the divertor receiving the energy ('wetted area') can be calculated as $A_{wet} = 2\pi R \cdot \lambda_q \cdot f_x$, yielding an average target heat flux of

$$q_{target} = q_{\perp,OMP} \cdot \frac{1}{f_x} \cdot \frac{R_{OMP}}{R_{div}} \tag{2.39}$$

with R_{div} the radius of the strike point. This is valid for the steady state phase.
For the characterization of the heat load caused by transients as ELMs the peak parallel ELM energy density $\varepsilon_{\parallel,peak}$ has prevailed (aside from divertor peak heat flux, heat flux width, and deposited energy). $\varepsilon_{\parallel,peak}$ is computed from the target ELM energy density ε_{tar}, defined as the spatial maximum of the time-integrated heat flux $q_{target}(s,t)$

$$\varepsilon_{tar} = \max(\varepsilon_{tar}(s)) = \max\left(\int_{\tau_{ELM}} q_{target}(s,t)dt\right) \tag{2.40}$$

where s is the radial coordinate along the tile surface, t is the time and τ_{ELM} is the ELM duration. This quantity is generally obtained of infrared thermography measurements. In order to allow comparisons between different machines or divertor configurations, the target ELM energy density is projected onto magnetic field lines, to obtain the corresponding parallel ELM energy density $\varepsilon_{\parallel}(s)$. The peak parallel energy density is the spatial maximum of $\varepsilon_{\parallel}$:

$$\varepsilon_{\parallel,peak} = \max\left(\frac{\varepsilon_{tar}(s)}{\sin\gamma(s)}\right) = \max\left(\frac{\int_{\tau_{ELM}} q_{target}(s,t)dt}{\sin\gamma(s)}\right) \tag{2.41}$$

where γ represents the incidence angle of the magnetic field lines with respect to the divertor tile surface. To simplify notation, $\varepsilon_{\parallel}$ will be used in the following for the peak parallel ELM energy density. The standard unit for $\varepsilon_{\parallel}$ is MJ/m^2. Typically, the location of the maximum is close to the strike point for narrow heat flux profiles, but it can be significantly different depending on the magnetic field configuration, in particular for broader heat flux profiles. As indicated in [82], $\varepsilon_{\parallel}$ represents an appropriate quantity for ELM heat load extrapolation when considering the dynamic of melting and erosion. The conventional approach to ELM heat load extrapolation, as shown by Loarte [21] is based on the empirical scalings for plasma energy losses during an ELM, W_{ELM}, the wetted area and experimental evidence that plasma energy losses during type-I ELMs are inversely related to the electron pedestal collisionality ν_e^* (equation 2.28) [83].
For ITER, the predicted ν_e^*~0.06-0.1 [84] entails ELM sizes of up to 20 % of the pedestal energy. In the initial, non-active phase (only helium or deuterium fuel, half value of possible current and magnetic field), a pedestal top temperature of 2.35 keV is predicted at a density of $4 \cdot 10^{19}\,\frac{1}{m^3}$ (active phase: 4.7 keV, $8 \cdot 10^{19}\,\frac{1}{m^3}$). At a plasma volume of 830 m^3, approximating the pedestal energy with $T_{e,ped} = T_{i,ped} = 2.35$ keV as

$$W_{ped} = \frac{3}{2} \cdot n_{e,ped} \cdot (T_{e,ped} + T_{i,ped}) \cdot V_{plasma} \quad (2.42)$$

this results in $W_{ELM} \sim 4$ MJ for uncontrolled type-I ELMs. Assuming that during ELMs 60 % of W_{ELM} is transported to the divertor with a distribution of 2:1 in favor of the inner divertor [85,86], 1.6 MJ will be deposited on the inner and 0.8 MJ on the outer. Considering the result of empirical studies revealing that the SOL heat flux width λ_q varies inversely with the plasma current [87], one obtains a wetted area of 1.6 m^2 on the inner and 2.6 m^2 on the outer divertor. This comprises the worst-case scenario for the non-active phase which assumes that the wetted area of inter-ELM and ELM phases are the same [88,89]. More optimistic scenarios predict a broadening of three- to sixfold due to the SOL perturbation during the ELM. For the no-broadening case, the target ELM energy densities can be determined to be $\varepsilon_{tar,Loarte}$ =1.10 MJ/m^2 on the inner and $\varepsilon_{tar,Loarte}$ =0.32 MJ/m^2 on the outer. The estimate for the active case follows on similar arguments.

A model put forward recently, the Eich model for ELM energy densities [90] assumes a direct flux tube connection between the pedestal top and the divertor during an ELM, such that, the width of the peeled-off pedestal layer determines the deposition width in the divertor. This assumption produces an optimistic scaling for the heat flux broadening during an ELM. Based on these assumptions, the Eich model concludes that the peak ELM energy density scales as

$$\varepsilon_{\parallel,Eich} = 6\pi \cdot p_{e,ped} \cdot a_{pol} \cdot \frac{B_{T,OMP}}{B_{p,OMP}} \quad (2.43)$$

where $p_{e,ped}$ is the electron pressure at the pedestal top, a_{pol} is the minor radius of the plasma (corrected for elongation), and $B_{T,OMP}$ and $B_{p,OMP}$ are the toroidal and poloidal magnetic fields at the outboard midplane, respectively. Measurements of $\varepsilon_{\parallel}$ on various tokamaks, namely MAST, AUG and JET (the majority on the outer strike point), when compared with model predictions, were found to lie between $\varepsilon_{\parallel,Eich}$ and 3x $\varepsilon_{\parallel,Eich}$ [90]. While the Eich model was developed to explain heat loads in the outer divertor, measurements of the inner divertor also indicate agreement [90]. For the non-active phase of ITER, the model predicts $\varepsilon_{\parallel}$ =2.5 MJ/m^2 ($\varepsilon_{tar} = 0.13$ MJ/m^2), for the active phase 10 MJ/m^2 ($\varepsilon_{tar} = 0.5$ MJ/m^2).

A comparison of the model predictions for target ELM energy densities on ITER is shown in table 1. In the table, Eich's model is listed with the lower and the threefold upper limits, whereas for Loarte's model, extrapolations are shown for the no broadening and threefold broadening cases. Since the Eich model is technically only valid for the outer divertor, the estimates for the inner divertor are calculated by multiplying the outer divertor estimates by the same in-out ratio as used in the Loarte

ε_{tar} $[\frac{MJ}{m^2}]$		Eich		Loarte	
		Lower limit 1 X	Upper limit 3 X	3 X Broadening	No Broadening
Non-active phase	In	0.41	1.23	0.37	1.10
(W_{ped}=25 MJ)	Out	0.12	0.36	0.11	0.32
Active phase	In	1.78	5.34	3.67	11.0
(W_{ped}=100 MJ)	Out	0.52	1.56	1.08	3.2

Table 1 Comparison of Eich and Loarte model for ITER's target ELM energy densities, the recommended material limit from divertor simulations is 0.15 MJ/m2

extrapolations. Note that even many of the lower estimates are well above the 0.15 MJ/m2 material limit established in the latest ITER divertor tolerance simulation [91]. The substantial differences between the models result from the different scaling of respective relevant pedestal quantities:

- In the Eich model, the ELM energy is solely determined by pedestal pressure $p_{e,ped} = n_{e,ped} \cdot T_{e,ped}$. It assumes comparatively benign decrease of the peeled off layer width during ELMs with plasma current resulting in $\varepsilon_{\parallel,Eich} \sim \frac{B_T}{B_p}$, resulting in considerably lower heat loads in the active phase of ITER compared to Loarte's approach, while the results are comparable in the non-active phase.
- In Loarte's approach, the relevant quantity is the pedestal collisionality $\nu_e^* \sim \frac{n_{e,ped}}{T_{e,ped}^2}$ [51], which determines the ELM size as a fraction of the pedestal energy. While the flux expansion remains constant, the increase of current leads to a reduction of wetted area and net increase with toroidal field $\varepsilon_{\parallel,Loarte} \sim \frac{{B_T}^2}{B_p}$.

These differences in projections for ITER will be exacerbated in predictions for fusion power plants, where low collisionality will be required for sustainment of high bootstrap fractions characteristic of steady state operation [51]. Figure 9 summarizes general material limits on the tolerable energy density $\varepsilon_{\parallel}$ in the divertor found in several material studies (red and black squares) [82,92] and simulation limits based on ITER's material and divertor geometry (blue dot) [91]. The green background indicates the range of expected heat loads for ITER's non-active phase according to the Eich model. 1000 heat pulses by unmitigated ELMs (reached after 1000 s on ITER's natural ELM

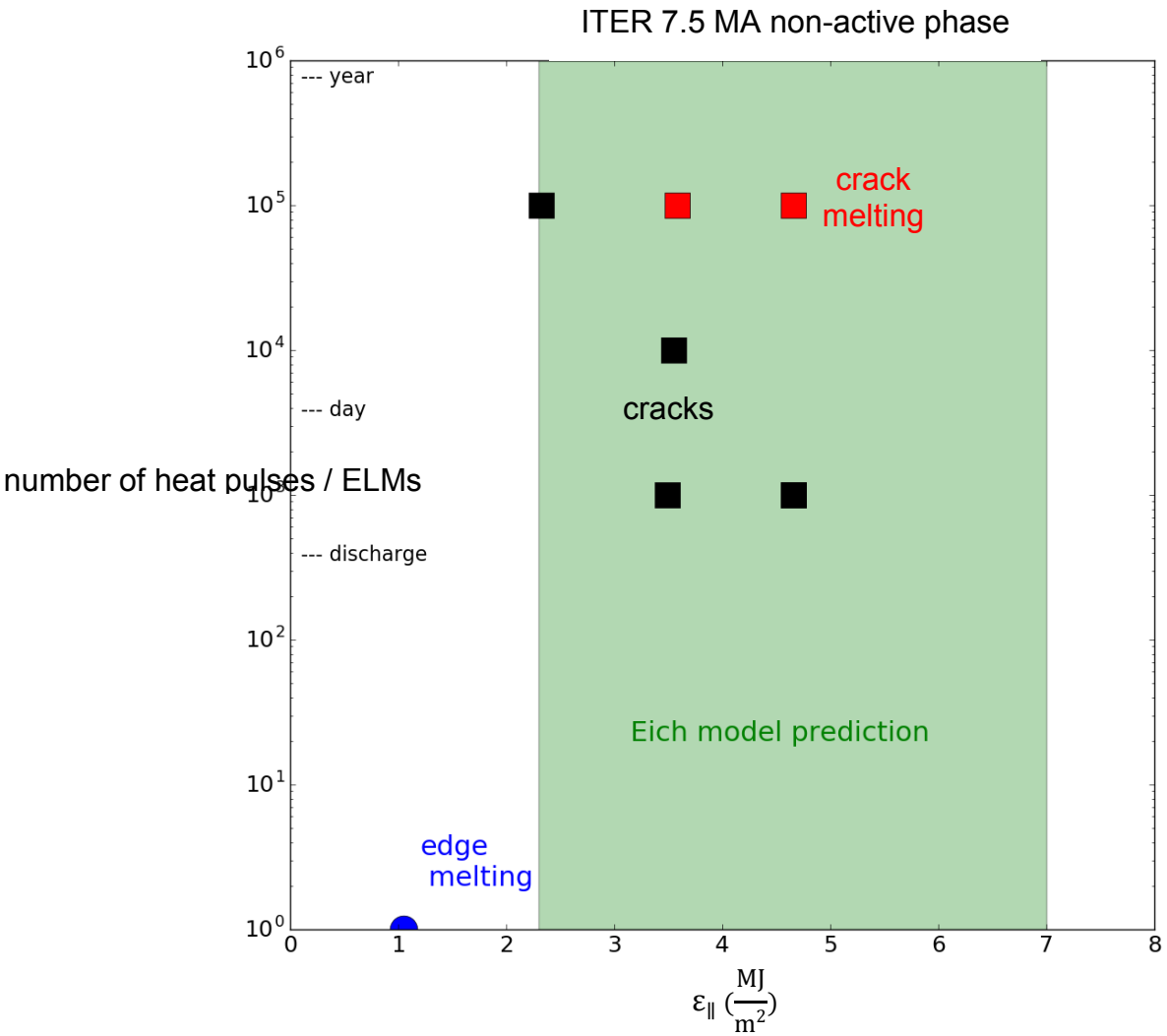

Figure 9 Comparison of ELM energy densities predicted for ITER's outer divertor in the non-active phase according to the Eich model (green background) and limits found in material studies (black/red squares) and simulations (blue dot)

frequency of 1 Hz) will already cause cracks and lead to edge melting in the non-active phase. This number will be reached within a single day of ITER operation given that a full discharge will last up to six minutes. Figure 9 conveys additionally, that exploring what ELM heat loads scale with and progressing in understanding the nonlinear ELM phase is indispensable for designing a benign operational scenario and defining heat flux mitigation requirements. This thesis will show that an important role hereby is played by thermoelectric currents during ELMs.

2.5. Thermoelectric currents

Thermoelectric currents during ELMs have been mentioned in a recent review as potential driver behind additional magnetic field stochastization in the nonlinear phase

[93]. Field stochastization describes a process transforming the ideal nested flux surfaces (as described in chapter 2.1) into randomly wandering field lines. The first measurement of currents in the divertor was reported on JET by Harbor et al. in 1989 using Langmuir probes. Dedicated shunt current resistors connected to tiles isolated from neighboring tiles facilitated more sophisticated measurements on DIII-D and AUG, quantifying the size of the currents. As experimental measurements have shown the existence of an asymmetry in heat flux between the two divertor sides [28,85], the proposed origin of the currents was based on a thermoelectric effect. The hot divertor side is connected through magnetic field lines to relatively colder side. Consequently, a temperature gradient builds up, producing a thermo-current with electrons flowing to the hotter side. Extensive theoretical work on thermoelectric currents by Staebler [94] is briefly summarized here. From plasma transport theory it is known that a current along field lines can be driven by gradients in electron pressure ∇p_e, electrostatic potential $\nabla\Phi$ or temperature ∇T_e along the field line, yielding a parallel current of [95]

$$j_{par} = \sigma\left[\left(\frac{\nabla p_e}{e \cdot n_e} - \nabla\Phi\right) + 0.70 \cdot \frac{\nabla T_e}{e}\right] \tag{2.44}$$

Here e is the elementary charge, n_e the electron density and σ represents the conductivity along the field line. The conductivity is calculated using the collision time τ_{ei}

$$\tau_{ei} = 0.30 \frac{{m_e}^{0.5} {T_e}^{1.5}}{n_i e^4 \ln\Lambda} \tag{2.45}$$

via

$$\sigma = 1.97 \frac{e^2 \cdot n_e \cdot \tau_{ei}}{m_e} \tag{2.46}$$

with m_e the electron mass, n_i the ion density and $\ln\Lambda$ the Coulomb logarithm (assumed here to be 15). There is no pressure difference between OSP and ISP locations linked through field lines during the inter-ELM phase, as all considered discharges are far away from detachment [96], hence the pressure gradient term can be dropped. Detachment describes a scenario in which the SOL density is so high, that the heat flux is considerably reduced, due to interaction with neutrals. One now uses the currents densities at plasma-material interfaces (known from Langmuir probes) as a boundary condition [94]

$$j_{I,O} = \frac{1}{2\sqrt{2}} \cdot e \cdot n_I \cdot c_{s,I,O} \cdot \left[1 - e^{-\frac{e\Phi_{I,O}}{T_{I,O}} + 3.89}\right] \tag{2.47}$$

where c_s the ion sound speeds at inner (I) and outer(O) divertor, respectively and n_I the ion density at the target. The first term of this equation is the ion saturation current $j_{sat,I,O}$. Integrating equation 2.44 along the length of connecting field line L assuming constant σ along the field line, one yields a predicted current of [94]

$$j_{par} = -\frac{\sigma}{e \cdot L} \cdot \left[4.04 \cdot (T_O - T_I) + \ln\left(\frac{(1 + j_{norm})^{T_I}}{[1 - \sqrt{\frac{T_I}{T_O}} \cdot j_{norm}]^{T_O}} \right) \right] \tag{2.48}$$

with $j_{norm} = \frac{j_{par}}{j_{sat,I}}$. Factoring out T_I (which is without loss of generality assumed to be the colder end) and defining $\gamma = \frac{\sigma \cdot T_I}{j_{sat,I} \cdot e \cdot L}$ yields the final result of [94]

$$j_{norm} = -\gamma \cdot \left[4.04 \cdot \left(\frac{T_O}{T_I} - 1 \right) + \ln\left(\frac{1 + j_{norm}}{[1 - \sqrt{\frac{T_I}{T_O}} \cdot j_{norm}]^{\frac{T_O}{T_I}}} \right) \right] \tag{2.49}$$

All units in the equations 2.44 – 2.49 above are in the cgs system. Note that published comments on corrections of the Staebler paper concern the heat flux part and are thus not relevant to this thesis [97]. One can see that in case of no field line temperature gradient ($T_O = T_I$), $j_{norm} = 0$ is the solution to equation 2.49, while the ion saturation current ($j_{norm} = -1$) is the upper limit.

The second part of the experimental work of this thesis (chapter 5) will investigate the questions, whether the measured ELM currents are consistent with the theory of thermoelectric currents, what causes them and what role the currents play during the ELM process.

This completes the review of tokamak basics, H-mode and ELMs. Despite intense study und research efforts there the exact ELM mechanism is not fully understood [19]. Open issues concern the growth evolution in the nonlinear phase and drivers for the instability size. Experiments with detailed measurements are indispensable to elucidate the ubiquitous H-mode phenomenon.

3. The DIII-D tokamak

Fusion research provides the exciting possibility to study the physics of magnetized plasmas in small to large scale experiments on earth. Often times novel and fascinating experimental measurements needed theoretical explanations enhancing understanding. This is why the design of fusion experiments and diagnostics is vital for research progress. The following chapter will give an overview of the DIII-D research facility and the diagnostics made use of in this thesis.

3.1. Machine overview

DIII-D is a mid-size tokamak that is known for its plasma shaping flexibility and large number of diagnostics. Both plasma current and toroidal magnetic field direction can be reversed (Appendix A) providing a large variety of magnetic configurations.

	DIII-D [98]	**ITER** [42,99]	
		non-active	active
R [m]	1.7	6.2	
a [m]	0.6	2.0	
B_T [T]	1.0-2.2	2.7	5.3
I_P [MA]	1.0-2.2	7.5	15
P_{NBI} [MW]	20	34 - 51	
P_{ECH} [MW]	5	20	
Volume [$\mathbf{m^3}$]	18	830	
W_{MHD} [MJ]	0.5 – 3.3	100	350
$\boldsymbol{\delta}$	0.1 - 0.6	0.2	
$\boldsymbol{\kappa}$	1.4 - 1.9	1.9	
$p_{e,ped}$ [kPa]	3 - 15	40	80
$\boldsymbol{\nu_e^*}$	0.1 - 5	0.2	0.1
$\boldsymbol{\rho^*}$ [%]	1 - 8	0.4	0.3
$\mathbf{n/n_G}$	0.2 - 0.6	0.9	
P_{fus} [MW]	0.02	10	500
$t_{discharge}$ [s]	5	600	

Table 2 Typical experimental parameters of the DIII-D tokamak and the ITER design.

For scaling studies, a plasma shape was created on DIII-D, replicating the ITER shape and labelled ITER similar shape (ISS). Relevant machine data is listed in table 2. The large difference in fusion power between ITER's active and non-active phase results from higher temperature, density and the use of tritium instead of deuterium fusion only. The table conveys how difficult extrapolations from present day devices as DIII-D to ITER are. While most dimensionless quantities (δ, ϵ, κ, q_{95}, β_N, ν_e^*) can be matched on DIII-D, plasma size and magnetic field of the ITER tokamak are considerably larger leading to two deviating dimensionless parameters:

- closer proximity to the Greenwald density limit n_G (equation 2.17)
- a smaller normalized gyroradius ρ^* (equation 2.20)

ITER will operate both near the Greenwald limit and in a low collisionality environment. As the Greenwald proximity for a given current can only be raised by increasing the density (by e.g. additional pellet fueling) this competes with achieving low collisionality (see equation 2.28). With Carbon as wall material, DIII-D can obtain very low collisionality plasmas, as there is little high-Z impurity sputtering compared to tokamaks with tungsten walls and lower plasma densities are possible [100]. Consequently, DIII-D is uniquely fit for collisionality dependent extrapolations.
There are research reactors as Alcator C-MOD [101] specializing on high pressure environment (with a record of p_{ped}=70 kPa achieved in a Super H-mode [102]), yet there is no mid-size or larger machine simultaneously achieving high current, field and pressure. Hence, in depth understanding of the physics of transients as ELMs is crucial for extrapolations, since little unfavorable deviations between theory and experiment on contemporary machines could scale up many times towards ITER.

3.2. Diagnostics

Measuring basic properties of a plasma is a great challenge due to the extreme temperatures and conditions, the fourth state of matter exists at in tokamak plasmas compared to usual lab environments. For instance, the ion core temperature in the H-mode example peaks at over 11 keV (Figure 5), ten times hotter than the sun's core. In the following, five out of over seventy diagnostics will be introduced with their principle physics, as they are heavily used for ELM analysis in this thesis. Multiple diagnostics are routinely operated to determine basic plasma properties as for instance an extended set of magnetic probes for plasma stored energy and mode analysis [103,104] and the Motional-Stark-Effect polarimeter (MSE) [105] for constraining the plasma current profile. A compelling overview of many tokamak diagnostics in more in-depth treatment is given in [106].

3.2.1. Thomson Scattering

This diagnostic forms the backbone of most profile and stability analysis since it robustly delivers electron temperature and density at multiple locations. The physics

principle taken advantage of is the scattering of electromagnetic waves on particles, yielding a cross section of

$$\sigma = \frac{8\pi \cdot (Z_X e)^4}{3 \cdot (4\pi\varepsilon_0 m_X c^2)^2} \tag{3.1}$$

with Z_X, m_X charge and mass of species X [107]. The strong mass dependence m_X^{-2} leads to an electron dominated scattering. The electron density can be calculated using the integrated intensity of the scattered waves and the temperature can be deduced from Doppler broadening. The incident electromagnetic waves are generated by lasers, the DIII-D Thomson system (Figure 10) operates with 10 Nd:YAG lasers firing at 20 Hz

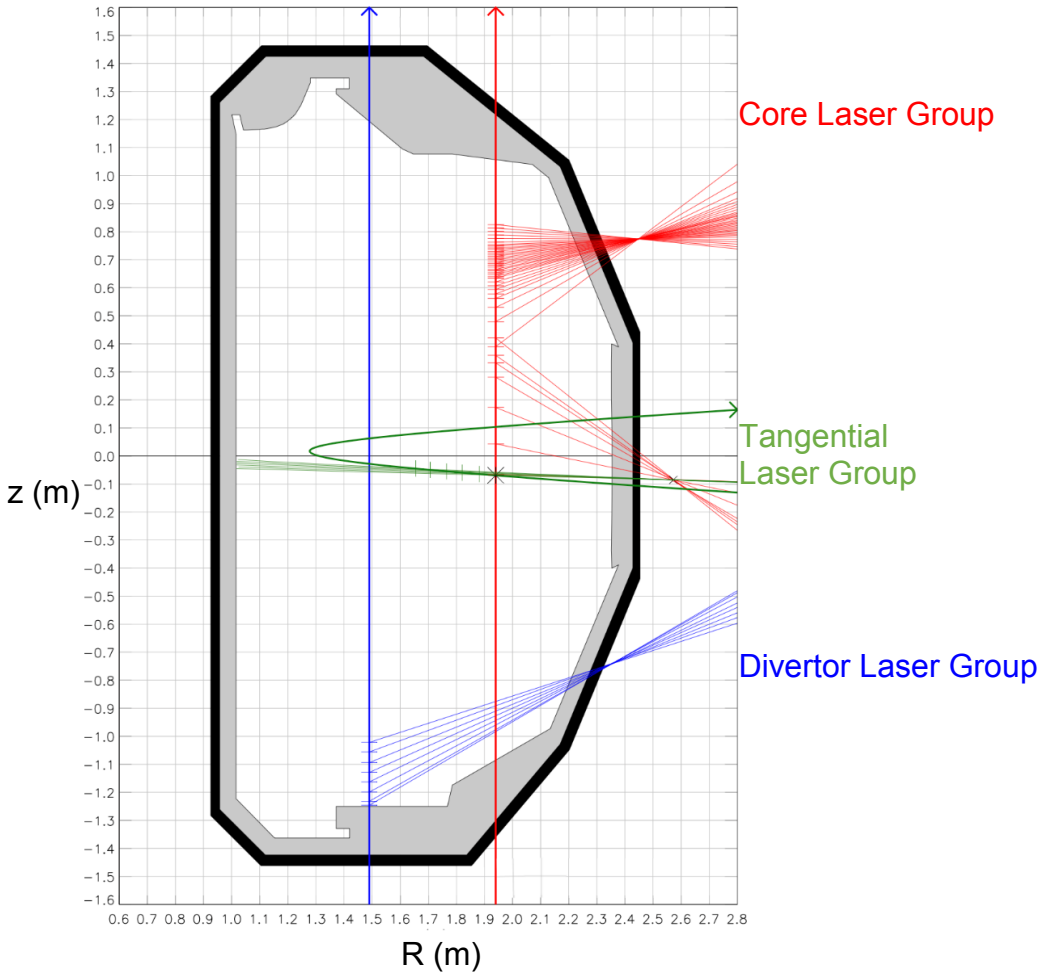

Figure 10 Thomson lasers and measurement points on DIII-D

or 50 Hz from three different locations [108]:

- 7 vertically down into the plasma at 1.94 m radius, to facilitate high edge resolution temperature measurement (red)
- 2 tangentially near magnetic axis (green)
- 1 along the divertor path (blue)

Contemporary, the diagnostic yields a total of 54 measurement points [109]. For a higher time resolution during the ELM studies, the Thomson laser system can be set to fire in 'bunch'-mode, i.e. instead of firing the lasers in equidistant time steps, the diagnostic is programmed to fire the lasers back to back in short time intervals followed by a comparatively longer pause.

3.2.2. Charge Exchange Recombination

Ion temperature, rotation and density are determined using charge exchange recombination (CER). This diagnostic relies on plasma heating via neutral beam injection. The neutral beams produce excited, hydrogen-like ions through the exchange of an electron between the previously neutral beam atoms D^0 and fully stripped light ion impurities I^{+Z} via

$$D^0 + I^{+Z} \rightarrow D^+ + I^{+(Z-1)*} \rightarrow D^+ + I^{+(Z-1)} + h\nu$$

The excited ion $I^{+(Z-1)*}$ then promptly undergoes level transitions, emitting photons with energy $h\nu$. An electron can leave a highly excited state only via several steps to the ground state, whereby photons of known and convenient wavelength are emitted. This is due to the selection rules for the azimuthal quantum number l, stating $\Delta l = \pm 1$. At DIII-D, carbon atoms are present as impurities, because of their abundance in the wall material[6]. The CER diagnostic uses the transition of the excited electron to determine the velocity (via Doppler shift), temperature (via Doppler width) and density (via total volumetric emissivity) of the impurity ion species emission spectrum. Obtaining the correct ion properties is difficult, because there are several other effects that can lead to spurious measurements, for instance additional sources of radiation at the same wavelength: the plasma background radiation, bremsstrahlung and radiation from impurity ions that recombine and do not emit the photon promptly but with a certain time shift. Properties of deuterium - the main ion species on present day tokamaks - are usually deduced from or assumed to be equal (in case of temperature) to impurity ion properties. Direct CER measurement of main ions has become available only recently [110], showing that main ion temperature profiles can have larger edge gradients than carbon on DIII-D [111]. The CER cameras are taking 2000 spectra per discharge on DIII-D [112]. In standard setting, a rate of 200 Hz is used to cover a time span of 10 s. During most discharges in this work, the CER timing was set to faster sampling rates, ranging between 2.5 ms time exposure time (400 Hz) down to 0.5 ms (2 kHz).

3.2.3. IR Thermography

Heat loads on the divertor emitted by the plasma are measured via infrared thermography (IR). The physics principle IR is based on is Planck's Law of black body

[6] In particular the Carbon C^{+5} transition with 529,05 nm is a dominating radiation source.

radiation [113]. As the divertor is not an ideal black body, a correction factor ϵ, the emissivity, is introduced defined as ratio of de facto emitted power to power emitted by an ideal black body. A gray body of temperature T will hence radiate the power

$$P_{\lambda}^{BB} = \iint \epsilon \cdot \frac{2\pi hc^2}{\lambda^5} \cdot \frac{1}{e^{\frac{hc}{\lambda T}} - 1} \, d\lambda dA \tag{3.2}$$

where h is the Planck constant, λ is the respective wavelength and dA is the differential solid angle of the observer (here the IR camera system). The integrand is called spectral radiance and depends on λ and T. To avoid saturation and increase measurement accuracy the camera system is designed to be sensitive to photons in a specific wavelength interval by using optical elements as filters and lenses. The photon flux Γ within a limited wavelength range can be calculated as

$$\Gamma \, d\lambda dA = \epsilon \cdot \frac{2\pi c}{\lambda^4} \cdot \frac{1}{e^{\frac{hc}{\lambda T}} - 1} \, d\lambda dA \tag{3.3}$$

Taking into account transmission losses, caused among others by the glass shielding to the vessel, a wavelength response function R (λ) can be composed. The exact solid angle in equation 3.2 can be calibrated by placing a black body radiator in the vessel at the line of sight or during the baking of the machine (in this process the tokamak is heated to a certain temperature to cause evaporation of unwanted impurities and gasses). The reason why sensors tuned to infrared wavelength around 4 µm are used can be found in the strong gradient in the temperature range of 200-1500 K of equation 3.3, resulting in excellent temperature resolution [114]. Knowing spectral angle and response function, the photon count

$$N_{\lambda,cor} = \iint R \cdot \epsilon \cdot \frac{2\pi c}{\lambda^4} \cdot \frac{1}{e^{\frac{hc}{\lambda T}} - 1} \, d\lambda dA \tag{3.4}$$

delivers the temperature distribution T(s,t) for each time step. To obtain the heat flux distribution q(s,t) the measured temperature distribution is compared to the calculated, expected distribution based on heat diffusion of the temperature distribution from the previous time step using the tiles heat coefficient α (determined experimentally, unit $\frac{W}{m^2 K}$)

$$q = \alpha(T_{exp} - T_{calc}) \tag{3.5}$$

T_{calc} is obtained from solving the two-dimensional heat diffusion equation

$$\rho c_p \frac{\partial T}{\partial t} = \nabla \kappa \nabla T \tag{3.6}$$

with heat conductivity κ $[\frac{S}{m}]$, specific heat capacity c_p $[\frac{J}{K}]$ and material density ρ $[\frac{kg}{m^3}]$. A caveat in divertor thermography consists of surface layers on the divertor. In fact, dust deposits with poor heat conduction on the tiles can substantially affect the temperature dynamics, which, if not properly accounted for, can lead to overestimates and, in some cases, negative heat fluxes. In case of the latter, heat dispersion abilities provided by the large surface of the layers are not properly accounted for; in the former case the additional photons emitted by the surface layer atoms are wrongly attributed to the tiles. DIII-D thermography analysis is based on the heat diffusion code THEODOR [115]. The code includes surface layers characteristics through a manual input of α_{surf} into the code, as ratio of heat conductivity κ_{layer} and thickness d of the layer.

$$\alpha_{surf} = \frac{\kappa_{layer}}{d} \tag{3.7}$$

The temperature deduced from the IR measurement T_{IR} is then corrected with respect to the surface layers to obtain T_{exp} for equation 3.7.

$$T_{exp} = T_{IR} - \frac{q}{\alpha_{surf}} \tag{3.8}$$

Since the determination of α_{surf} is crucial for the heat load determination, details for DIII-D can be found in appendix B.

3.2.4. Tile Current Array

The DIII-D tile current array (TCA) has a history of reconfigurations and rededications to address various physics questions. A first poloidal tile current array was constructed on DIII-D in 1991 [116]. Shortly thereafter an extensive upgrade facilitated broad toroidal coverage and higher sampling rates of up to 20 kHz by adding a large number of current sensors [117]. Each of the tiles with a current monitor in the DIII-D divertor is isolated from the other tiles and connected to ground. Each shunt current resistor ($\Omega \approx 2.3$ mOhm) is built in series to the ground cable and regularly calibrated during

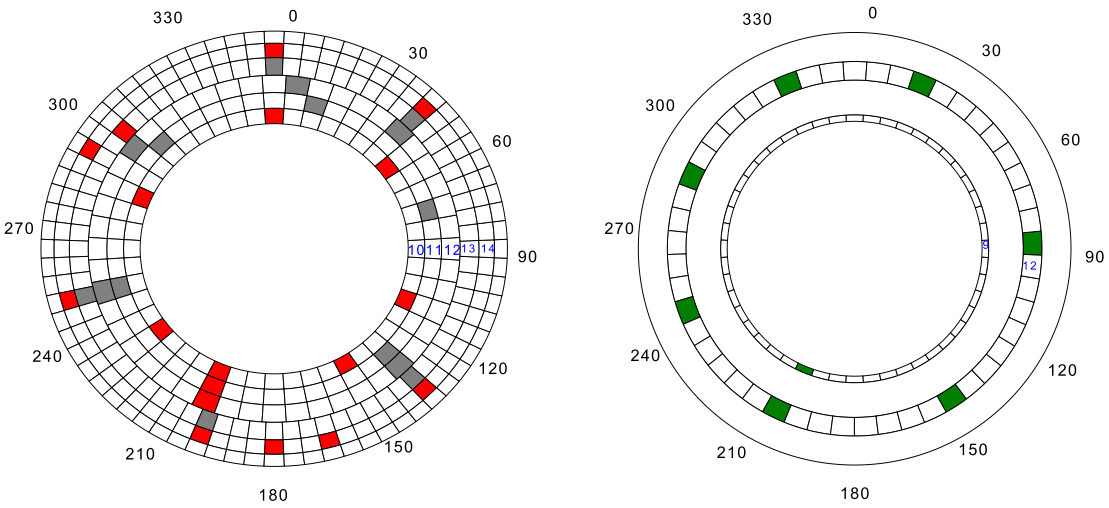

Figure 11 TCA configuration in the lower DIII-D divertor (left), red tiles indicate tiles with current monitors used in this thesis (unused sensors in grey), machine coordinates are listed for orientation. The upper divertor TCA (right) is less wide and availability of measurement data rare.

vents by manually applying a small voltage to the respective tile. Between 2001 and 2003 fast digitizers were installed on the array delivering sampling frequencies of 200 kHz (and up to 500 kHz in some cases), ideal for ELM measurements. The duration of a typical ELM-related current flow amounts to 1.5 ms, which corresponds to 300 measurement points at 200 kHz sampling frequency. The tile current array in this configuration is shown in figure 11. The shunt current resistors are attached to tiles, which are arranged in 5 concentric circles in the lower divertor. The diagnostic tiles used for the analysis in this thesis are shown in red; grey color indicates unused tile sensors. Regarding the nomenclature, the tile rings are labeled by numbers, with the innermost being 9 and the outermost 14. The tile current monitors are then termed through their machine coordinate and the respective divertor (upper (A) or lower (B)), so that 10B200 refers to the tile current monitor in ring 10 of the bottom divertor at machine coordinate 200° (machine coordinates are oriented clockwise, with 0° being north). By design, particularly good coverage is available near the standard strike-point locations. In ring 10, the typical ring of the inner strike point, 7 out of 48 tiles have fast current monitors and ring 14, the equivalent for the outer strike point, 8 out of 72 have fast current monitors. Note that due to data storage constraints the availability of fast digitized TCA measurements away from the strike points is often limited. There are additional slow only digitized tiles, but due to the limited sampling frequency of 10-20 kHz, these are not useful for ELM measurements.

In 2005 the DIII-D divertor was remodeled, extending the elevated shelf structure in the outer divertor to smaller major radii R. The tile current array diagnostic was reduced in size due to port space constraints and re-purposed to disruptions, implying a reduction of the number of measurement points in the lower divertor from 40 to 10, a lower current sensitivity to measure larger currents and a lower signal to noise ratio.

Hence, this configuration is not useable for detecting smaller current changes during the ELM onset and restricted to n<3 toroidal variations. However, it is used in this thesis to compare the tile current measurements to diagnostic measurements only available after the divertor remodeling (e.g. fast IR data, higher frequency magnetics). The contemporary configuration of the array is limited to two circles in the lower divertor in proximity to the outer strike point (OSP). The sensors are localized on an elevated shelf structure in what approximately corresponds to circles 13 and 15. Of particular interest are TCA 13B068 and TCA 15B060, as they are in the toroidal vicinity of the 60-degree IR camera on DIII-D.

4. Divertor heat loads

In order to answer the physics questions for the scaling of heat loads raised in the beginning of this thesis and broaden the understanding of the nonlinear ELM phase, suitable datasets consisting of controlled variation of independent parameters are needed. Since DIII-D is a large experiment with annually limited run time, all data taken by diagnostics for each discharge is routinely stored in a MDSplus database system [118]. If suitable data cannot be found in this database, an application detailing the novelty of the experiment has to be filed and run time will be allocated, if responsible councils approve. In the frame of this thesis, an experiment on ELM heat load scaling was conducted while the physics of the ELM currents were analyzed based on previous discharges. This chapter presents scaling of heat loads with plasma parameters on DIII-D, a comparison to Eich's and Loarte's model and other findings on the nonlinear ELM phase. In the following, the setup and results of the heat load experiment will be introduced and presented.

4.1. Experimental scenario

For scaling analysis towards ITER and future power plants it is common to work with multi-machine databases in order to increase the parameter ranges. This has also been done in the Eich model for ELM energy densities, as it's based on data from AUG, JET and MAST [90]. Testing this model on DIII-D is interesting due to the tokamak's unique ability to provide highly shaped, low collisionality plasmas. Higher shaping improves peeling-ballooning stability allowing the access to higher pedestal pressures (see section 2.4). Isolating the potential drivers behind larger ELM sizes – collisionality as proposed by Loarte [21], respectively pedestal pressure according to Eich [90] - in a parameter scan as far possible is one objective of the experiment to understand their individual role. Additionally, the influence of pre-ELM conditions on the ELM crash and quantities associated with the nonlinear phase such as divertor heat load should be investigated.

A simple approach to a heat load scaling experiment is to conduct a continuous current ramp, that is run the same discharge scenario and increase the plasma current discharge by discharge. From DIII-D operational experience, it is known that at constant toroidal field the density traces the current (i.e. higher densities will be achieved at higher currents), hence a linear rise in plasma pedestal pressure is to be expected. However, this approach has two disadvantages: First, increasing only the current will affect non-dimensional parameters as the safety factor (equation 2.18) and the normalized toroidal ion Larmor radius ρ^*, which themselves can influence ELM sizes and the likelihood of

core mode activity [119]. Secondly, too large of a pedestal density will lead to a transition into a type II ELM regime (see figure 8) and to partial divertor detachment (as explained in chapter 2.5).
To avoid influence of undesired codependences the idea was to execute a non-dimensional collisionality scan, i.e. keeping dimensionless parameters other than collisionality constant by varying plasma current, magnetic field and heating power accordingly. As $\rho^* \sim \frac{\sqrt{T}}{B}$ (equation 2.20) and $\beta_N \sim \frac{nT}{B^2}$ (equation 2.16), it is necessary to keep the ratio of temperature and magnetic field $\frac{T}{B^2}$ and the density n constant for ions and electrons by adjusting the heating power [120]. Additionally, the ratio of plasma current and toroidal field needs to kept steady to avoid changing the safety factor q_{95}. To guarantee attached divertor conditions for accurate heat load measurement and remain at ITER relevant low collisionality, it was aimed to keep the pedestal electron density n below $4.0 \cdot 10^{19} m^{-3}$. With the density being limited, very high temperatures are required to get to high plasma pressures. For this purpose, up to 3.5 MW of electron cyclotron heating (ECH) power were injected into the outer plasma core and edge (ψ_N =0.65-0.92), achieving pedestal electron temperatures in excess of $T_{e,ped}$=2 keV. ECH does not inject additional particles as NBI heating does, but rather leads to a pump-out of density due to changes in turbulence [121]. Both the density pump-out and increase of pedestal temperature contribute to reducing collisionality.

	Low collisionality	**Medium collisionality**	**High collisonality**
$\mathbf{B_T}$ [T]	2.15	1.80	1.60
$\mathbf{I_P}$ [MA]	1.50	1.26	1.12
$\mathbf{P_{NBI}}$ [MW]	1.6 - 5.0	1.6 - 5.0	1.6 - 3.0
$\mathbf{P_{ECH}}$ [MW]	0 - 3.5	1.6 - 2.3	0 - 2.2
$\boldsymbol{\nu_e^*}$	0.05 - 0.75	0.13 - 0.34	0.45 - 2.17
$\mathbf{f_{ELM}}$ [Hz]	7 - 47	14 - 31	8 - 43
$\mathbf{p_{ped}}$ [kPa]	4.2 - 6.5	3.9 - 7.8	3.1 - 4.8
$\boldsymbol{\beta_{n,ped}}$	0.45 - 0.56	0.47 - 0.91	0.52 - 0.72

Table 3 Operational overview of three-point collisionality scan

Since collisionality scales with $\frac{n}{T^2}$, lowest collisionalities are obtained at high temperatures. As $\frac{T}{B^2}$ and n are kept constant in the scan, the collisionality strongly scales with the field strength $\nu_e^* \sim \frac{1}{B^4}$. Due to limited run time, it was decided to run three-point

scans, i.e. obtain conditions at the extremes (very high / low pressure) first and finalize the data collection with a state in between. An overview of operational conditions and obtained plasma parameters in this three-point scan is shown in Table 3. Regarding the plasma shape, a modified lower single null plasma was chosen with a lower triangularity of 0.74-0.78, an upper triangularity of 0.33-0.39 and an elongation κ of 1.77-1.80, close to the ITER similar shape (ISS).

A combination of NBI and ECH power steps was implemented within each discharge to investigate a wide variety of pedestal conditions. The NBI power was varied between P_{NBI}=2.0-5.0 MW yielding β_N=1.5-2.2, and an edge safety factor q_{95}=4.0-4.4. The principle success of realizing the designed scenario can be seen in the comparable ELM frequency and $\beta_{n,ped}$ obtained during the experiment with very low pedestal collisionalities down to 0.05. The reason for the high pedestal pressures in the medium regimes will be discussed in the following segment.

In order to extend the dataset and to include variations of plasma shape from the modified ISS (e.g. shapes with lower triangularity), data from eight NBI heated H-mode plasmas from previous experiments [122,123] was included in the analysis. All discharges have type-I ELMs and IR data on inner and outer divertor. They cover the following ranges: P_{NBI}=1.5-6 MW, β_N=1.2-2.5, δ=0.3-0.6, B_T=1.7-2.1 T, I_P = 1.1-1.6 MA, and q_{95}=3.1-4.4. υ_e^* ranges from 0.3 to 1.2. In comparison to the newly conducted experiment, the average density and collisionality is higher in the previous discharges. It is clearly stated when and how previous data is added to the analysis.

4.1.1. Design of the experiment

The shape and evolution of a medium-collisionality discharge are shown in figure 12. After the LH transition the outer strike point (OSP) was programmed to move inwards, i.e. away from the cryo-pump baffle (black shape to green shape). This procedure allowed taking advantage of better density pump-out before the L-H transition (due to proximity of the OSP to the cyro-pumps, which are below the engaged divertor shelf on DIII-D) while monitoring both strike points simultaneously with the fast-infrared television camera (IRTV) in the H-mode. As can be seen from the figure, the OSP would not be visible to the IR camera without the shape change, since the shelf of the outer divertor is in line of sight in pumping position, creating an IR shadow region. The discharge trajectories display the power steps in P_{NBI} at t=2.0 s and P_{NBI} and P_{ECH} at t=3.5 s (c). The change of the stored energy at 3.5 s (a) is a response to the heating power change. The density pump-out effect of the ECH can be seen at t=3.5 s, when both line-averaged and pedestal electron density increase after the ECH is switched off (b). Here, three quasi-stationary intervals with different pedestal conditions were obtained: 1.5 - 2.0 (only inner divertor IR data), 2.2 - 3.4 s (ECH and NBI) and 4.3 – 5.0 s (NBI only). $p_{e,ped}$ remains approximately constant at ECH turn-off, with the increase in density resulting from the loss of ECH pump-out balancing the decrease in temperature resulting from cessation of ECH heating (d). While pedestal pressure remains stable, the density increase and the temperature decrease at 3.5 s cause a rise

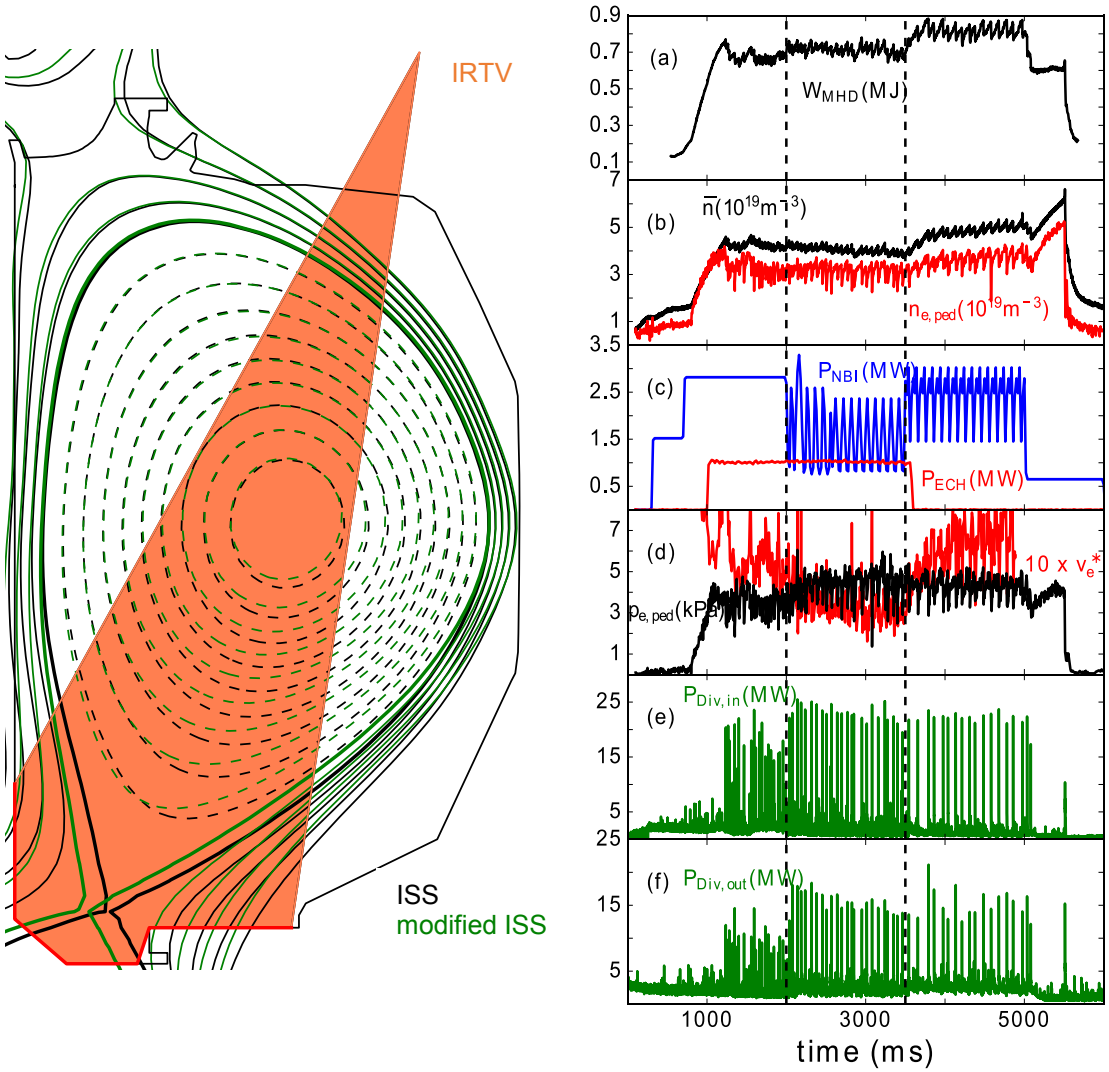

Figure 12
Left: ITER Similar Shape (ISS) and modified shape for monitoring both strike points with the DIII-D fast IR camera. IR covered range shown in red
Right: Evolution of discharge 169430 (1.6 T, 1.12 MA) with: a) stored MHD energy of the plasma b) line-averaged (black) and pedestal electron density (red) c) injected power with NBI (blue) and ECH (red), d) pedestal pressure and electron collisionality at the pedestal (multiplied by a factor of 10), e) inner and f) outer divertor power.

in collisionality (d). The frequency of the ELMs decreases, whereas the absolute size only changes marginally. In this discharge the power in the inner divertor during ELMs is about 5 MW higher than the power arriving in the outer divertor (e,f). Typically, two to three time segments with stationary ELM cycle conditions (defined by small variations in f_{ELM} and $p_{e,ped}$ before ELM crash) were obtained per discharge, each lasting at least 0.5 s. Strong heating power in the first segment ensured a stable L-H transition and high-quality data with beam-dependent diagnostics (most important: CER and MSE). The last segment in the discharges, when the input power was typically dropped to P_{inj}= 2.5 - 3 MW, allowed investigation of conditions close to the LH-power threshold.

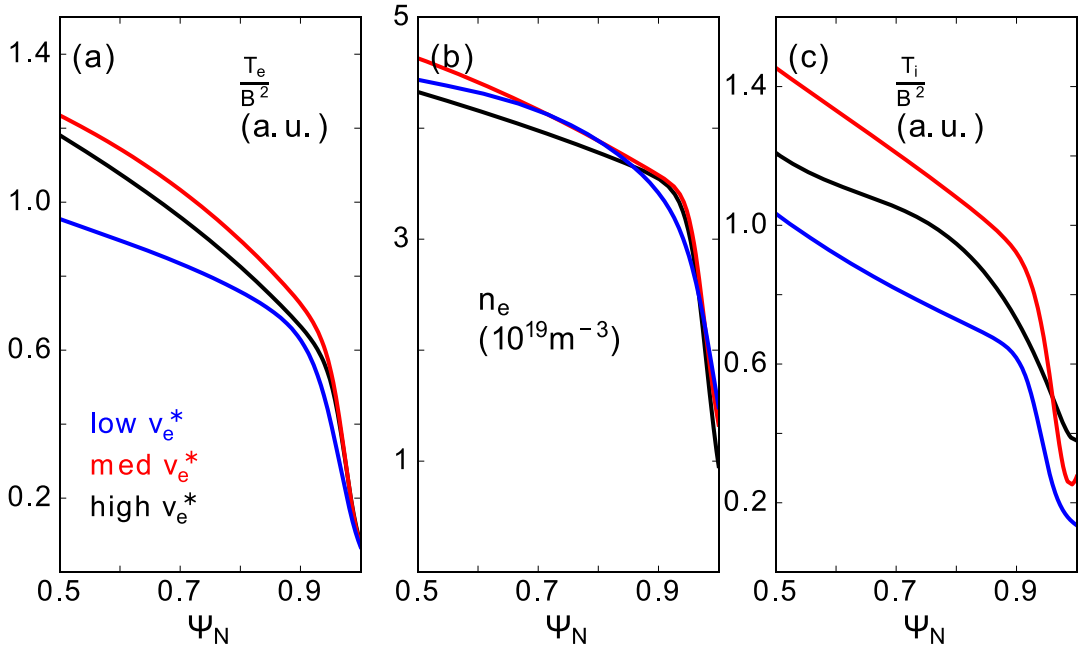

Figure 13 Profile overview in the outer plasma for the three-point non-dimensional scan: a) normalized electron temperature b) electron density and c) normalized Ion temperature. While the density match is good, there are discrepancies in the temperature channel: For a better match the low collisionality case (blue) would require stronger heating, which was avoided to obtain lower ELM frequencies for better diagnostic resolution.

Throughout the experiment, a relatively good match of non-dimensional parameters was obtained as exemplified by figure 13, where kinetic profiles of electron and impurity ion temperatures normalized to B^2 (a, c) and electron pedestal densities (b) are compared in ψ_N-space. One representative of each collisionality point is selected. The electron density profiles (b) agree well. Both the normalized electron and especially the ion temperature profiles show that the low collisionality case (blue, 2.15T) has lower normalized temperature values than required for perfect non-dimensionality match. The discrepancy exemplifies a common operational issue, i.e. the conflict of competing effects between increasing the power to improve the profile match and undesirable high ELM frequencies due to the rise in SOL power. High ELM frequencies come with lower ELM energies and reduce the ELM size determination accuracy, as for instance inter-ELM and ELM phase are more difficult to distinguish. Additionally, the natural ELM frequency expected for ITER is below 10 Hz imposing the objective of low ELM frequencies in comparisons to mimic ELM dynamics [21]. In high collisionality plasmas, there is a competition between lowering the heating power correctly with field and current and having enough beam power to maintain the beam dependent diagnostics, such as CER. As consequence of these competing goals, the pedestal beta in general reached higher values in the medium and high collisionality phase than desired for an ideal scan (Table 3).

4.1.2. Exemplary results

As an example, the results of the ELM IR thermography data analysis are shown for a low collisionality plasma (169426) in figure 14. The five largest ELMs in the selected time interval t=4.4 - 5.0 s display very similar temporal evolutions of the peak heat flux q_{peak} on inner (a) and outer divertor (b). The time coordinate represents the time relative to the ELM heat flux peak. Figure 14c and d show the radial profiles of heat flux at the time of peak. q_{peak} in this example is higher on the inner divertor than on the outer (25 MW/m^2 vs 18MW/m^2), whereas the decay is slower on the outer divertor. Thus, the resulting target and parallel ELM energy densities are comparable (e, f). Note that due to uncertainties in the equilibrium construction during the ELM part of the heat flux from the outer divertor is mapped in the private flux region [36]. As the ELM energy density lacks a normalization to the integration time, it is important to define a standard for determining time integration limits. In accordance with [90] the time limits are determined by a drop to $\frac{1}{e^2}$ of the peak power value relative to the background heat flux and yield divertor ELM durations between 0.9 ms and 1.6 ms on DIII-D (dashed

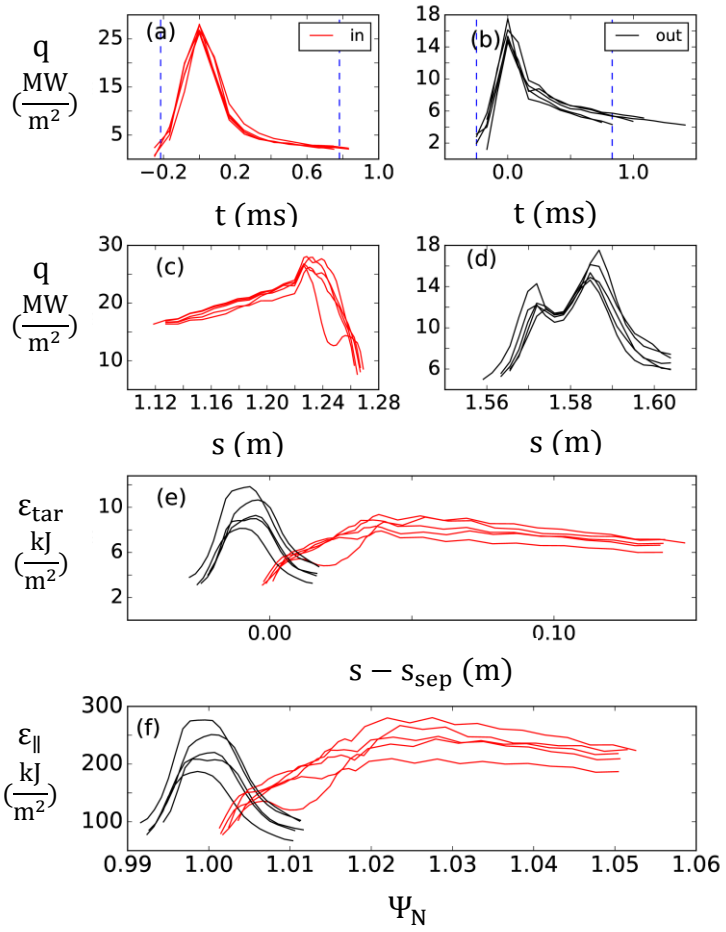

Figure 14 Overview of inner (red) and outer (black) divertor ELM energies during discharge 169426: peak heat flux vs time for inner (a) and outer divertor, (b) peak heat flux vs location along IR measurement path s for inner (c) and outer (d) divertor, target ELM energy densities relative to separatrix location (e) and parallel ELM energy densities in flux space (f).

blue lines in (a) and (b)). In general, the standard deviation for the peak parallel ELM energy densities is below 35 % for all time-intervals used in the analysis. The time evolution of four different ELMs on various diagnostics covering the SOL and the divertor is shown in figure 15. High collisionality discharges (black, blue) are compared to mid-collisionality plasma (green, red). The magnetic perturbation is typically the earliest indicator for the energy loss of the plasmas through an ELM (a). During the onset period of the ELM – and before considerable increase in heat flux in both divertor legs (e, f), there is a spike in the divertor tile current of up to 500 A, as measured by a

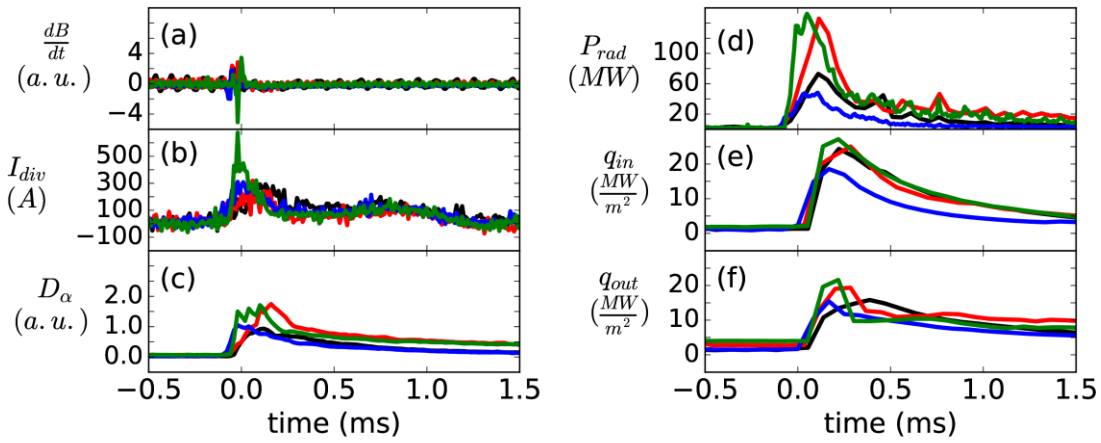

Figure 15 Time evolution of an ELM in discharges 169431 at 2.4 s (green), 169432 at 2.7 s (black), 169433 at 3.0 s (blue), 169434 at 3.0 s (red): a) Magnetic midplane toroidal array signal, b) tile current array measurement, c) D-α trace, d) radiated power during ELM, e) heat flux towards inner divertor, f) heat flux towards outer divertor.

tile current array sensor (TCA) with a sampling rate of 100 kHz (b). The role of the current in the nonlinear ELM phase will be inspected in chapter 5. The particle losses across the last closed flux surface into the SOL are accompanied by an increase in D_α line radiation (c) and a sharp spike in SOL radiation (d). While the D_α and the heat flux measurements appear approximately comparable in size, the mid-collisionality plasmas in this example have more than twice the peak radiation power of the high collisionality discharges and consequently a larger ELM size W_{ELM}. The relation between plasma losses and divertor energies will be investigated in the following section.

4.2. Plasma energy and heating overview

In order to investigate the dependence of the parallel ELM energy density $\varepsilon_{\parallel}$ on υ_e^* and $p_{e,ped}$, quasi-stationary time intervals in the respective discharges of the heat load experiment were selected. They are operationally characterized by different magnetic configuration and heating power. In total, twelve discharges with 27 ELM-data time windows form the base of the analysis, each window with different plasma edge conditions. For each time window, kinetic equilibria were reconstructed with the EFIT

discharge B_T (T)	t (s)	$\pm\Delta t$ (s)	P_{ECH} (MW)	P_{NBI} (MW)	f_{ELM} (Hz)	W_{MHD} (MJ)	W_{ELM} (kJ)	$\frac{W_{ELM}}{W_{MHD}}$ (%)
169425 2.15	2.8	0.25	3.3	3.7	22	1.09	60	5.5
	3.2	0.2	3.3	3.8	45	1.04	59	5.6
	4.2	0.4	2.1	0.6	21	0.73	59	8.1
169426 2.15	4	0.35	3.3	1.9	35	0.81	61	7.5
	4.7	0.3	3.3	1.9	33	0.81	73	8.9
169427 2.15	1.8	0.2	3.5	4.6	67	1.18	23	1.9
169430 1.6	1.8	0.25	1	2.8	20	0.67	43	6.5
	2.9	0.55	1	1.5	17	0.71	62	8.7
	4.3	0.55	0	2.4	11	0.81	83	10.2
169431 1.8	2.4	0.2	2.2	4.3	14	1.14	95	8.4
	3.2	0.24	2.2	4.3	21	1.00	81	8.1
	4.3	0.55	2.2	1.6	27	0.70	68	9.7
169432 1.6	2.7	0	0	1.3	10	0.54	68	12.5
	4.3	0.4	0.6	2.4	7	0.76	87	11.4
169433 1.6	1.8	0.25	1.1	2.8	25	0.66	43	6.6
	3	0.75	1.1	1.3	7	0.66	70	10.6
	4.8	0.55	1	2.4	15	0.46	62	13.5
169434 1.8	2.3	0.2	1.7	5	14	1.17	99	8.5
	3	0.48	1.7	4.8	18	1.07	102	9.6
	4.2	0.35	1.3	1.3	19	0.62	56	9.0
169508 2.15	2.8	0.65	3.3	4.5	17	1.19	28	2.4
	4	0.2	3.3	1.7	22	0.92	66	7.2
	4.8	0.25	3.3	1.7	38	0.76	47	6.1
169509 2.15	3	0.4	0	4	14	1.22	85	6.9
	4.2	0.35	0	1.4	4	0.99	89	9.0
169510 2.15	2.2	0.25	3.2	4.6	20	1.12	35	3.1
	3.1	0.3	0	4.5	10	1.27	89	7.0
	4.2	0.35	0	1.7	16	0.95	59	6.2

Table 4 Selected discharge time windows with heating powers in MW, ELM frequencies and sizes. Rows in grey mark time windows with relative ELM sizes above 9 %.

code [35], using experimental profiles selected in the 80-99 % inter ELM phase. Pedestal profiles are fitted using the standard hyperbolic tangent functions [50]. Since the accuracy of the ELM energy determination is greatly reduced for smaller type I ELMs at frequencies $f_{ELM} > 60$ Hz, only time windows where $f_{ELM} < 60$ Hz were retained. Compound ELMs are not included in the analysis presented in this chapter.
Table 4 compares the average value of a selection of plasma parameters for the time intervals of interests, in particular the ELM frequency, the plasma energy loss W_{ELM} and the relative ELM size to the total plasma energy. W_{ELM} is obtained as an average over all type-I ELMs in the respective time window. An interesting pattern conveyed in table 3 is that the increase of relative ELM sizes above 8 % correlates with decreases in heating power, as shown by rows highlighted in grey. The energy range of W_{ELM}=23-102 kJ is typical for type-I DIII-D ELMs.

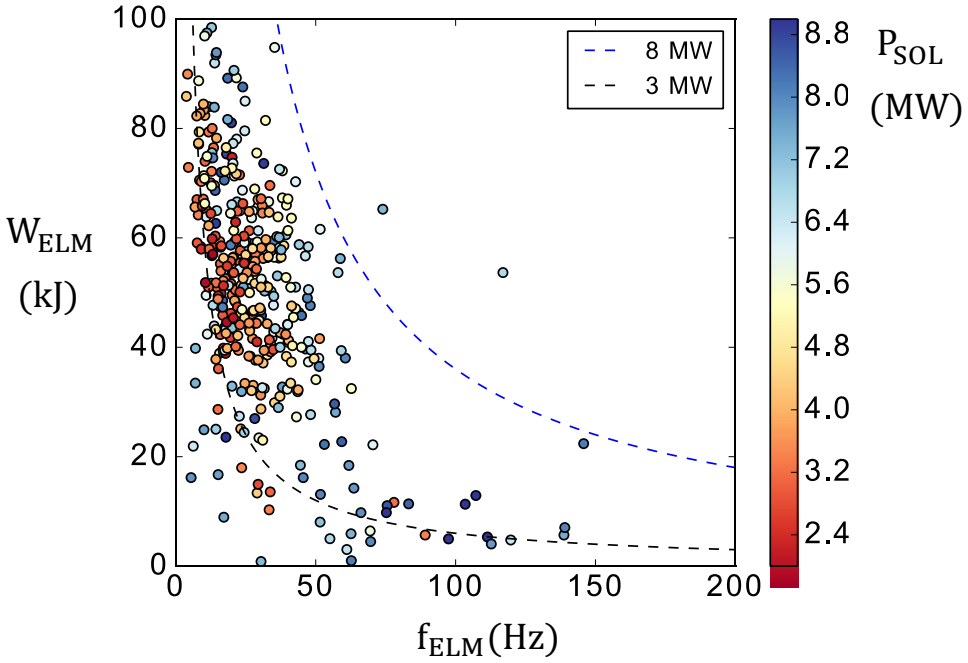

Figure 16 Overview of type-I ELM energy losses W_{ELM} and their dependence on ELM frequency f_{ELM} and power in the scrape-off-layer P_{SOL}. Prediction of upper (blue) and lower (black) limit for ELM dissipated power during the experiment as explained in text.

An overview of all obtained type-I ELMs during this experiment (including the ones not considered for the ELM scalings due to $f_{ELM} > 60$ Hz) in frequency – size space is illustrated in figure 16. The figure shows each singular ELM's dependence on the SOL power P_{SOL} (equation 2.35). Since the plasma is in a stationary state during the inspected time intervals, there were no changes in plasma energy other than ELM losses, so $\frac{dW}{dt}$ was ignored in the P_{SOL} sum. The black and blue dashed lines in figure 16 represent lower and upper limits to the ELM loss power space for the experiment (equation 2.31). The dashed blue line assumes 8 MW of SOL power (for the high heating phases) and

an ELM loss power of 40 % (c=0.4), whereas the black dashed line assumes 20 % ELM loss power of 3 MW SOL power (c=0.2). The distribution of data points in the f-W space confirms the characteristic behavior of type-I ELMs. In particular, nearly no high frequency ELMs with large size are observed.

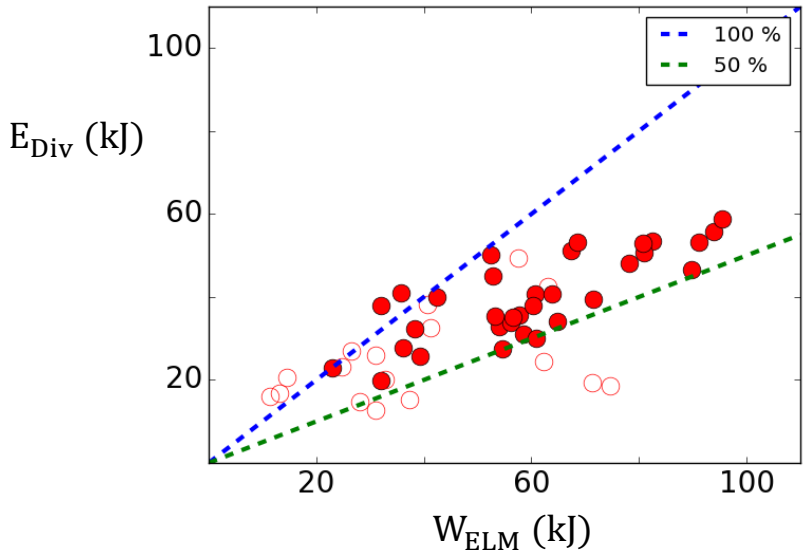

Figure 17 ELM loss energy in kJ vs ELM energy measured in the divertor for all time intervals considered in the experiment. The dashed lines limit the expectancy cone between 50 % (green) and 100 % (blue) of ELM energy arriving in the divertor. Measurements from previous experiments are distinguished by non-filled markers to demonstrate the generality of the dataset.

For each ELM, an energy balance can be computed by comparing the plasma energy loss W_{ELM} with the energy arriving in the divertor E_{div} and radiation energy measurements. An overview is shown in figure 17, where E_{div} is plotted as a function of the W_{ELM}. Each data point in the figure represents the average type-I ELM energy in a time window with stationary plasma conditions. Here E_{div} is the sum of energy arriving during the ELM in the inner and outer divertor. While for ELMs with $W_{ELM} <$ 30 kJ most of the energy is transported to the divertor, the maximum of E_{div} for ELMs with $W_{ELM} >$ 60 kJ remains around 60 kJ, indicating divertor energy saturation at levels of 40-60 % of W_{ELM} for large ELMs. This result is in quantitative agreement with previous measurements of ELM energies on other tokamaks [85,86]. Radiative energies were measured to be between 26 kJ and 50 kJ, so that the sum of radiation energy and divertor energy approximately equals the plasma energy loss, proving consistency of the ELM energy balance. An example for different radiation energies with similar divertor energy deposition was illustrated in figure 15.

4.3. Comparison to Eich model

The comparison of the experimental DIII-D data (both new and retrieved from database) and the Eich model prediction is shown in figure 18. As discussed previously,

the model predicted values are obtained from experimental profiles in kinetic equilibrium reconstructions. The experimental values in figure 18 are computed by averaging the IR heat flux measurements over the five largest ELMs in the respective time-interval. Within a significant scatter, the DIII-D dataset, as a whole, appears to be

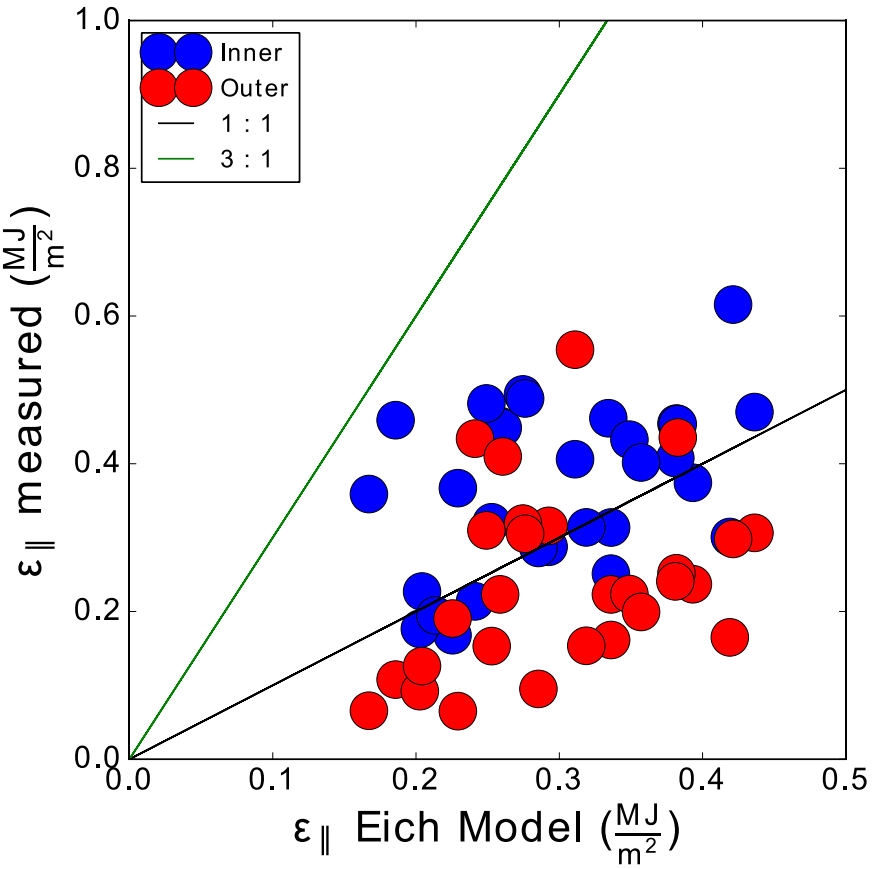

Figure 18 Measured peak parallel ELM energy densities vs. Eich model on DIII-D. Each circle represents averaged data obtained from a 0.5 s-1.5 s time window.

consistent with the model regarding no violation of the upper boundary formed by three times the model prediction value.

The peak parallel ELM energy density is slightly higher on the inner divertor, which in most cases is due to a higher target heat flux on the inner divertor (as shown in the IR data example in figure 14). The average ratio of peak heat flux on the inner to outer divertor is 1.1 : 1 during the experiment described in this thesis. The experimental data range is found to lie between half and two times the model prediction. The lines in the figure are 1 and 3 times the model prediction encompassing the range of data seen on AUG and JET.

Understanding this spread in the multi-machine comparison to the Eich model is an important open question, since it might be associated with one or more hidden variables not included in the model. The dependence of ELM energy density on ELM size W_{ELM} will be investigated in the remainder of this section as possible causes of the data spread around the model prediction. The correlation between peak parallel ELM energy

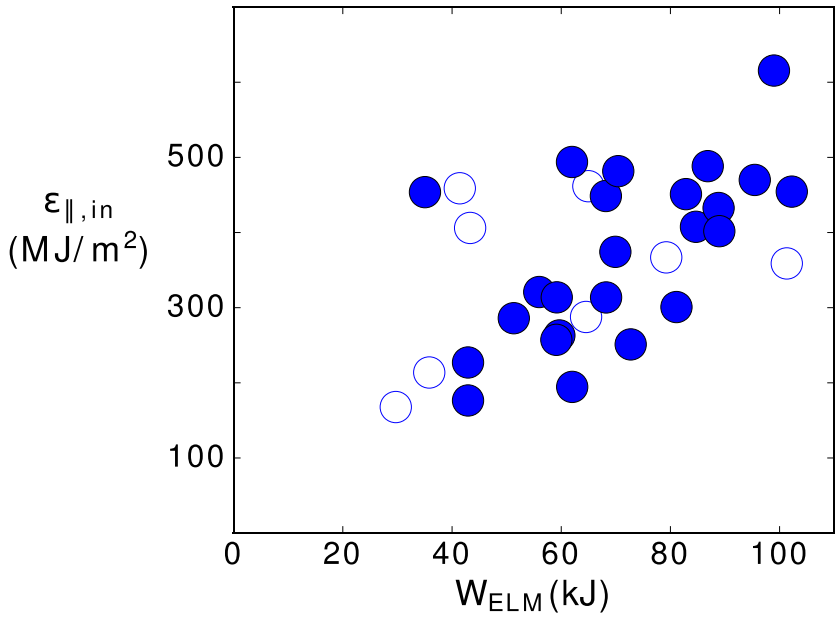

Figure 19 Dependence of peak parallel ELM energy density to the inner divertor on ELM size. Measurements from previous experiments are distinguished by non-filled markers to demonstrate the generality of the dataset.

density on the inner divertor and plasma loss energy during ELMs based on fast stored energy changes W_{ELM} for each of the inspected time intervals is shown in figure 19. While there is strong scatter in the data, the minimal observed ELM energy density increases with W_{ELM}. Notably, relatively high $\varepsilon_{\parallel}$ values can be reached at small ELM sizes: A 40 kJ ELM can generate a peak in parallel ELM energy density of up to $\varepsilon_{\parallel}$ ~0.45 $\frac{MJ}{m^2}$, which is the lower limit of the $\varepsilon_{\parallel}$ range for ELMs in the 100 kJ range. In the experiment described in this thesis, the ELM energy density is linearly proportional to the total energy deposited in the divertor. For ELMs with small W_{ELM} with large $\varepsilon_{\parallel}$ (as in the 40 kJ – 0.45 $\frac{MJ}{m^2}$ case) a large fraction of the ELM energy arrives in the divertor, implying that the radiative fraction is small. An example of different W_{ELM} but same $\varepsilon_{\parallel}$ is shown in figure 15: The mid-collisionality discharge (red) has smililar peak heat flux profiles as the high collisionality discharge (e,f). But the ELM size (not plotted here) differs by 30 kJ, due to a much higher ELM radiation energy (d). The accuracy of the Eich model prediction is slighly worse for the low radiation case ($\varepsilon_{Model}/\varepsilon_{\parallel}$ (black) = 1.7 vs $\varepsilon_{Model}/\varepsilon_{\parallel}$(red) = 1.2). A quantitative understanding of ELM radiation has not been established yet due to the difficulity of accurate measurements (very non-axisymmetric deposition) and the need for further progress in understanding the physics of neutrals in tokamaks. While radiation certainly contributes to the scatter observed about the Eich model, the weak proportionality in figure 19 implies coherence between models based on pedestal data (e.g. W_{ELM}) and divertor data (e.g. $\varepsilon_{\parallel}$), since an increase

of ELM energy is within the scatter consistent with a rise of ELM energy density and as such limiting the influence of radiation as reason behind the scatter of the Eich model. Additionally, Figure 18 shows that the divertor energies for large ELMs are very similar, yet the $\varepsilon_{Model}/\varepsilon_{\parallel}$ scatter does not decrease.
Although a linear dependence of the ELM energy density on the pedestal pressure is not seen, the spread in the dataset (0.5 x - 2.0 x $\varepsilon_{\parallel,Eich}$) remains consistent with the threefold spread observed in the comparison between the Eich model and the multi-machine database [90].

4.4. Overview of dependencies

While scaling laws serve the purpose of generally estimating ITER's ELM heat loads, an in depth study of potential drivers of ELM size facilitates deeper understanding of nonlinear ELM physics. Besides pedestal pressure and collisionality, the operation marginally above the LH threshold with large conductive ELMs will be inspected in this chapter.

4.4.1. Role of pressure and collisionality

Since plasma shape and the field ratio $\frac{B_T}{B_p}$ were kept approximately constant as part of the non-dimensional scan, the Eich model prediction implies a linear relation between $p_{e,ped}$ and $\varepsilon_{\parallel}$ (equation 2.43). Such dependence was not observed experimentally in the dataset as illustrated in figure 20 which shows the ELM energy density on the inner

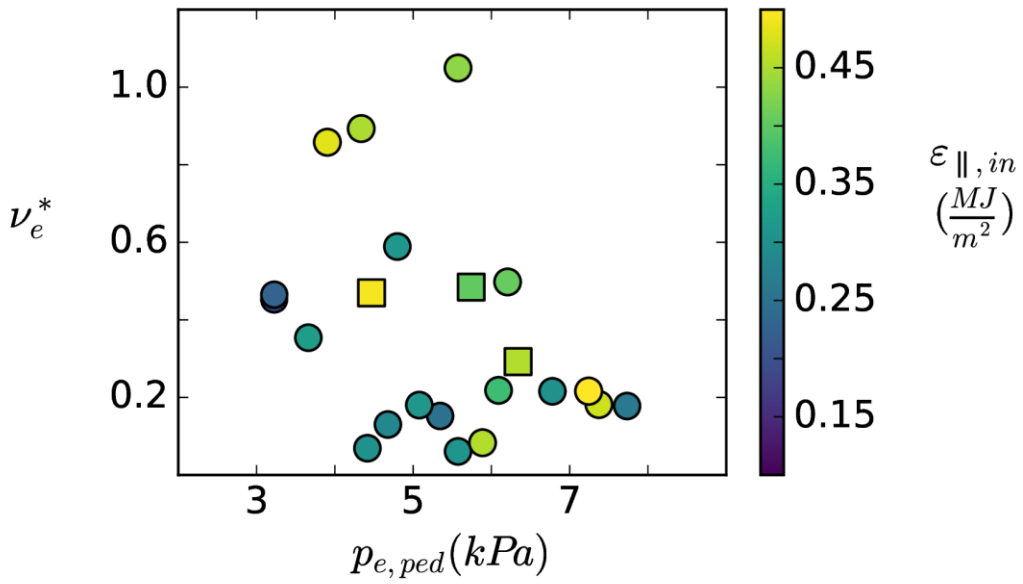

Figure 20 Dependence of peak parallel ELM energy density to the inner divertor on pedestal electron pressure and pedestal collisonality. The discharges with highlighted profiles in Figure 3 are distinguished by square makers (from left to right: low, high and medium B_T)

divertor in dependence of electron pedestal pressure and collisionality. In the region between 6 - 8 kPa with $\nu_e \approx 0.2$, there are high $\varepsilon_{\parallel}$ values of up to 0.6 $\frac{MJ}{m^2}$ next to low values in the 0.2 $\frac{MJ}{m^2}$ range. Large ELM energy densities in the 0.4 $\frac{MJ}{m^2}$ range are measured in the high collisionality region ($\upsilon_e^* \geq 0.8$) over a pressure range from 4-6 kPa (in these time windows the high collisionality resulted from a significant reduction of both NBI and ECH power).

4.4.2. Convective and conductive ELM sizes

By comparing profiles of temperature and density before and after the ELM, W_{ELM} can be split into a conductive and a convective part. Previous studies in DIII-D density scans [83] found that, while the energy fraction of an ELM transported convectively is approximately constant, the conductive energy loss associated with the pedestal temperature drop increases reciprocally with collisionality or proximity to the Greenwald density limit. Following these results, the largest values of W_{ELM} are expected at low collisionality as the pedestal temperature drop across an ELM reaches its largest magnitude.

The convective and conductive fractions of ELM transport were estimated using the following procedure (similar to the procedure used in [83]): Pedestal density and temperature in the pre-ELM phase were obtained from Thomson measurements using mappings from kinetic EFITs (corresponding to the 80-99 % inter-ELM phase), while the pedestal values for the post ELM phase were calculated based on standard EFITs as described below. This is necessary due to large uncertainties in post ELM kinetic equilibrium reconstructions (0-20 % inter-ELM phase): the MSE diagnostic incorrectly attributes ELM-driven filament currents in the SOL to confined plasma currents [36] and the data scatter in the Thomson measurements is high due to separatrix movement and convective transport. In detail, linear fits were applied to Thomson temperature and density measurements near the pedestal top for the first and last 10-20 % time interval of the respective inter ELM phases. The goal of these fits was to project the time-varying measurements of temperature and density to values at the onset of the ELM and at the start of recovery from the ELM. While the ELM cycle is a complex nonlinear process, linear fits in time as originally applied in [83] agree reasonably well with the Thomson measurements. The percent change of pre- to post-ELM value was then subtracted from the pedestal density and temperature values of the pre-ELM kinetic profiles. The conductive and convective energies are estimated as follows

$$W_{cond} = \frac{3}{2} \cdot V_{ELM} \cdot n_{e,av} \cdot (T_{e,pre} - T_{e,post}) \tag{4.1}$$

$$W_{conv} = 3 \cdot V_{ELM} \cdot T_{e,av} \cdot (n_{e,pre} - n_{e,post}) \tag{4.2}$$

where V_{ELM} is the plasma volume affected by the ELMs, the T_e and n_e refer to the values of the electron profiles taken at the- pedestal top before (pre) and after (post) an ELM. $T_{e,av}$ and $n_{e,av}$ refer to average values, i.e. $(T_{e,pre}+T_{e,post})/2$. As the ion parallel transport time is much slower than for electrons, the ion conductive losses can be neglected, and the ion convective losses are assumed to balance electron convective losses, maintaining ambipolar transport (hence the factor 3 in equation 4.2) [83]. V_{ELM} is calculated by comparing Thomson temperature and density profiles before and after the ELM and finding the maximum penetration depth of the ELM in ψ_N - space. From the ψ_N -V grid in the pre-ELM kinetic EFIT the affected volume V_{ELM} is obtained. In most cases the profile comparison indicates a maximum ELM penetration depth between ψ_N =0.5 and ψ_N =0.6, corresponding to an affected volume of approximately 10 m^3. In some cases, notably for input powers close to the L-H power threshold, a penetration up to a minimal ψ_N =0.3 is found.

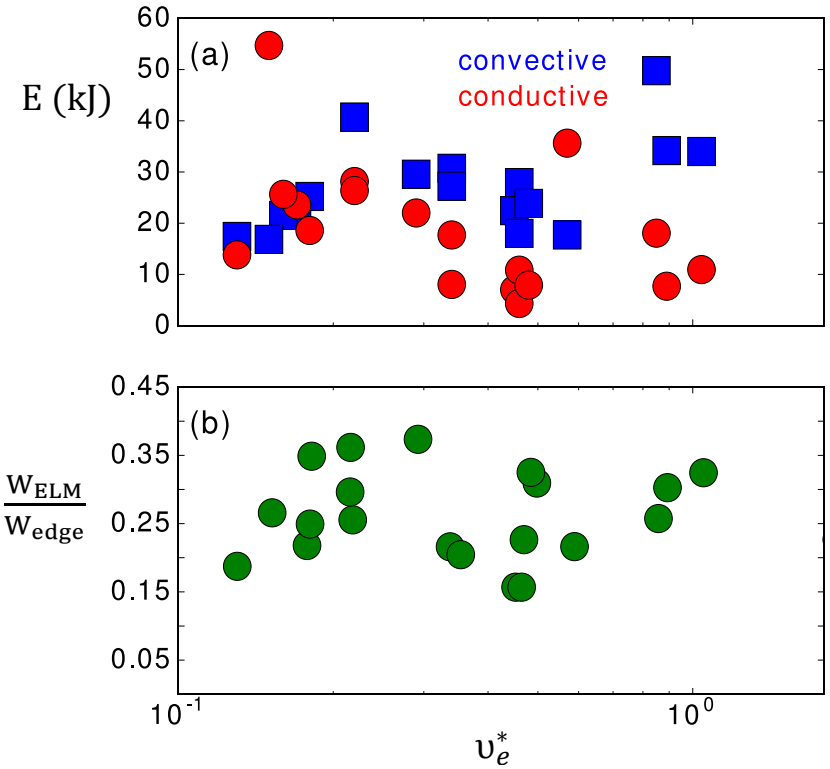

Figure 21 a) Calculated conductive and convective losses of the ELM vs. collisionality $\boldsymbol{\nu_e^*}$ b) ratio of measured ELM loss energy $\mathbf{W_{ELM}}$ to pedestal energy $\mathbf{W_{ped}}$ vs. collisonality $\boldsymbol{\nu_e^*}$

The results are shown in figure 21: there is strong scatter, but contrary to the results of previous ELM studies [83] the conductive energy loss (red) does not show a clear trend to increase at lower collisionality; moreover, while the convective loss (blue) doesn't show a clear correlation with collisionality, neither, high energies are obtained in the large collisionality segment around $\upsilon_e^* \geq 0.8$ (a).It should be noted though, that when comparing the ELM energy obtained by adding the convective and conductive energy

fractions to the ELM energy loss measured by magnetics, W_{ELM}, the ELM energy inferred from the kinetic profiles tends to underestimate the measured ELM energy in the higher collisionality range. This could be associated with the pure plasma assumption: The high collisionality cases are in general closer to the LH-threshold where, as will be explained in the following section, the ELM induced density reductions are stronger for impurities than for electrons. As most plasmas in the experiment were operated at power input close to the LH power threshold, biasing the dataset towards large ELM sizes at high density (and high collisionality), the expected inverse proportionality between collisionality and fast MHD energy losses was not seen. The ELM size in the previous DIII-D study stayed below a relative level W_{ELM}/W_{ped} of 20 % [83], whereas here values up to 35 % are included. For this experiment the ratio of measured ELM energy loss W_{ELM} and pedestal energy as defined in equation 2.42 does not depend on collisionality (Figure 21b).
Connecting back to Eich's model, the model underestimates the $\varepsilon_{\parallel}$ for ELMs with large convective transport near the LH threshold, as will be explained in the following segment.

4.4.3. L-H threshold proximity

As shown in the ELM size overview of Table 4, the largest relative ELM losses (grey background) are obtained for relatively small injected power at low ELM frequencies. The dataset indicates, that a change in ELM frequency alone does not necessarily imply a change in relative ELM size and that the heating power plays a strong role in determining relative ELM size. For instance, a doubling of the ELM frequency at constant power on 169425 (from 22 Hz to 45 Hz, caused by a density change) only leads to a marginal change in ELM size. In discharge 169433, where the relative ELM size (W_{ELM}/W_{MHD}) almost doubles following the 50 % reduction of P_{NBI} from t=1.8 s to t=3.0 s, f_{ELM} decreases overproportionately from 25 Hz to 7 Hz, further indicating a stronger role of the input power than f_{ELM} as driver behind ELM size changes. Overall the dataset here suggests that the ratio of the heating power to the L-H threshold has a strong impact on the relative ELM size. The analysis illustrated in figure 22a shows that the largest ELM losses W_{ELM} relative to the total plasma energy of up to 14 % occur when the heating power gets closer to the L-H threshold (equation 2.30). Here, the heating power P_{heat} is the sum of ohmic and external heating by ECH and NBI subtracted by radiation. As soon as P_{heat} reaches 2.5 times the LH-threshold value, the relative plasma losses during ELMs stay below 10 %.
Not only ELM energies but also ELM energy densities increase closer to the L-H threshold, which can already be inferred from figure 20. In this dataset, equilibria close to the L-H threshold are found at higher collisionality due to the low temperature at small heating powers and are associated with large ELM energy densities. The amount of scatter in the Eich model correlates with the relative heating power. This scatter is shown in figure 22b, which is a plot of the ratio of experimental ELM energy density to the Eich model prediction on the inner divertor versus the relative heating power.

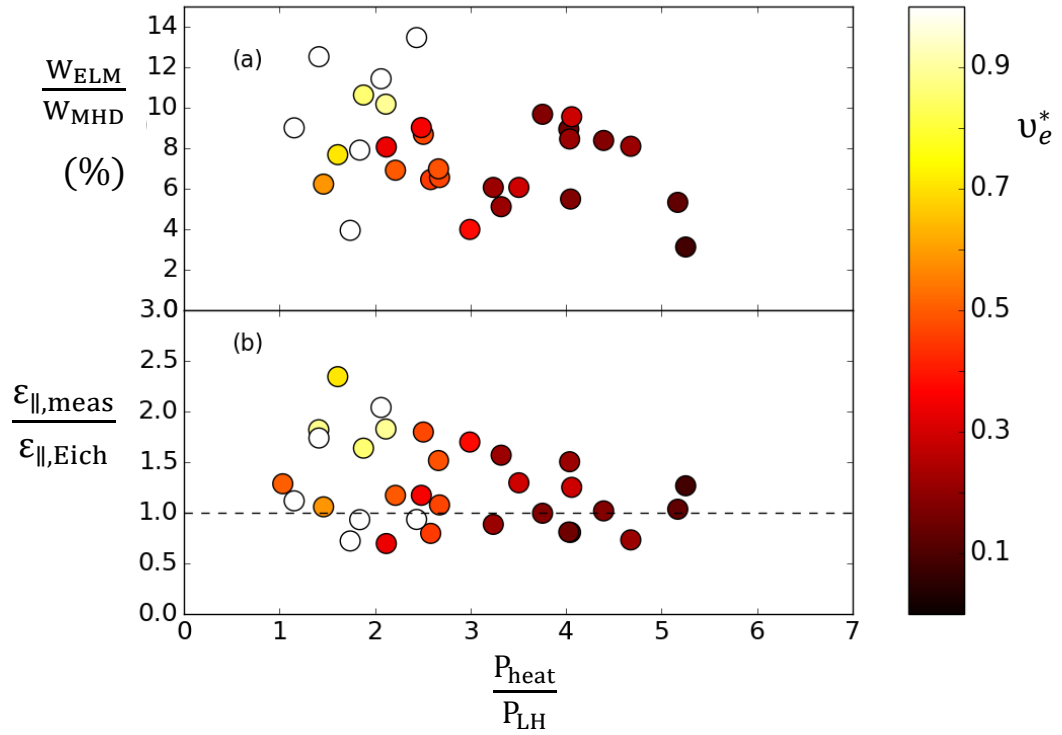

Figure 22 a) Relative ELM size vs relative heating power in dependence of collisionality, b) Measured relative ELM energy density to Eich model prediction vs proximity to LH-threshold

The inner divertor is chosen, as it generally had higher ELM energy densities during this experiment and more time windows can be included. Low densities ensure complete attachment and contrary to the outer divertor the full width is visible on the fast IR camera. Note that previous standard H-mode experiments (see section 4.1) are included in this figure and confirm the trend found in the more recent experiments. The $\varepsilon_{\parallel}$ range relative to the Eich model prediction decreases from 0.5-2.5 for discharges marginally above the threshold to 0.8-1.2 for strongly heated plasmas. To conclude, the Eich model performs generally better in well heated plasmas.

The physics behind the ELM size increase close to the LH threshold will be inspected in the following segment. A typical case demonstrating changes in the ELM dynamics when the input power approaches the LH-threshold is shown in figure 23. Following a drop of P_{NBI} from 4.0 to 1.4 MW, the net heating power of the discharge subtracted by radiative losses equals approximately the LH-threshold power (a). The ELM frequency initially decreases from 23 to 16 Hz (for 200ms, yellow window), and subsequently drops to f_{ELM}~3 Hz. While density profiles of electrons (e) and the Carbon impurities (f) are not affected in the intermediate phase, they start to increase in the low frequency phase. The confinement improvement is expressed by the H_{98} factor increase from H_{98}~1.5 to 1.7. These generally high confinement values could be achieved due to running the experiment closely after a boronization on DIII-D, improving wall conditions. Similarly, the beta values decrease marginally during the intermediate phase

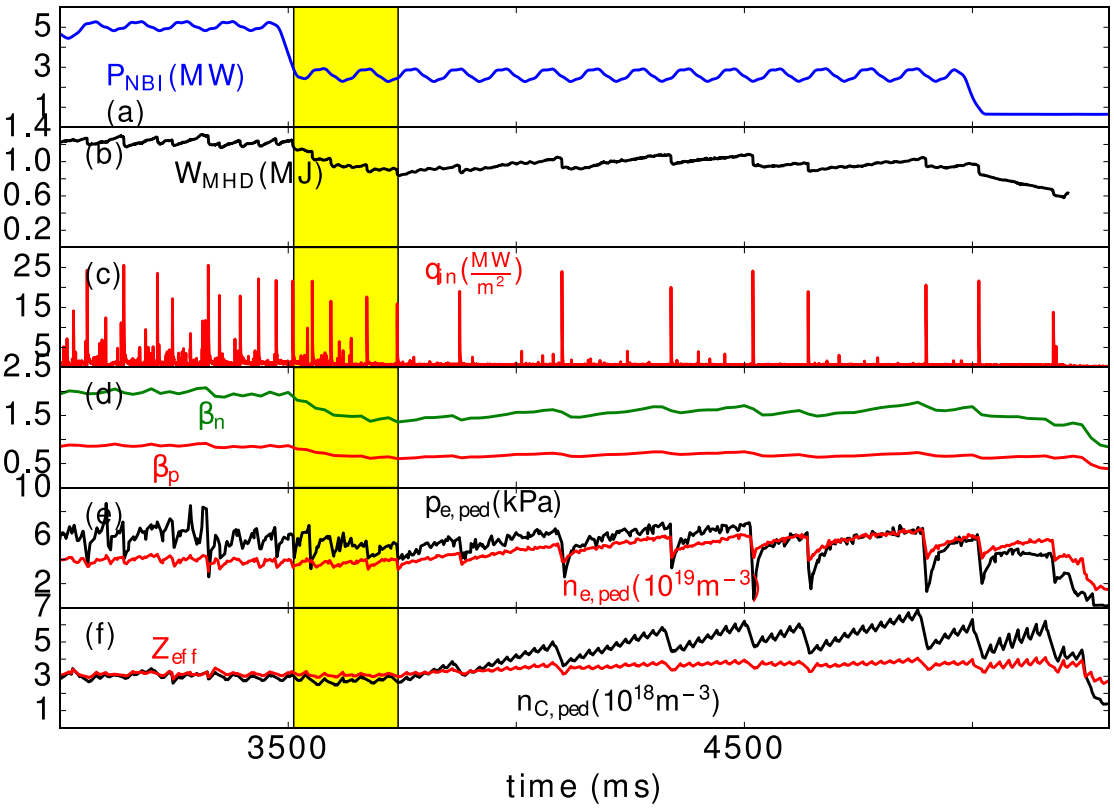

Figure 23 Discharge evolution of 169509 with a power ramp down closer to the LH-threshold: a) injected power with NBI (blue) b) stored MHD energy of the plasma, c) Peak heat flux on inner divertor, d) plasma betas β_n and β_p e) pedestal pressure (black) and pedestal electron density (red), f) effective charge (red) and Carbon impurity density at the pedestal top (black). The yellow window marks the intermediate phase, in which the ELM frequency is still high even though the power has been lowered. After the yellow window big ELMs occur even though the pressure is lower than in the first segment.

and then rise in the low frequency phase. The pedestal width increases during the beta rise phase. By comparing the total plasma energy W_{MHD} (b), the pedestal pressure (e), and the peak heat flux q_{peak} on the inner divertor (c), it becomes evident that the relative ELM size is largest in the third, low frequency phase (notice that both plasma energy and pedestal pressure are lower than in the first segment, but q_{peak} and W_{ELM} are similar). It is interesting to investigate the characteristics of these ELMs in comparison to ELMs in time intervals characterized by larger input power and larger ELM frequency.

A comparison of electron and ion profiles before and after the ELM (figure 24) shows that the largest difference comes with the electron and carbon impurity density profiles. First, note that the post ELM impurity density profiles look similar. In contrast, the pre-ELM profile is about 50 % higher at the edge when closer to the LH threshold. Similarly, the edge electron density decrease is stronger. These combined effects result in a relatively stronger loss of bootstrap current during the near LH threshold ELM, as its j_{bs} is largely determined by the pedestal density gradient in these discharges [51]. Linear stability analysis was performed for pre-ELM profiles taken before and after the

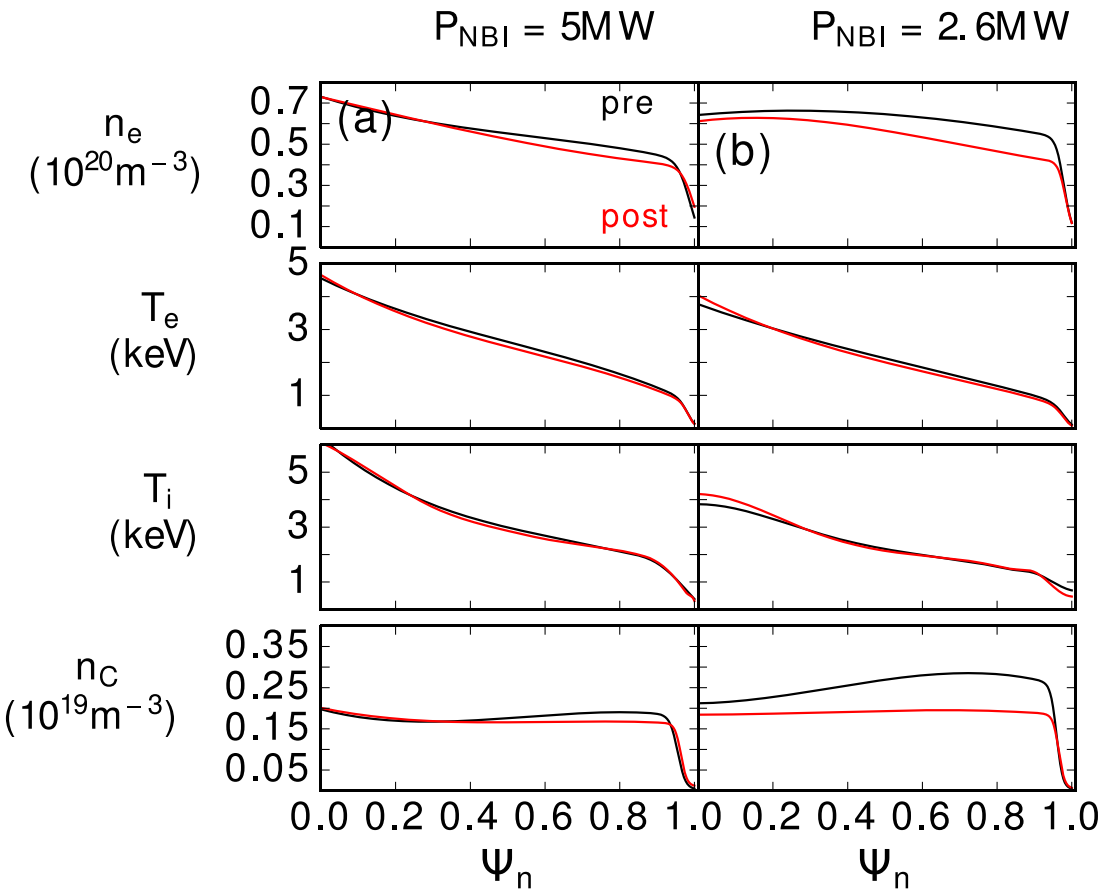

Figure 24 Comparison of pre (black) and post (red) ELM kinetic profiles for the equilibrium further away (P_{NBI}=5 MW, P_{heat}/P_{LH}=2.2) (a) and closer to the LH boundary (P_{NBI}=2.6 MW, P_{heat}/P_{LH}=1.2) (b) and. The traces shown are pedestal electron density and temperature, as well as ion impurity temperature and impurity density.

NBI power reduction (figure 25). The results are represented with the peeling-ballooning stability map in which the x-axis represents α, the normalized pressure gradient and the y-axis denotes the relative edge current density j_{norm} (as introduced in figure 7). The computation finds that, with reduced input power the changes in pedestal stability are minimal: the experimental points sit in similar locations of the stability map, the stability boundary itself changes marginally, and the linear growth rate spectra for both equilibria are similar, with n=16 being the most unstable mode number. In the combined framework of the peeling ballooning model [49] and ELM loss power as a constant share of SOL power (described in equation 2.31), the ELM behavior in the intermediate period (yellow) can be understood as a consequence of the NBI power reduction: The heating power loss leads to a slower pedestal buildup towards the same pedestal critical conditions, resulting in a lower ELM frequency. As the ELM loss power is reduced due to the smaller SOL power, the ELM energy loss remains approximately constant in the intermediate phase. However, the observation of large ELM sizes despite lower heating and reduced stored energy in the third section of the discharge is more difficult to interpret. The question is why does the ELM frequency

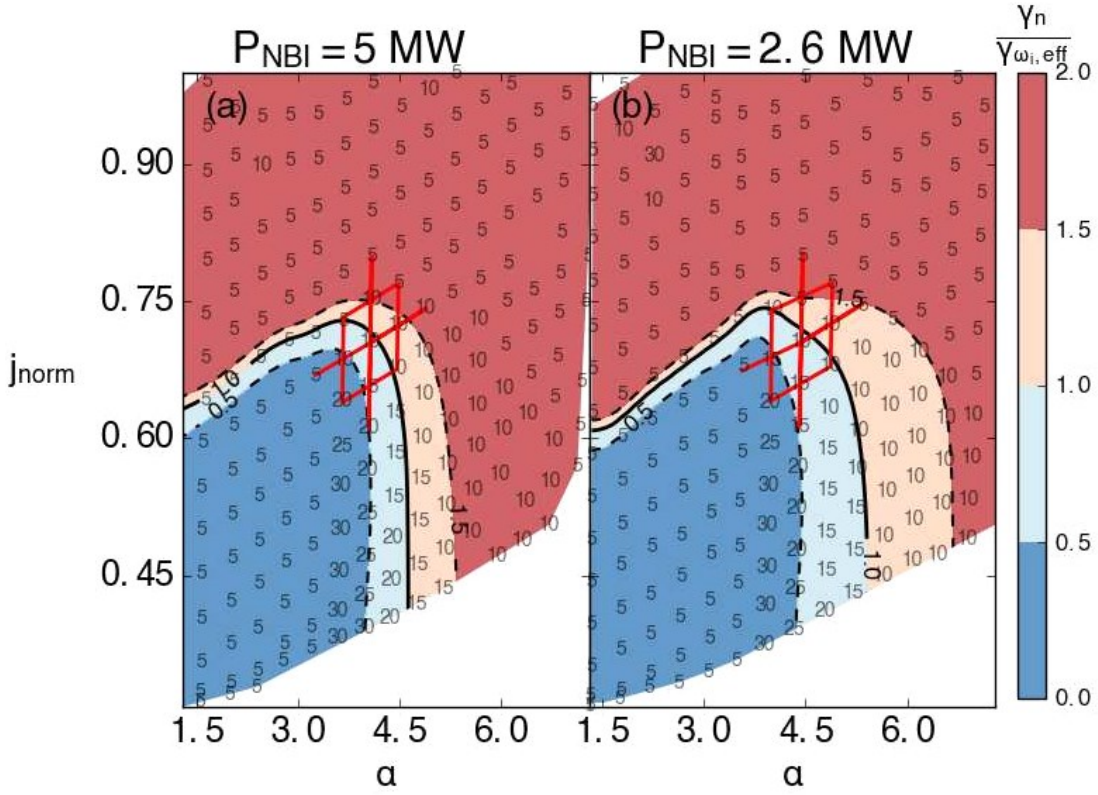

Figure 25 Comparison of linear stability analysis results before the ELM crashes for discharge 169509: an equilibrium further away from the LH power threshold at 3.0 s (a) contrasted with a scenario close to LH threshold at 4.2 s (b). The numbers in the plot indicate the most unstable linear mode for each equilibrium, with normalized growth rates $r = \frac{\gamma_n}{\gamma_{\omega i,eff}}$ (to its effective stabilization growth rate) divided in four groups: minimal (r<0.5, dark blue), marginal (0.5<r<1, light blue), unstable (1< r <1.5, yellow), very unstable (r>1.5, red).

for heating powers marginally above the LH threshold drop overproportionately compared to the power reduction? While the underlying dataset does not provide a systematic scan to answer this question, it allows to draw the following conclusions based on singular discharges including the one analyzed in this section: As the position in the peeling ballooning model diagram is similar, the critical pedestal pressure gradient and bootstrap current do not change after reducing the heating power. This is confirmed when comparing the bootstrap current size and pressure gradient in the kinetic EFITs of the 80-99 % ELM phase. However, there is a stronger contribution of the density gradient towards the pressure gradient (as can be seen in the profiles in figure 24, temperatures drop due to the heating power decrease). Additionally, as the buildup towards the critical gradient takes more time, impurities accumulate in the plasma. In the case of 169509 the collisionality almost doubles and the effective ion charge increases from 2.1 to 2.7.

Hence, it can be speculated that the ELM frequency drops overproportionately near the LH-threshold because the remaining edge current after the ELM crash is comparatively smaller in near LH scenarios and critical gradients and current densities need to be built

up through comparatively slower density increases. The profiles also indicate that the stored energy loss due to the heating reduction mainly affects the plasma core, so that the edge energy remains similar, and so does the absolute ELM size (while the relative ELM size increases due to the overall reduced stored energy). The ELMs the near LH-threshold are more convective, which is associated with lower radiation losses and could explain the large ELM energy density in some cases as for the one shown in figure 14 (black).

4.5. Comparison to linear stability analysis

The peeling-ballooning model for the ELM onset has proven to be successful in analyzing the linear stability of ELMy H-mode plasmas, as well as ELM controlled scenarios as QH-mode and RMP [124–126]. Based on the extensive validation, the model is presently used to extrapolate pedestal stability in future machines like ITER [127]. The model addresses the linear stability of the pedestal, providing information on the mode structure during the initial exponential growth, which precedes the nonlinear phase, associated with the pedestal collapse [128]. As pointed out in the introduction, the amplitude of the ELM losses should be addressed by nonlinear MHD simulations [78], which require extremely demanding computation resources. Consequently, there have been efforts to link linear simulations to nonlinear quantities [129,130]. Here, the question is raised whether the results of the linear ELITE code can provide insight about a nonlinear quantity, such as the ELM size. For instance, a common conjecture, based on extensive set of ELITE simulations, associates low-n peeling-ballooning modes with larger ELM sizes, due to the broad radial eigenfunction [127].

In this work ELM energy densities are found to scale inversely with the calculated most unstable toroidal linear mode number as will be shown in the following. For this purpose, stability analysis with the ELITE code was performed on all 27 kinetic equilibria of the dataset, to determine whether the position in the PB stability map, the toroidal mode number of the most stable modes, or growth rates have an influence on the experimentally observed ELM sizes. The latest version of the code was used including a bi-linear fit model for the calculation of the effective diamagnetic stabilization rate [131] to improve the accuracy of the results. To extend the range of the most unstable mode number n_{max} up to high values typical of the ballooning regime, the discharges from previous experiments described in section 4.1. were included in the analysis. From this additional dataset, four discharges representing a shot-by-shot density scan were selected, which was obtained by means of gas puffing and variation of heating power (shape, field and current were held constant). For this dataset, a wide region in the type-I ELM region from low-n to high-n PB modes is covered with similar plasma conditions ($W_{MHD}, \beta_N, p_{e,ped}, \delta$). Figure 26 shows the ELITE results from three consecutive discharges from this density scan. The stability boundary in the standard PB map (see figure 8) is drawn as a contour line for each of the discharges. For an equilibrium on this boundary the mode growth rate γ_n equals the

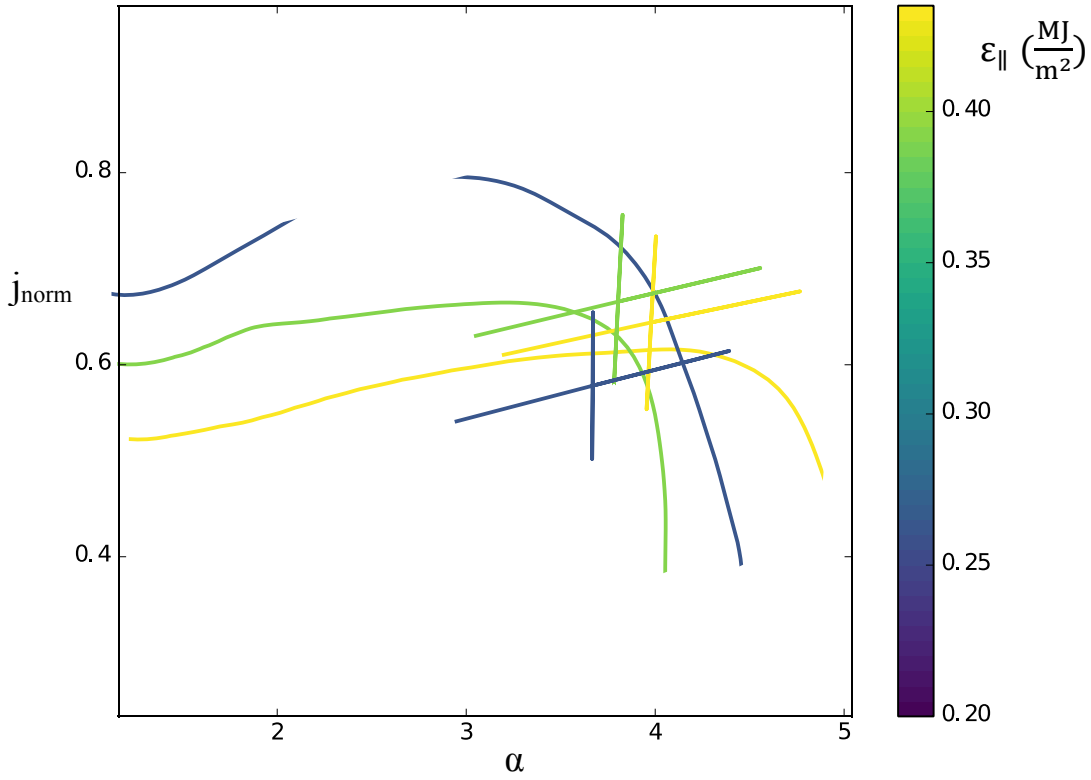

Figure 26 Linear stability of selected equilibria for discharge 153827 (yellow, n=14), 153828 (green, n=17) and 153830 (blue, n=35) with different collisionality and mode numbers. The contour lines show the stability threshold for the respective equilibrium in α-j space while the crosses denote the position of the operation point relative to the stability threshold. The peak parallel ELM energy density is indicated by the color of the lines and crosses, with the largest value corresponding to 0.43 MJ/m^2 and a most unstable mode number n=14.

effective stabilization rate $\gamma_{\omega i,eff}$. The color of each stability boundary corresponds to $\varepsilon_{\parallel}$ (from the inner or outer divertor, whichever is larger). The exact position of the equilibrium in j-α space is denoted by the cross in the respective color. An error bar of ±10 % is applied to account for the uncertainties in pedestal pressure and edge current density. From the position of the cross relative to the respective stability boundary one can distinguish the three discharges as low-n (yellow), intermediate-n (green), and high-n (purple) peeling-ballooning unstable.

As summarized in Table 5, the lowest $\varepsilon_{\parallel}$ =0.26 MJ/m^2 is measured during the most ballooning-unstable (n=35) plasma, and the highest $\varepsilon_{\parallel}$ =0.43 MJ/m^2 is measured during the most peeling-unstable (n=14) plasma. The relative growth rates of the most unstable mode $\frac{\gamma_n}{\gamma_{\omega i,eff}}$ are similar for these equilibria. There are three trends for the density scan experiment shown in this table:

- While the normalized growth rate determines how unstable a reconstructed equilibrium is, it does not correlate with ELM energy density. Typical type I ELMs are in the range of 0.8-1.5 around the onset of the instability.

- $\varepsilon_{\parallel}$ increases with lower n_{max}. This could either be due to the deeper penetration of the lower n modes into the plasma in the linear phase or due to the stronger role of the edge current. Analysis of numerous discharges did not show a correlation between edge current (relative and absolute size) and $\varepsilon_{\parallel}$, while the inverse scaling of $\varepsilon_{\parallel}$ and n_{max} held for all inspected discharges as explained below.

The prediction of Eich's model is less accurate at lower n_{max}. The physics causing the change in linear mode number structure (i.e. change of collisionality and effects of P_{LH} proximity) is not captured in the model. Further discharge analysis will show that there is no general dependence of the Eich scatter on mode numbers .

Most unstable n calculated	**ELM energy density experimental**	$\frac{\gamma_n}{\gamma_{\omega i,eff}}$ **calculated**	$\frac{\varepsilon_{exp}}{\varepsilon_{Eich}}$ **experimental**
14	0.43	1.5	1.7
15	0.39	1.9	1.6
17	0.38	1.2	1.6
24	0.30	1.4	1.3
35	0.26	1.4	1.1

Table 5 Linear stability analysis results of density scan experiment

Figure 27a shows peak ELM energy densities from the experiment of this thesis (including additional discharges described in section 3) as a function of the most unstable linear mode number n_{max}. As the ELITE calculation of mode numbers is sensitive to changes in the profiles of the equilibrium reconstruction, an error bar was added based on all mode numbers with growth rates larger than 90% of the n_{max} growth rate. Aside from the current profile, the exact location of the separatrix and the resulting electron temperature in this region are the largest sources of uncertainty. Because the comparison of the five ELMs over which the heat flux is averaged shows good reproducibility (figure 13), a 10 % error bar is assumed for the IR measurement. The results indicate a correlation with decreasing trend (as can be seen in the $1.1 \cdot n_{max}^{-0.38}$ fit to the data), with the largest ELM loads being reached for low-n peeling-ballooning modes. This confirms the findings of the density scan analysis (figure 26) and offers a better interpretation of the role of collisionality: for cases in which lower collisionality or a different edge density gradient lead to a lower n_{max}, lower ν_e^* will come with larger ELM energy densities and ELM sizes. But these large ELM energy densities can also be reached at high collisionality if n_{max} is lowered by another quantity, e.g. a large density gradient at the edge facilitating a strong bootstrap current. Regarding comparisons to other tokamaks, it is highly desirable to find a normalization quantity

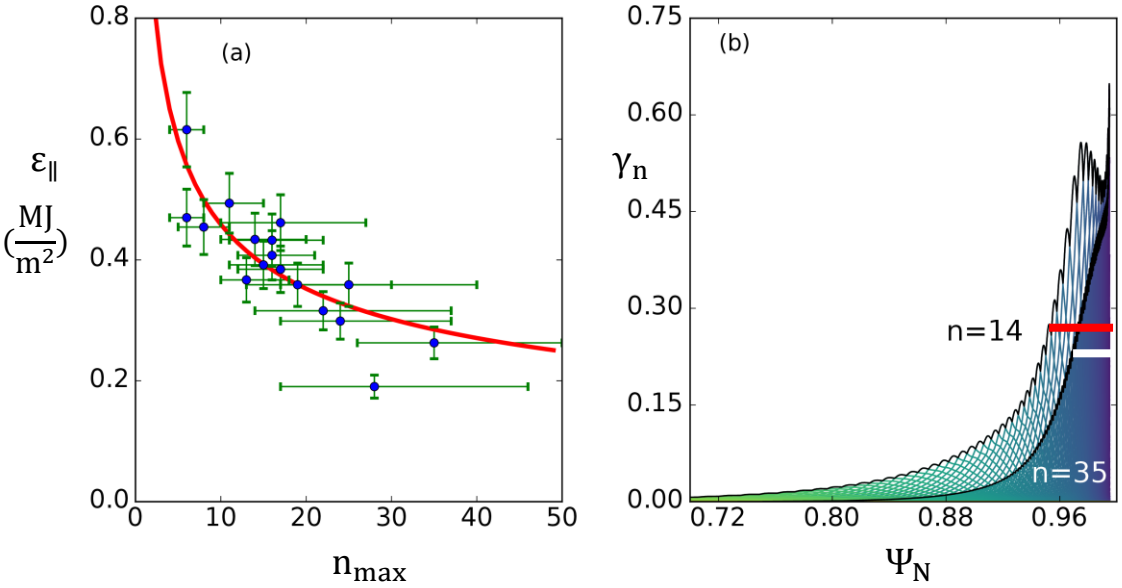

Figure 27 a) $\varepsilon_{\parallel}$ vs. most unstable mode number $n_{max}$for a selection of 17 equilibria. The error bar in the abscissa direction stretches over mode numbers with growth rates above 90 % of the n_{max} growth rate. A $1.1 \cdot {n_{max}}^{-0.38}$ fit (red) is included for reference b) Radial Eigenfunction of most unstable modes with width at half max penetration curves: (a) n=14 for low collisionality discharge 153827 (red), (b) n=35 for high collisionality discharge 153830 (white)

for $\varepsilon_{\parallel}$; at present a reasonable non-dimensional normalization for a $\varepsilon_{\parallel} = f(X) \cdot {n_{max}}^{-c}$ relation (with c a constant and f(X) a function of plasma parameter) has not been found yet. Identifying the exact physics mechanism behind the ELM energy density increase at lower mode numbers is beyond the scope of this work. As previously stated, a possible explanation is that lower-n-PB modes penetrate deeper into the plasma increasing the ELM size in the divertor. Radial eigenfunctions of the n_{max}=14 and n_{max}=35 equilibria are shown in figure 27b. One can see that in the n_{max}=14 case, there is a considerable peeling tail and the penetration reaches to about $\psi_N = 0.6$, while the high-n_{max} case only penetrates to $\psi_N = 0.8$. As the stability calculation is linear the amplitude is arbitrary. However, the width at half maximum can be used as indicator for the mode penetration. For the lower n mode number case (red horizontal line) the penetration is almost double that for the n=35 case (white horizontal line) and the mode mesh considerably coarser.

The scatter in the experimental data relative to the Eich model prediction can now be interpreted as a consequence of only including the pedestal height of all quantities considered in linear stability analysis. The prediction accuracy of the Eich model will decrease as soon as additional actuators (as triangularity, beta, collisionality …) cause a change in mode numbers without altering the $p_{e,ped}$. These "hidden variables" are responsible for the scatter in the Eich model, with the L-H threshold proximity being important for the largest outliers in this study.

Experimental signatures of this trend (thermal profiles, rotation) could unfortunately not be produced, as the fast CER measurements of ELMs during the experiment were

inconclusive due to an insufficient signal-to-noise ratio in the 0.25 ms integration period. From Thomson measurements a weak correlation between the most unstable mode number and the penetration depth of the electron temperature perturbation is seen; that is, deeper penetration of the temperature perturbation was typically associated with lower most unstable mode numbers. Some ELMs, having low n_{max} and short ELM penetration depth, deviate from this picture. However, these ELMs exhibit stronger decreases in electron temperatures in the ELM affected space.

For further investigation of edge-localized-modes, an important aspect of the nonlinear phase, the flow of currents, will be analyzed in the next chapter.

5. ELM currents

While the potentially important role of currents in the nonlinear ELM phase has been pointed out numerous times in literature [93,117,132], few quantitative or in-depth analyses were carried out. The purpose of studying ELM currents is improving the understanding of the nonlinear ELM phase in order to reliably control the instability on the long-term horizon.
In the following, current measurements on DIII-D are presented and interpreted with a new ELM current model (ECM).

5.1. Data selection

As shown in figure 14 of the heat load chapter a perpetual observation made during the ELM scaling studies consists of the flow of currents into the divertor tiles shortly after the ELM onset. Since the present DIII-D tile current array (TCA) is not as wide and sensitive to smaller currents as its predecessor, new experiments would likely not provide additional insights. Hence, a broad and intense study of 9000 logged DIII-D discharges was conducted to select a suited dataset for ELM current investigations.

5.1.1. Experimental scenario

Based among others on ELM frequency, TCA data availability and discharge shape a

Series	**Analyzed discharge range**	**TCA**	**B_T [T]**	**I_P [MA]**	**f_{ELM} [Hz]**
ELM and SOL characterization	118210 118250-118255 119432-119450	Old	+2.1 +1.7 -1.7	1.0	20 - 70
Particle exhaust in non-symmetric DN	119143-119150	Old	+1.9	1.0	20 - 40
ELM shape dependence	121553-121571	Old	-1.8	1.5	38 - 80
Long Pulse ITER baseline	147140	New	-1.6	1.3	5 - 20
ELM heat load	169509	New	-2.1	1.5	10 - 25

Table 6 Overview of discharges analyzed or referred to in this thesis. All shapes are LSN, negative B_T (forward B_T) indicates ion $B \times \nabla B$ pointing to the lower divertor.

selection of multiple experiments was made with two different divertor constructions, both realized with all-graphite tiles. In the following, the experimental scenarios and TCA configurations are described (an overview is given in table 6). With the exception of the particle exhaust experiment [133], all discharges listed in table 6 are in lower single null (LSN) shape. The majority is chosen from an ELM and SOL study [27], focusing among others on the effect of B × ∇B drift direction on ELMs.

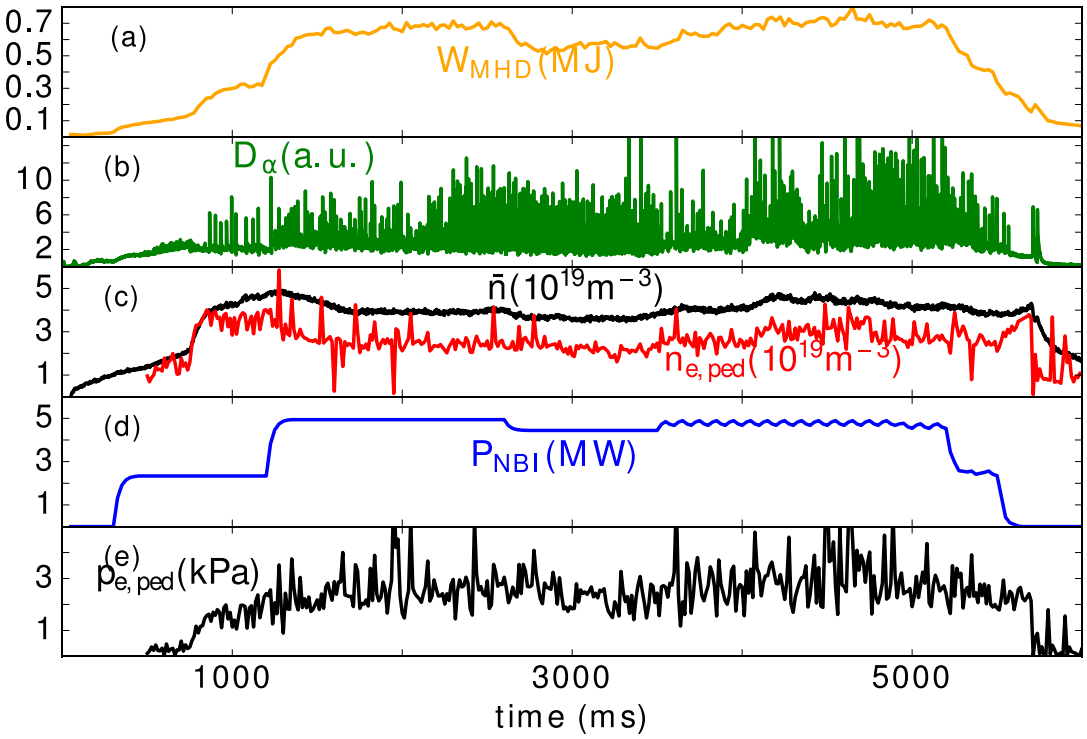

Figure 28 Discharge evolution of 119432: a) Plasma energy in MJ, b) ELM D-α filterscope, c) line-averaged (black) and pedestal density (red), d) NBI power in MW (blue), e) pedestal electron pressure in kPa.

The typical discharge evolution as illustrated in figure 28 will be described briefly. In this discharge the ion B × ∇B drift is pointed towards the lower divertor (forward B_T on DIII-D, see appendix A). The current flattop of $I_P = 1.0$ MA is reached at 1.5 s, and the toroidal field strength is 1.7 T. The plasma energy is 0.7 MJ (a), with an injected power of 5.0 MW (d). The neutral beams are programmed to fire in a specific way[7] in the second part of the discharge to improve spatial resolution of pedestal ion measurements by Charge Exchange Recombination (CER) causing a sinusoidal pattern in the power trace. The ELMs are detected by the D-α filterscope (b) with a frequency around 60 Hz. The pedestal electron pressure is approximately 3 kPa and stays fairly constant throughout the H-mode phase (starting around 0.8 s), as do the pedestal- and line-averaged density (c). This discharge and all others in this series are heated

[7] So called beam modulation: a pair of beams is programmed to fire alternating, so that the origin for the CER signal can clearly be determined.

considerably above the L-H threshold with P_{heat}/P_{LH}=3.0. The discharges with the ion B × ∇B drift away from the lower divertor are run at matching plasma conditions (same shape and Ip, heating and field strength). The second series of discharges is taken from an ELM shape study [134] set up with I_P = 1.5 MA in forward B_T =1.8 T and heated by 7.0 MW of neutral beam power. To compare divertor heat fluxes to tile currents, an ITER baseline scenario study [135] with ELM resolved IR camera data is included in the analysis. The experiment was conducted with the contemporary TCA at 1.25 MA and 1.6 T (ion B × ∇B downwards) with a heating power of 2.5 MW. The discharges are heated marginally above the LH threshold and exhibit low ELM frequencies of about 10 Hz. Additionally, discharges from the heat load experiment with forward B_T =2.15 T and I_P = 1.5 MA (chapter 4) are analyzed [136]. The particle exhaust experiment in DN shape for validation of the ELM current model developed in this chapter and set in reversed B_T=1.9 T. The type-I ELM sizes in all discharges considered for the ELM current analysis range between 15 and 110 kJ. Also, compound ELMs are included in this analysis with sizes up to 400 kJ (50 % of W_{MHD}).

5.1.2. Illustration of measurements

The time evolution of currents flowing into divertor tiles during a selected 200 ms time window in discharge 119432 (introduced in figure 28) is compiled in figure 29.

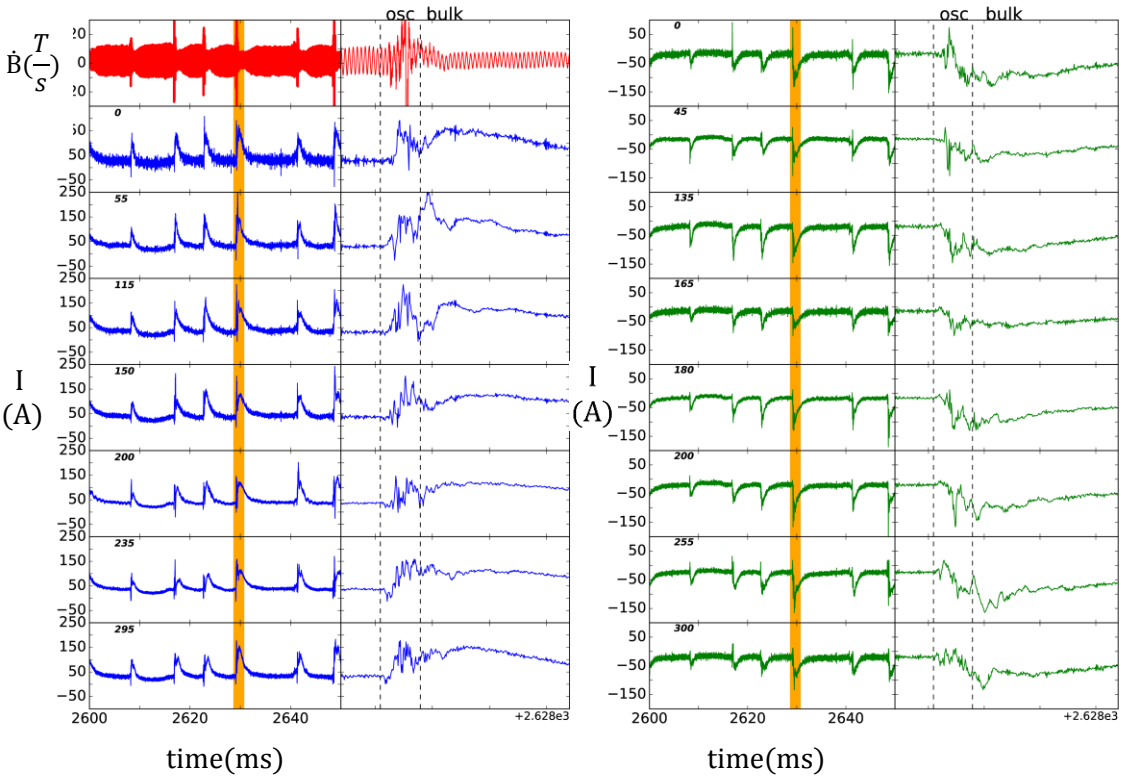

Figure 29 Evolution of tile currents in inner (ring 10, blue) and outer divertor (ring 14, green) during discharge 119432 between 2.6s and 2.65 s. The toroidal position of each TCA is indicated by the bold number on the top left. ELMs - registered by the fast midplane magnetic probe (red) - are discernible on all tile current monitors. The 1 ms zoom (orange) into a single ELM reveals oscillations the initial ELM phase, followed by the bulk/filamentary phase.

As an indicator for ELMs the 150º toroidal fast magnetic probe trace is depicted (red). The current measurements of sensors located in ring 10 near the inner strike point are colored in blue, the measurement of sensors near the outer strike point in ring 14 are shown in green. The strike point positions of this discharge (ISP near ring 10, OSP close to ring 14) are representative, as this shape is used as a well-developed LSN standard. The respective tile sensor position in machine coordinates is indicated on the top left of each panel (in accordance with the TCA layout shown in figure 10). A zoom into a singular ELM is provided by the 1 ms time window on the respective left of each side. There are three phases distinguishable in the zoom window, which are representative of all ELMs in this discharge:

- the inter-ELM current (prior to 1st dashed line, duration depends on ELM frequency): small currents below 50 A on all TCA, positive on inner, negative on outer
- the oscillatory phase (between dashed lines, 0.25 ms duration): peak absolutes of up to 150 A, sign changes
- the bulk phase (past 2nd dashed lines, about 1 ms duration): currents still large (e.g. 150 A on 10B200), but few sign changes or oscillations

During the featured discharge seven sensors in ring 10 and eight sensors in ring 14 were sampling data at 200 kHz. The current amplitude is 150-200 A near the inner and -100 A to -150 A near the outer strike point. Positive currents indicate a net loss of electrons on the tile, while negative currents indicate net gain of electrons on the tile. This would indicate a net flow of negative charge from the inner to the outer strike point. However, there are also spikes in the opposite direction for both rings as shown in the figure (up to -50 A near the inner, 50 A near the outer strike point respectively).
The significance and potential role of tile currents are reflected in their magnitude compared to the inter ELM phase currents as well as in their prominent temporal position between rise of magnetic activity in the plasma and the divertor heat flux peak, as will be shown in the following. For illustration, typical ELM evolutions on DIII-D over the time span of 1.4 ms are shown in figure 30. The particle exhaust and recycling from the walls are detected by D-α-radiation (656 nm) measurements focused on the outer divertor leg at a 135° toroidal position (a). These are large type-I ELM (energy loss ≈ 10 % of plasma energy) common for DIII-D plasmas operated marginally above the LH-threshold at very low ELM frequency. The magnetic probe data from a poloidal probe at 322 ° sampling at 200 kHz (b) covers growth and non-linear phase of the ELM. Regarding the sequence, after the initial growth of the ELM is registered in the magnetics, the ELM bursts at the outer midplane first [137]. On the way towards the divertor interaction of expelled energetic particles with the local plasma leads to an increase of D-α radiation. The peak in the divertor heat flux (d) marks the bulk energy arrival in the outer divertor. Between peak activity in magnetics and filterscope the divertor tile current peaks in the illustrated sensor (TCA 13B068). As figure 29, the

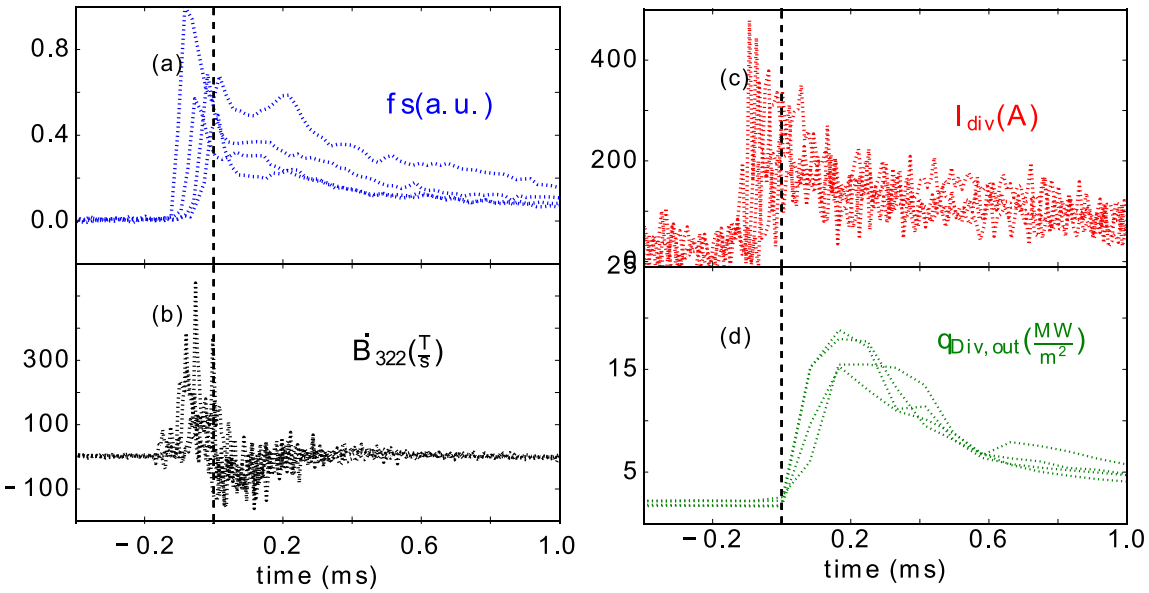

Figure 30 Current Precursor for type-I ELMs in divertor on discharge 169509, 1.2 ms time window: a) D-α-filterscope at 135 ° toroidal, view on outer divertor b) poloidal magnetic fluctuation measurement at 322 ° toroidal (200 kHz sampling rate) c) Divertor Current measured at 68 ° in row 13 (100 kHz sampling rate) , d) peak outer heat flux measured by IR camera at 60 ° (12 kHz sampling rate)

temporal shape of the tile current in the outer ring during the ELM consists of two elements (c):

- a large spike of 400 A at the time of the first increase in D-α-radiation (the oscillations are suppressed due to the use of an electronic 40 kHz filter)
- a constant current flow with up to 200 A, lasting for about 1.2 ms. This phase often comes in shape of a ‘bump’.

The current peak occurs before peak heat flux in the outer divertor measured with the 60° IR camera starts to increase (indicated by the dashed line). Note that toroidal TCA location and IR camera position coincide. As the IR camera sampling frequency of 12 kHz is much lower than the sampling frequency of the Dα-filterscope or the TCA sensor (here 100 kHz), it is necessary to carefully analyze respective construction of measurement time bases. While each data point of the TCA corresponds to the current measurement exactly at that time, the IR data point corresponds to the divertor temperature calculated from the integrated photon count in a 72 µs time window at the beginning of each 0.082 ms sampling interval. Using the THEODOR code [115] the heat flux is then reconstructed for the time step before, as the heat flux causes the temperature increase. This implies that at the current spike (coinciding with dashed line) there is no significant temperature increase in the divertor. Note that as a part of the outer divertor (not the OSP) is shadowed to the IR view an earlier temperature increase in this shadowed region would not be registered by the camera. The ELM presented in figure 30 is clearly showing, that large divertor currents are flowing before

the heat flux increases. This result has been reproduced on multiple contemporary discharges and raises the question where the tile currents flow in the tokamak and what their causal impact is.

5.2. The typical ELM current

For further analysis, it is important to compare current flows of multiple ELMs in spatial and temporal space, to find the current flow during a typical ELM, labelled the average ELM in consistency with previous work [138].

5.2.1. Temporal coherence

Under relevant stationary conditions (constant heating, similar pedestal pressure in corresponding inter-ELM phases) the shape of successive ELM divertor currents is invariable with the exception of an oscillatory phase at the onset. To obtain a temporal

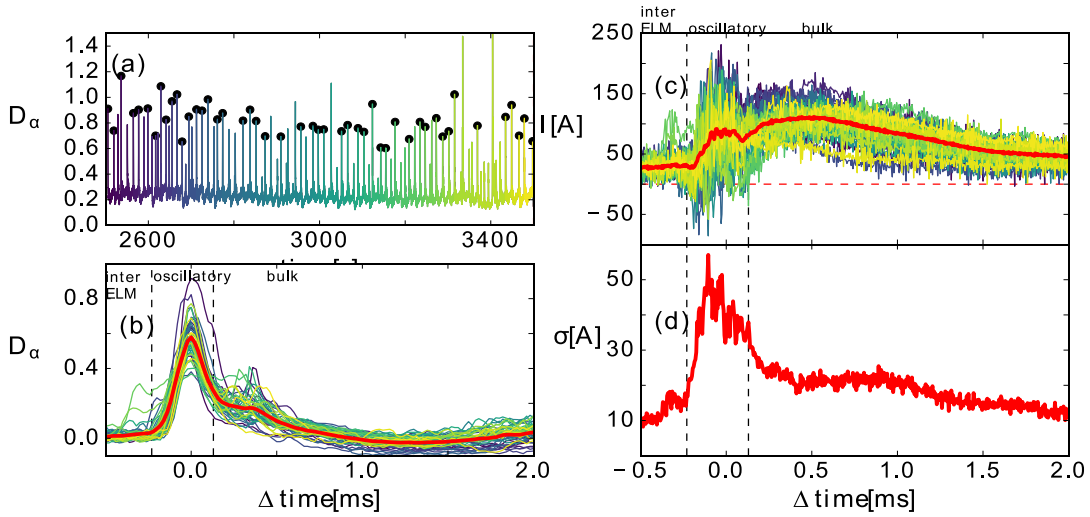

Figure 31 Temporal average of ELMs on 119432: a) Dα trace between 2.5 and 3.5 s b) Dα relative to its peak with the average in red c) tile current in TCM 10B000 relative to Dα peak with the red line marking the average d) standard deviation of the tile current

average of the divertor currents flowing through the same tile over multiple ELMs, conditional averaging is required. Figure 31 shows the D-α signal between 2.6 s and 3.4 s in discharge 119432, color-coded by time (a). The ELM frequency averages 65 Hz in this segment. As the D-α signal is non-saturated its peak during each ELM is suitable and reliable to be used as reference point for conditional averaging. The resulting average ELM for the D-α signal and the tile current measured at TCA sensor 10B000 can be seen in (b) and (c), respectively. The red line indicates the mean of the 48 ELMs. One can clearly see that there is broad correlation between successive ELMs regarding D-α and TCA signals, except for the time frame of 0.35 ms between the two vertical dashed lines. It is a region of strong oscillation, and the oscillations differ from

ELM to ELM in amplitude and number. This becomes evident when calculating the standard deviation of the current for each time (d). The peaks of the oscillation are higher on average than the peak during the bulk phase when the heat flux arrives at $\Delta t = 0.5$ ms, so it is mainly these oscillations that are seen in the overview plot in figure 28.

5.2.2. Spatial variations

Having determined the temporal average of the tile currents during an ELM, it is now interesting to compare the spatial variation of the current. An exact radial distribution pattern for the tile currents is difficult to infer, as the number of measurement points in the radial direction is limited by the number of tiles. Unfortunately, no Langmuir probe data on these discharges was available to analyze current flows within a tile. If there were current flowing into one side of the tile and flowing out on the other side, the TCA would measure the average. The drawing of the TCA (figure 10) illustrates that at a machine angle of 200° there are five tiles with current monitors. Radial profiles of current measurements for four tiles at this angle (no fast TCA measurement in ring 13 was available) are shown in figure 32 for discharges with same shape but different

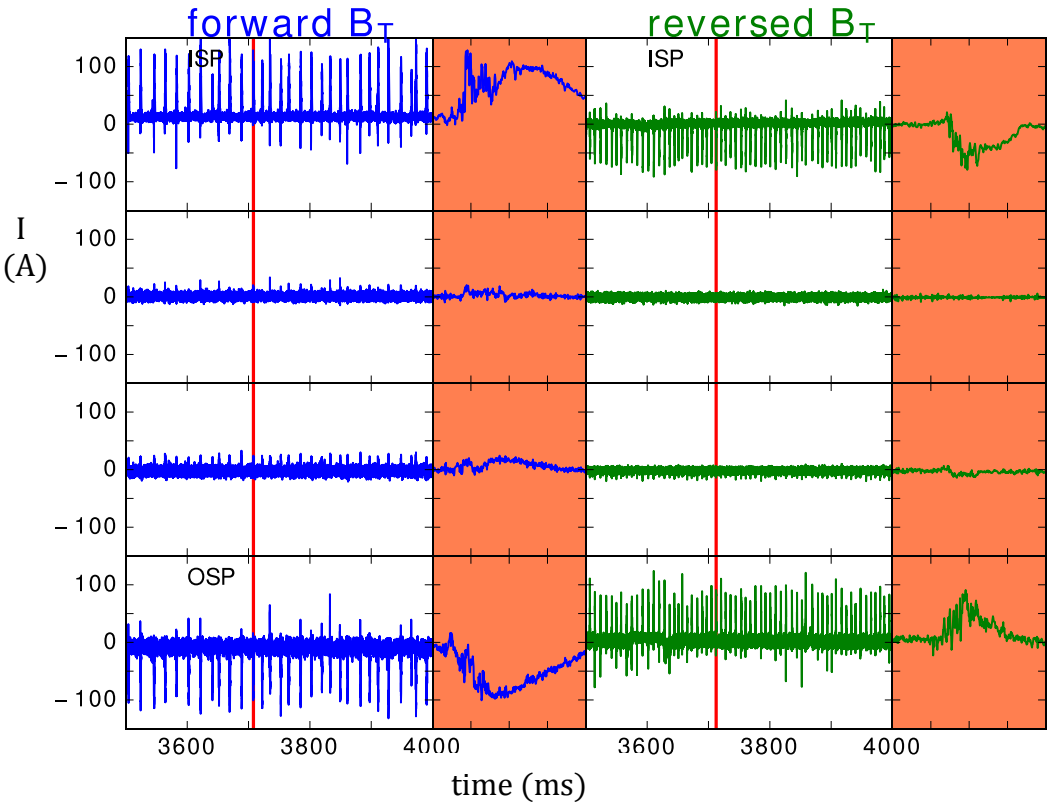

Figure 32 Comparison of TCA signals during forward Bt (blue, 119448) and reversed Bt (green 118252) at 200 °s in machine coordinate from inner 10 ring (a) to outer 14 (d) ring. The position of the outer strike point is shown in the respective first row. The used signals here are from the rings 10,11,12 and 14 (from top to bottom). The orange regions are a zoom into a single ELM from 3711.5 ms to 3713.5 ms to resolve the oscillations.

B × ∇B direction. The largest currents are measured near the strike points, currents of smaller size are measured in the private flux region. As mentioned before the spikes shown originate mostly from the oscillatory phase. Reversing the toroidal field direction (same I_P, so B × ∇B drift pointing upwards now) leads to a reversal of tile current direction. While in forward direction the TCA on the inner ring measure positive inter ELM currents and positive deflections during ELMs (119448), the deflections turn negative here in reversed B_T (118252), where the outer ring receives positive currents. As the zoom into a single ELM shows, the bump is clearly mirrored, whereas ratio of peaks between the oscillatory phase and the bump is smaller on the inner ring in reversed B_T. As seen from the radial current profiles, the majority of the ELM currents is flowing through the tile rings near the strike points. Hence, only these will be considered for the further toroidal analysis, including rotation and mode numbers. At first it will be shown that there is harmonic variation in the toroidal direction within the vicinity of inner and outer strike point. For this purpose, the ELM at 2712.5 ms of discharge 119432 is selected; its toroidally-resolved current measurements in ring 10 and 14 at various times are shown in figure 33.

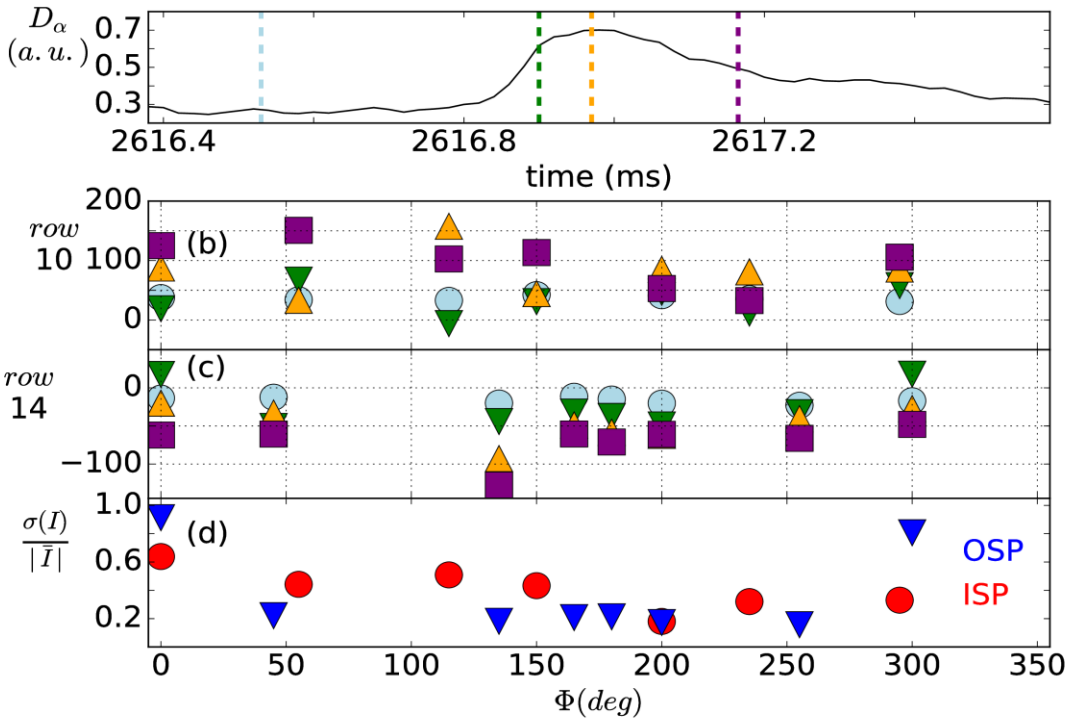

Figure 33 Toroidal current measurement of a single ELM in 119432: a) Dα signal with color-code to identify position and succession for b) tile current as monitored near the inner strike point and c) outer strike point d) ratio of standard deviation and absolute mean of tile currents near ISP and OSP during oscillatory phase between 2616.90 (green line) and 2616.98 (yellow line).

The dashed, colored lines in the D-α signal (a) are used to indicate these measurement times for the tile currents of row 10 near the ISP (b) and row 14 near the OSP (c). One sees that all tile currents are initially at similar values (light blue), then there is

considerable variation especially at the toroidal angle of 135º during the oscillatory phase near the OSP (yellow-green). 1 ms after the D-α peak (purple), the toroidal variation on the ISP has decreased, however, currents have still not returned to pre-ELM values. The standard deviation of TCA currents normalized to their respective means in the oscillatory phase (here between yellow and green line) emphasizes a strong n=1 deviation with most oscillation at machine angles of 0 and 300 ° (d). Theoretically – as only 10 of 72 tiles in row 14 are part of the TCA, and their measurements are averages over 2 spatial directions – it is conceivable that the current distribution during the pre-ELM phase could be strongly localized toroidally on only a small number of tiles. However, from studies of numerous discharges with different edge rotations and medium range type-I ELM frequencies undertaken within the framework of this thesis, there has not been a single occasion with an oscillation pattern fundamentally different to the one in figure 33, i.e. an ELM with no current spike in the oscillatory phase in any of the near strike point tile current sensors. With the limited toroidal coverage of the tiles, one would expect that some ELMs would not be accompanied by a toroidal spike if the currents were highly toroidally localized. As this is not the case, it must be concluded that the toroidal structure varies relatively slowly (i.e. low-n). Hence, the toroidal structure is sufficiently smooth that it can be accurately represented in terms of a low-n Fourier series.

5.2.3. Mode number and rotation

This section will show that mode numbers inferred from the TCA are within the expected range from peeling-ballooning theory [76] and experimental measurements with fluctuation diagnostics [93]. Based on the previous analysis, the toroidal Fourier decomposition $\vec{S}$ of the measured currents I_{TCA} can be found by solving the following matrix equation

$$V_{mod} \cdot \vec{S} = \overrightarrow{I_{TCA}} \tag{5.1}$$

Here, $\overrightarrow{I_{TCA}}$ represents a vector of the measured tile currents at different toroidal locations within a ring, $\vec{S}$ is the Fourier decomposition of the measured tile currents, and V_{mod} is the basis matrix of the low-n Fourier reconstruction corresponding to each of the TCA sensors. $\vec{S}$ and $\overrightarrow{I_{TCA}}$ are time-dependent as defined in appendix C. The total current in the n=0 component in a toroidal ring can simply be extrapolated using the sum of all individual TCA measurements I_i of that ring and the total number of tiles in the ring N_{tiles}

$$I_{n=0} = \frac{N_{tiles}}{N_{TCA}} \cdot \sum_{i=1}^{N_{TCA}} I_i \tag{5.2}$$

The total current in each phase can be obtained by multiplying the Fourier component with the number of tiles in the respective ring. An example for this analysis of ELM currents near the strike points on discharge 119432 is shown in figure 34.

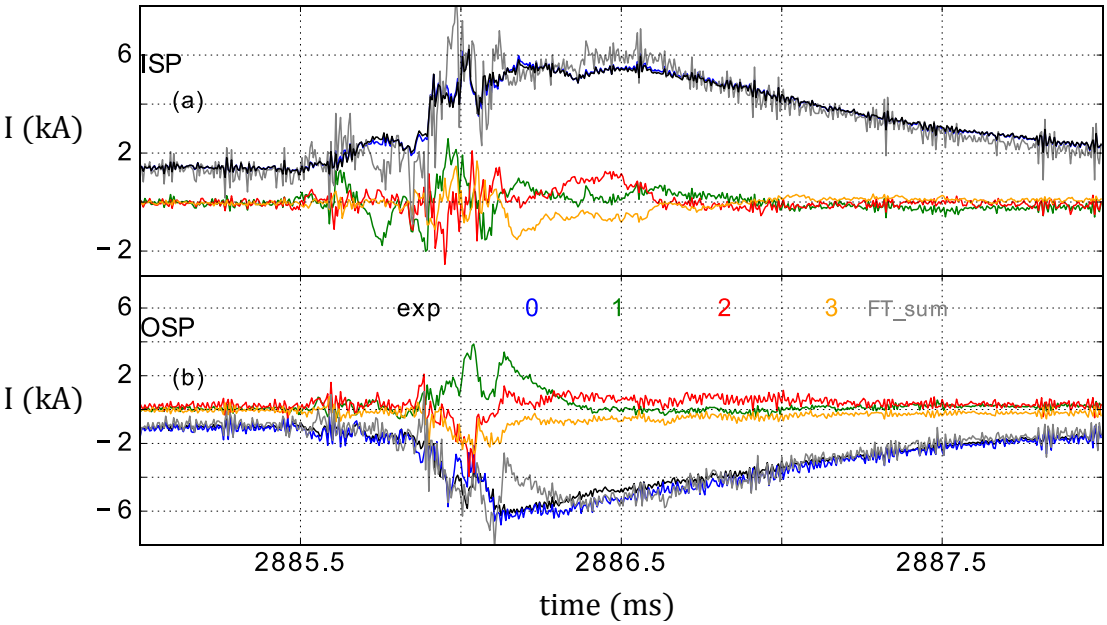

Figure 34 Mode decomposition of tile currents during type-I ELM: a) ISP Amplitude of n=0 to n=3 modes b) OSP Amplitude of n=0 to n=3 modes during a typical ELM. The sum of the currents in the decomposed modes (grey) is compared to the experimental measurement (black), the difference is due to missing higher harmonics in the decomposition and finite tile width effects (radial broadening of divertor current deposition during the ELM, currents in private flux region and outer SOL not captured by central strike point tile). Inner and outer divertor currents balance with a peak of about 6 kA.

As there are seven functional current sensors near the ISP (respectively eight near the OSP) in this discharge mode numbers up to n=3 were analyzed. The contribution of these mode numbers can be divided in two groups (a): The zeroth component is dominant in the post-oscillatory phase, whereas a mix of the higher mode numbers produces the oscillation in the onset phase of the ELM. This division is representative for all ELMs during this discharge on the inner ring. In the outer ring (lower part of the figure), the Fourier decomposition looks similar with the exception of the sign of the 0^{th} component contribution. The current in the n=1 and n=2 component reaches up to 4 kA at the OSP, the current in the n=3 phase up to 2 kA, indicating that typical helical components are only slightly below the ring current peak in the oscillatory phase. While the Fourier decomposition indicates good agreement with a mix of low n-modes (as can be seen by the comparison of black and grey trace, representing experimental current and sum of currents in the Fourier components), it needs to be stated that the possibility to resolve higher mode numbers is restricted by the number of available sensors. If there were high n asymmetries, the TCA would not be able to detect them. The comparison of total currents near inner and outer strike point in figure 34 demonstrates that they balance. The inter ELM current is 1.7 kA for this forward B_T discharge, the matching

reverse Bt discharge displays a current flow of 0.9 kA in the opposite direction (not shown here). The resulting ELM peak current values range between 5 and 8 kA (up to 20 kA have been measured during larger ELMs). This is consistent with previous TCA measurements [139] and magnetic measurements [140]. In agreement with the TCA measurements, a mix of low-n mode numbers is what is typically seen on the magnetics during ELMs in standard H-modes in mid-scale tokamaks [93]. Linear Stability analysis with the ELITE code [49] shows that the most unstable linear modes of these shots are mid-range peeling-ballooning modes around n=15-20. Experimental results of a mix low-n modes measured by the TCA in the nonlinear phase are however still in line with the peeling-ballooning model, as nonlinear ELM simulations indicate that the unstable linear modes can beat together and drive a low-n mode in the post-linear growth phase [76,77]. Hence, there is correlation between the nonlinear mode structure in the plasma and in the tile current array.

5.3. Coherence of tile currents and ELM properties

Having defined the currents during a typical ELM and shown the principal mode number correlation with nonlinear peeling ballooning simulations, it is now interesting to compare current to ELM properties.

5.3.1. Correlation with ELM size

The total inner and outer currents $I_{n=0}$ during ELMs balance, as can be seen in figure 34 within the accuracy of the measurement. In the inter-ELM period the current is negative near the OSP and positive on the ISP, consistent with an electron flow from the inner to the outer strike point. Consequently, it is now interesting to study two distinct properties of these oscillations - namely amplitude and duration - and their correlation to the plasma energy lost during ELMs measured by magnetic probes. First, the amplitude of the ring current in the oscillatory phase (5.4 kA for the ELM shown in figure 34) is compared to the ELM energy loss. Time windows in 20 discharges of the ELM squareness experiment [134] with type-I ELMs were selected based on availability of fast magnetics data and constant strike point position.
The ELM energy loss has an offset-linear relationship with the amplitude of $I_{n=0}$ during the oscillatory phase (extrapolated from five tiles at the OSP where comparatively more TCA were functional during this series of discharges), as shown in figure 35. Each data point represents one ELM. The primary uncertainty results from the extrapolation from currents measured in 15 % of the ring circumference. As only large ELMs above 20 kJ were analyzed due to the measurement accuracy limits, it cannot be stated whether the offset-linear relationship also applies to smaller ELMs. The correlation changes only marginally when considering peak to peak amplitude or the extrapolated sum of the absolute amplitudes of the tile currents. While it is conceivable, no proportionality between the oscillation duration and the ELM energy is found.

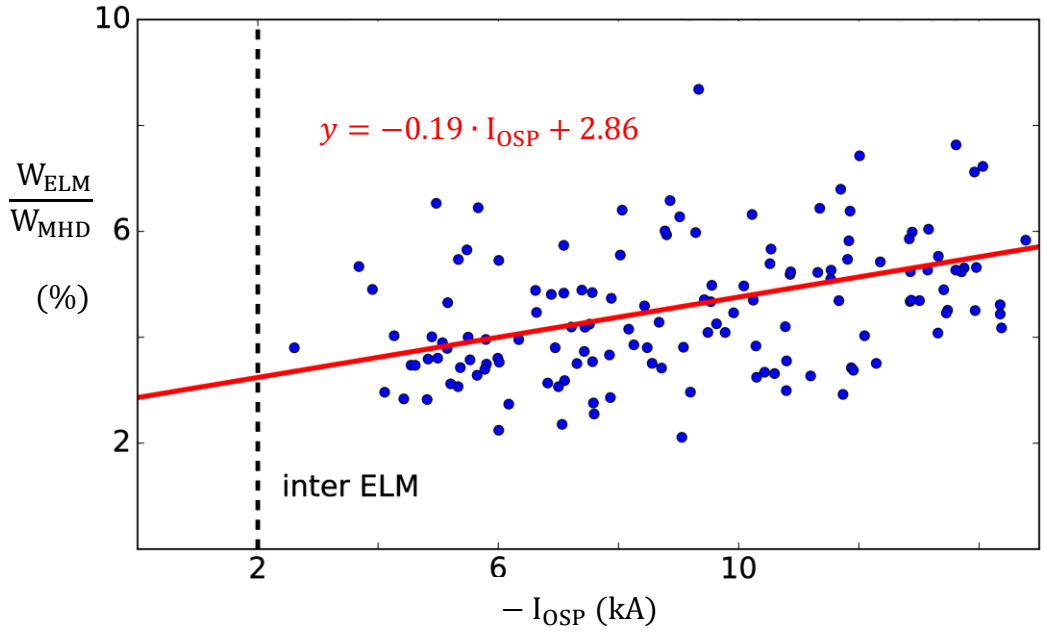

Figure 35 Dependence of ELM size as plasma loss energy on currents near the OSP on discharges 121552-121573. The x-axis is the peak amplitude of the total current $I_{n=0}$ from eq. 5.2 in the oscillatory phase. The dashed line marks the maximum total currents in the inter ELM period, the ELM data linear fit indicates weak correlation $R^2 = 0.48$ (red).

5.3.2. Oscillations and rotation

The frequencies of the current oscillations - determined as the inverse of the time between two current peaks - consist of a mixture of high frequency oscillations (~50 kHz) and low frequency oscillations (~10 kHz). Oscillations with higher frequency than 67 kHz were not seen, even in discharges with 500 kHz TCA sampling rate. It is reasonable to compare the oscillatory phase duration and the expected arrival time of ELM expelled ions in the divertor. During an ELM, the ion transit time $\tau_{\parallel}$ (i.e. the time ions need to move from the outer midplane to the divertor) can be approximated as the ratio of connection length L_C and ion sound speed c_S [141]

$$\tau_{\parallel} = \frac{L_C}{c_S} = \frac{2\pi R q_{95}}{\sqrt{\frac{T_{I,ped} + T_{e,ped}}{m_I}}} \tag{5.3}$$

where R is the major plasma radius, q_{95} is the safety factor at $\psi_N = 0.95$, m_I is the deuterium ion mass and $T_{e,ped}/T_{I,ped}$ are the temperatures of electrons and ions at the pedestal top. Typical experimental values on DIII-D yield transit times of $\tau_{\parallel}$=0.16-0.22 ms ($q_{95} = 4.0, R = 2.1$ m, $T_{e,ped}$=0.6-0.9 keV, $T_{I,ped}$=0.7-1.2 keV). The duration of the oscillations lasts between 0.05 ms and 0.3 ms (determined as the maximum time

difference between clearly distinguishable peaks). While the order of magnitude is consistent (given that $\tau_{\parallel}$ is an approximative formula and that due to toroidal asymmetry not all tile current dynamics can be captured), the variation of the oscillation duration indicates that there are processes that can lead to a quicker end of the oscillations and there are ELMs in which the oscillations blend into the bulk phase. Very fast CER measurements have shown that there are two phases during ELMs: fast particle transport out of the pedestal (<0.3 ms), followed by a slower decrease of temperature (1 ms) [63]. These different transport mechanisms may be related to the dynamics observed with the tile current array.

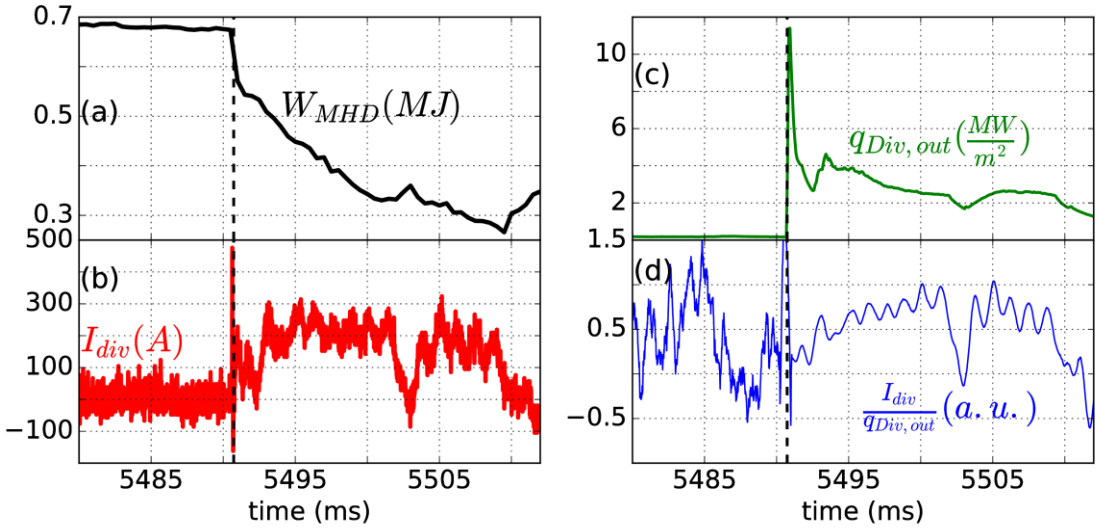

Figure 36 Compound ELM on discharge 147011, 40 ms time window: a) Plasma energy in MJ showing a 300 kJ energy loss b) filter scope (50 kHz) c) Divertor current measured at 60 ° in row 14 (100 kHz) , e) peak outer heat flux in MW/m^2, IR camera at 60 ° (12 kHz)

A pathological, yet interesting case to study these dynamics with is found in the compound ELM. The plasma shown in figure 36 loses approximately 400 kJ (more than half of its energy) during the compound ELM (a). The stored energy trajectory shows a quick initial drop (marked by the dashed line), during which the current oscillation (b) occurs. Also, there is a large spike in the heat flux on the outer strike point (c). The ratio of current and peak heat flux is fairly constant during the bulk phase of the compound ELM (d). Note that time window shown in figure 36 is much larger than the one of figure 30, as the duration of a compound ELM is many times higher than a type-I ELM and that the time derivative of loss of stored energy in the bulk phase is much lower than for a type I ELM. After the initial stored energy drop (dashed line), the energy loss occurs at a fairly linear rate in agreement with a constant heat flux to the divertor. What can be seen is that the tile current correlates well with the heat flux over a 20 ms time window after the oscillatory phase. During this time of constant particle

influx and tile currents up to 200 A, no oscillations are seen. The large stored energy drop during the oscillatory phase (dashed line) is consistent with the correlation of fast ELM transport and large current oscillations and supporting the observation that the initial tile current oscillation regime ceases with bulk particle influx on the divertor.
The analysis of mode rotation patterns emerging from the Fourier decomposition of the oscillatory phase (section 5.2.3) offers another possibility of comparing plasma to tile current properties. For each of the low n modes (n=1 to n=3) a corresponding phase velocity is calculated as average over start and end point of the phase rotation. The emerging current rotation pattern changes strongly from ELM to ELM in whether it rotates at all and which modes rotate. A comparison of TCA rotation frequencies at the OSP to rotation frequencies of the pedestal top measured by CER is shown in figure 37.

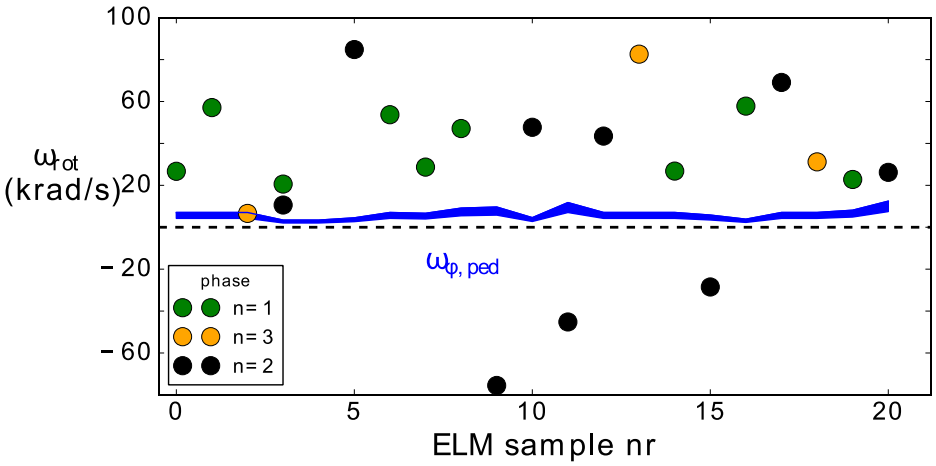

Figure 37 Comparison of toroidal rotation frequency of n=1 to n=3 phases (only shown if rotation is measured) during the oscillatory phase of multiple ELMs to toroidal rotation frequencies measured by CER near the pedestal top just before the ELM crash (blue)

For this comparison 60 ELMs were selected from four different discharges with fast CER data (2 kHz sampling frequency). 40 discharges were rejected as they did not show discernable rotation of Fourier modes of the current. Note that a consistent phase locking was not found. For the remaining 20 discharges, the rotation mostly originates from the n=1 and n=2 phases. Figure 38 conveys that the toroidal carbon rotation frequency is lower than the phase rotation at the outer divertor, and much lower than the oscillation frequencies of the TCA measured currents (10-70 kHz). However, as the maximum ExB drift frequency in the steep gradient region is considerably higher than the pure toroidal rotation and phase rotation frequencies, a connection to perpendicular drifts will be investigated. The radial electric field E_r has the shape of a well in the plasma edge and causes an ExB drift in perpendicular direction of the size

$$\omega_{ExB} = -\frac{E_r}{R \cdot B_\theta} \tag{5.4}$$

with R, B_θ radius and poloidal magnetic field strength at the outer midplane and the radial electric field computed from force balance (of carbon CER measurements on DIII-D) as

$$E_r = \frac{\nabla p_\alpha}{q_\alpha n_\alpha} + v_{\phi,\alpha} \cdot B_\theta - v_{\theta,\alpha} \cdot B_\phi \tag{5.5}$$

where B_ϕ is the toroidal field strength and α refers to the respective species and their charge q, pressure gradient $\nabla p = \frac{dp}{dr}$ and edge density n. The first term of equation 5.5 is also referred to as diamagnetic term and its contribution to the ExB drift frequency as diamagnetic drift, with electron and ions drifting in opposite directions.

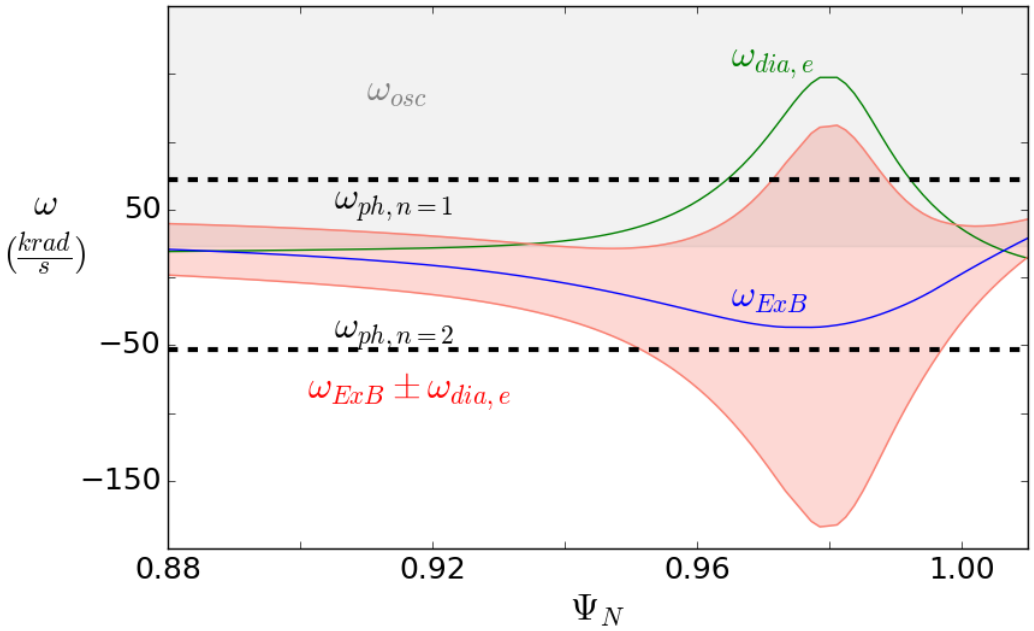

Figure 38 Diamagnetic (green) and ExB rotation (blue) frequency at the plasma edge, range of expected rotation from simulations [142] (red) and TCA measurement (black, dashed lines) during discharge 119433.

A comparison of ω_{TCA} of two different ELMs with rotating n=1 and n=2 phases to ω_{ExB} profiles is illustrated in figure 38. ω_{TCA} rotates in the electron diamagnetic for n=1, respectively ion diamagnetic direction for n=2. Quantitatively both cases agree with an origin in the steep gradient region (assuming a frequency bandwidth of $\omega_{EXB} \pm \omega_{dia,el}$ found as appropriate limit in simulations of finite width islands [142]). As the

Discharge	E_R [kV/m]	$\omega_{dia,C}$ [kRad/s]	$\omega_{dia,e}$ [kRad/s]	ω_{ExB} [kRad/s]	$\omega_{tor,ped}$ [kRad/s]	ω_{TCA} [kRad/s]	ω_{osc} [kRad/s]
119432	-30	-21	142	-44	-15	6 - 84	35 - 250
119433	-26	-18	130	-38	-9	-75 - 53	23 - 310
119434	-22	-24	188	-32	-9	-28 - 82	48 - 250
119440	-12	-22	72	-18	-12	22 - 69	29 - 310
121560	-43	-38	115	-46	0.4	-	78 - 157
118252	-15	-14	54	-21	-9	-	35 - 250

Table 7 Overview of rotation quantities for three different discharges between 3.0±0.3 s: Toroidal pedestal Carbon rotation frequency $\omega_{tor,ped}$, radial electric field E_R and diamagnetic contributions $\omega_{dia,C}$ and $\omega_{dia,e}$, ExB rotation frequency ω_{ExB}, TCA phase rotation ω_{TCA} and TCA oscillation frequency ω_{osc}.

analysis of several discharges conveys (table 7), the limits of $\omega_{EXB} \pm \omega_{dia,el}$ are considerably higher than the pure toroidal rotation frequency, on the order the low n mode rotation (ω_{TCA}) and at the lower end of the current oscillation frequency. Most of the ELMs from the previous figure 37 are consistent with a phase rotation in the electron diamagnetic direction.
As many ELMs do not show rotation patterns and no clear correlation with drift frequencies can be shown, the rotation analysis remains inconclusive indicating that multiple processes could be involved determining the resulting TCA measurement.

5.3.3. Magnetics

Since currents flowing in plasma and SOL produce their own magnetic fields, it is very interesting to compare the tile current array measurements to magnetic probes. Auto spectral density analysis of fluctuation measurements from an internal magnetic probe and TCA (figure 39) shows the correlation in frequency space between the measurements. The magnetic probe is localized at 135° toroidal with 1 MHz sampling frequency, whereas the TCA sensors are at 115º (ring 10) and 200° (ring 14). In the inter-ELM phases the n=1 mode around 20 kHz is clearly detected both on magnetic probe and TCAs (d). During ELMs, a large excitation of the frequency range between 0 and 80 kHz is observed, starting with the oscillatory period (b). In the auto spectral density panels (a,c), the ELMs are hence recognizable as vertical yellow bars. In [143] the concept of solitarity was introduced, as a measure for the peaked-ness of the early magnetic perturbations during ELMs described in a parameter termed *slt*. It is calculated as ratio of the mean value of a Fourier transformation of a signal to its peak. In this case, both magnetics and inner divertor TCA have an *slt* of 0.041 (outer: 0.049), so that - in accordance with [143] - they can be categorized in the transition between

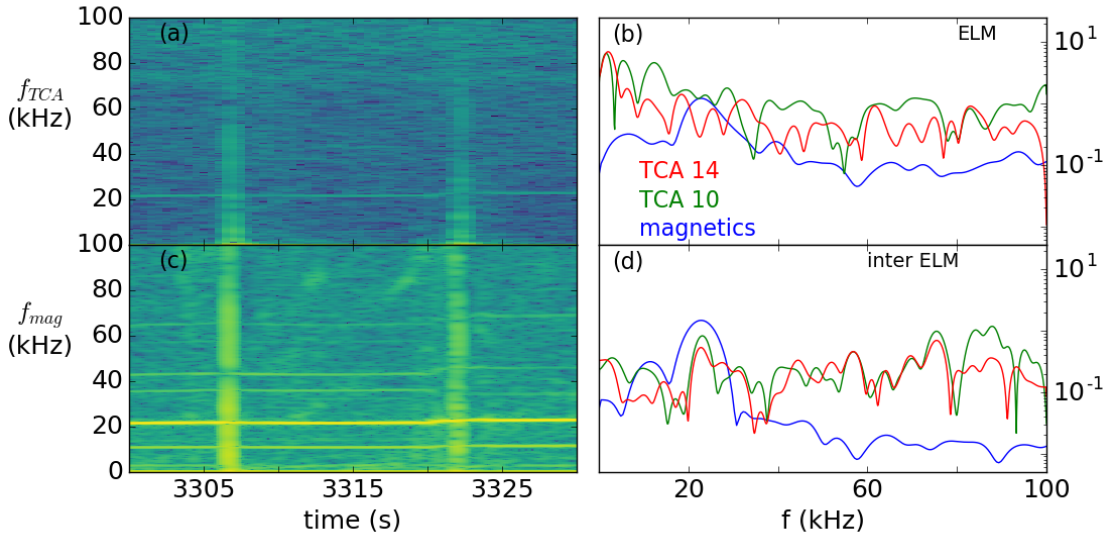

Figure 39 Auto spectral density of TCA and magnetics during discharge 119433 (left), power spectral density at selected times during an ELM (3321.85±0.25 ms) and in the inter ELM phase (3326.05±0.25 ms) for a fast magnetic probe (blue), a TCA sensor near the inner (green) and outer (red) strike point. The power is plotted as square root of the power spectral density.

strongly peaked and less pronounced peaked ELMs, which are more likely to occur at lower collisionality. Intense analysis on the resulting magnetic probe measurement of filamentary currents has been done elsewhere, identifying low-n structures as dominant at the ELM onset as likely emerging from the steep gradient region [143]. Unfortunately, a comparison between TCA-measured and magnetics-measured mode numbers is impractical, as the spatial resolution of the old magnetic probe system on these discharges only allows poorly conditioned fits and vice versa (i.e. the present magnetics providing great magnetics data can only be compared to poorly conditioned TCA fits).

The good correlation of magnetics and tile currents raises the question, whether the tile currents can evoke a similar effect as external 3D-field coils by perturbing the plasma equilibrium: For instance, the current in the n=3 component figure 34, reaches a peak of 3.0 kA. Even if the current were flowing in the outer SOL at maximum distance to the confined plasma (which corresponds to 3 cm distance to the confined plasma around the midplane, field lines further out intersect with the vessel) this will - in the frame of a snap-shot - create a field of 0.02 T at the separatrix according to Ampere's Law. This corresponds to about 1.3 % of the LFS magnetic field and is stronger than all RMP fields on DIII-D, showing the importance and potential impact of the ELM currents, that will be inspected in the following chapter.

In summary, correlations between ELM properties and tile currents are found between the tile current amplitude and the ELM size. While rotation is only detectable in the minority of the inspected ELMs, the origin of mode rotation – if present – is likely localized in the outer pedestal and possibly related to diamagnetic or ExB drifts.

5.4. ELM current model (ECM)

The previous sections have summarized experimental findings of ELM currents on DIII-D. Due to their large size and critical time of appearance, understanding the origin, nature and impact of these currents is indispensable for a better understanding of the nonlinear ELM phase. In the following, an interpretation of the experimental data is made and arranged in the ELM evolution. While it will be shown that the obtained model is consistent with experimental measurements, it is partly based on hypotheses that by themselves cannot be verified with the available experimental data and are clearly marked as such. As tile currents play a major role in the model, it is referred to as the ELM current model (ECM). The ECM describes a mechanism leading to explosive growth and additional transport in the nonlinear ELM phase. The physics of such a mechanism has been identified as missing in contemporary nonlinear ELM simulations by JOREK and M3D [78,79,144]. Without this mechanism ELMs would likely be less violent and of longer duration. While a full nonlinear simulation cannot be presented yet, all stages described in the following can be understood and expected as ad-hoc snap shots during such a simulation. The ECM proposes the following explanation for the tile currents during ELMs:

- after exceeding the peeling-ballooning stability threshold, loss of energy and particles sets in at the pedestal; the electron heat pulses lead to a rise of plasma temperature in front of the divertor causing thermoelectric currents (this mechanism has been suggested in a conceptual model for ELMs put forward by Evans [145])
- these currents flow through error field produced flux tubes between ISP and OSP in the confined plasma and in a self-amplifying mechanism, more and larger flux tubes are produced (demonstrated by Wingen [146]), degrading the plasma confinement and causing transport
- when the pedestal has regained stability and the arrival of ions in the divertor has balanced thermal gradients, the drive for the thermoelectric current ceases and the transition to the filamentary phase sets in with the pedestal recovery

Since the thermoelectric currents of the ECM do not contribute to initial ELM triggering, they will not alter the onset criteria, which is well described by linear peeling-ballooning theory but may be crucial in the nonlinear evolution. The details of the ECM will be explained in the following, starting with the nature of flux tubes in the confined plasma.

5.4.1. Existence of flux tubes through plasma

To understand the path of current flow, field lines intersecting with the divertor tiles through which the currents are measured are traced employing the MAFOT [147] code. MAFOT is a field line tracer based on TRIP3D [148] (a well-established field line

tracing code) and uses the field produced by the plasma current and toroidal field coils as well as error fields or applied fields introduced through various coils. On DIII-D these non-axisymmetric fields originate from imperfections in the toroidal field coil itself (B-coil) and additional field contributions from error field correction and 3D-field coils (labelled I- and C-Coils). MAFOT confirms the conceptually predicted breakup of the separatrix in two parts [145,149–151] - so called manifolds - through the application of non-axisymmetric perturbations. Even small perturbations will lead to separatrix splitting near the X-point, where there is no poloidal magnetic field. The code demonstrates that the two manifolds form an oscillation pattern towards the X-point. At the intersections of the two manifolds within the separatrix, flux tubes are

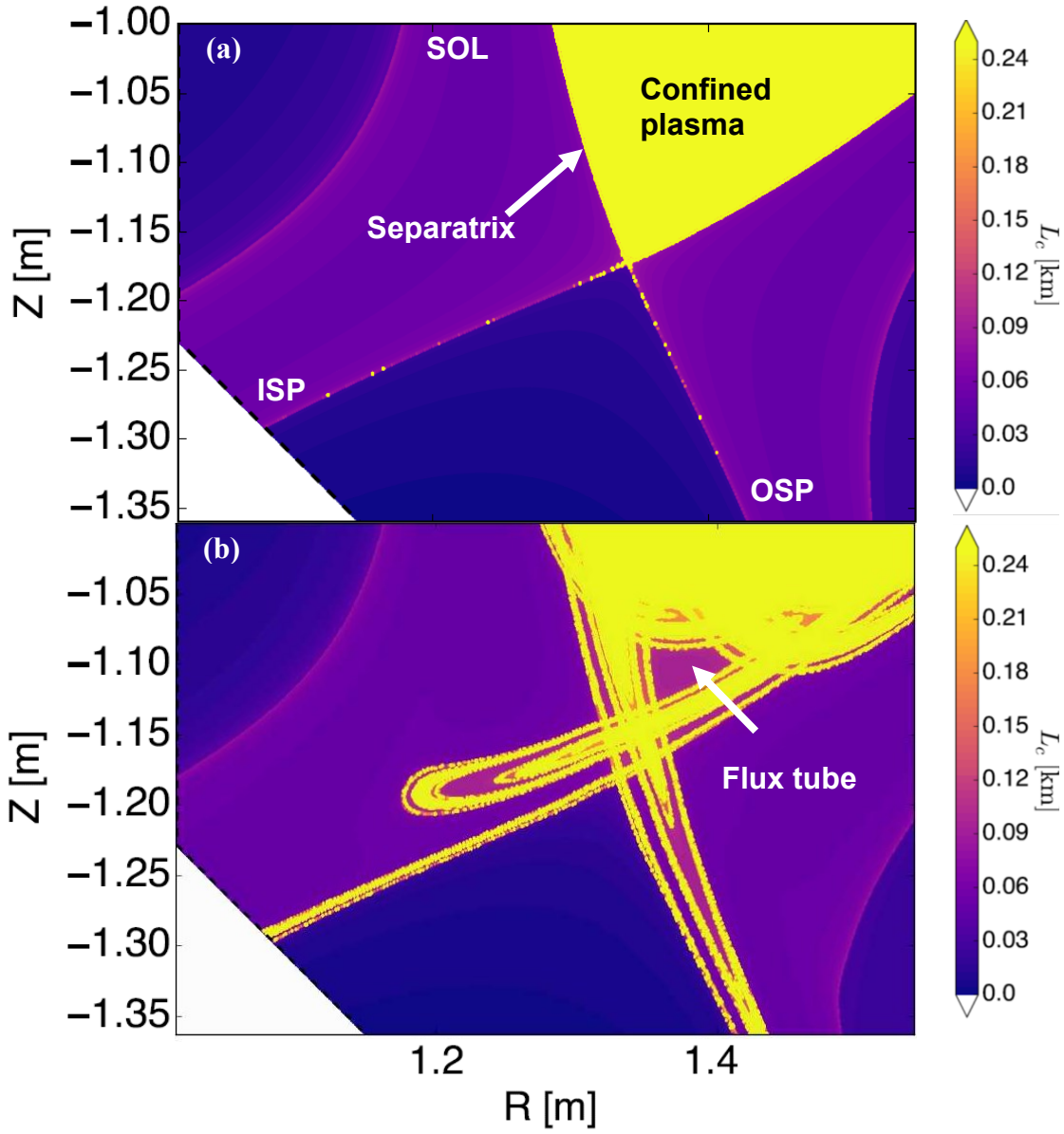

Figure 40 MAFOT connection length calculation of discharge 121560, based on a) solely kinetic equilibrium of 80-99% ELM phase between 2.75 s - 3.25 s b) additional error fields from C-Coil, F-Coil and B-coil: Spatial location of short connection length flux tubes between the inner and outer divertor inside of the separatrix and their respective length L_C.

formed connecting the two divertor sides and tiles upon which the strike points reside [146]. At the intersection with the target plates lobes are formed. These lobes have been verified in simulations [128] and experimentally seen on DIII-D [152,153] and MAST [154]. The flux tubes are of short length (typically two poloidal turns between the target plates) and inside the stochastic region of the plasma edge, while they themselves are non-stochastic (the field lines within the tube are parallel and of equal length). Larger error fields increase the size and number of these flux tubes.
For illustration, discharge 121560 is analyzed in a 0.5 s time window around 3 s. The resulting connection lengths of magnetic field lines between outer and inner divertor are computed by MAFOT and the topology near the X-point and divertor is presented in figure 40. The figure shows the effect of separatrix splitting by error fields. While the connection length in a) are solely based on a kinetic EFIT (80-99 % ELM phase, assuming perfect axisymmetry) and display a well-defined separatrix, the analysis with known error fields from the DIII-D C-Coils, F-Coils, and B-coil results in relaxation of separatrix degeneracy and existence of short connection length flux tubes (b). These are recognizable as areas of purple color surrounded by yellow colors of the confined plasma.
The MAFOT code can and has been to compute additional effects on magnetic topology associated with simulated currents flowing through the short-length connection tubes or the SOL respectively. Previous ELM simulations on DIII-D with MAFOT have shown that the IR heat flux footprint geometrically aligns with MAFOT predictions of field line widening at the strike point due to currents flowing through the confined plasma [152]. Agreement between predictions of currents connecting outer and inner divertor through the confined plasma and Langmuir probe measurements has also been found on JET [155]. Note that these numerical results are instantaneous snapshots of perturbed equilibria in the vacuum field approximation, their temporal evolution cannot be modelled by MAFOT. At present the plasma response is not included in the model. While it is well known that H-mode plasmas respond with screening towards external fields, it has been shown elsewhere that including the plasma response reduces the initial penetration depth of flux tube structures but does not fundamentally affect the existence of a large number of flux tubes [156]. Additionally, the contribution of the initial ballooning mode to the flux tube topology is missing. Since rotation of Fourier components is not consistently measured (section 5.2.3) a competition between error-field-provided, static flux tubes and ballooning evoked rotating flux tubes as seed for the first perturbation is possible. Note that heat flux patterns on AUG during application of RMPs in L-mode could be modelled without considering error field produced flux tubes in the plasma [157]. Hence, the impact of these flux tubes is likely scenario dependent.

5.4.2. Comparison of SOL to confined plasma currents

It has been suggested elsewhere that all of the ELM tile currents are flowing through the SOL [140]. While there are certainly currents in the SOL associated with filaments expelled in the post-oscillatory ELM phase [158], it will be shown that the current

measured during the oscillatory period is more consistent with a flow through flux tubes in the confined plasma. The present model builds on experimental evidence from other devices, which indicate a temperature increase preceding the bulk particle and heat flux pulse of the ELM. In particular, measurements with Langmuir probes on the TCV tokamak showed that increased temperature can be detected as early as 0.15 ms before a heat flux increase [138]. Although comparable measurements were not available for the DIII-D experiments in consideration, these types of observations suggest that thermoelectric effects can be at the origin of the currents observed in DIII-D. After the plasma edge exceeds the peeling-ballooning stability threshold, the loss of edge confinement leads to emission of particles and energy towards the divertor. Due to their higher velocity electron conducted heat will arrive within several microseconds at the divertor delivering a heat pulse and leading to local hot spots on both divertor sides [141]. These hot spots in front of each divertor side are connected through magnetic field lines in confined plasma flux tubes or SOL to colder spots on the respective other divertor side of the field line. Consequently, a temperature gradient parallel to the field lines builds up, producing a thermo-electric current with electrons flowing to the hotter side.

The flux tubes are distorted strongly in the divertor region due to the magnetic field changes, in particular the small poloidal field. By tracing field lines within the error field produced flux tubes of discharge 121560 (annotated in figure 40b), it can be shown that the tubes are stretched in the toroidal and compressed in the radial direction, so that a radial deposition width in the divertor between 0.001 and 0.02 m is calculated with a toroidal angle coverage of up to 260°. Additionally, several of the tubes overlay in the same toroidal area. The MAFOT-predicted short flux tubes for discharge 121560 have an average connection length of approximately 90 m.

Based on the assumption that the tile currents are of thermo-electric nature, Staebler's thermo-electric current model is implemented here: The field line length corresponds to the 90 m flux tube length. Strictly speaking, Staebler's model is developed under the assumptions of negligible pressure gradient between the end points and approximately constant or linearly varying conditions along field lines. In general, these conditions are not expected to be met throughout the later ELM phases. While the exact drive of the current might vary, the sheath conditions determining the maximum current flow will hold during the oscillatory phase. Hence, to check for consistency with the TCA measurements, the absolute size of the current needs to be calculated based on path and the area through which the current flows. The tile width is 0.12 m and the MAFOT simulation result of an average radial current inflow width of 0.01 m can be used to solve equation 2.49 numerically and obtain the thermo-current to a tile. For SOL currents, field lines outside of the separatrix are traced between the divertor sides. At a certain radius there is no connection to the inner divertor any more, since the field lines intersect with the upper divertor. For major radii between 1.45 m and 1.49 m the connection length amounts to 50 m according to MAFOT, since it is only one poloidal turn (this approximately equals $2\pi R q_{95}$).

	ELM current through flux tubes in confined plasma	ELM current in SOL
$\mathbf{n_e}$ $[\mathbf{10^{19}m^{-3}}]$	2.0	1.0
$\mathbf{n_i}$ $[\mathbf{10^{19}m^{-3}}]$	2.0	1.0
$\mathbf{T_e}$ [eV]	60 - 100	10 - 60
$\mathbf{L_C}$ [m]	90	50
$\mathbf{n_I}$ $[\mathbf{10^{19}m^{-3}}]$	5.0	
$\boldsymbol{\tau_{ie}}$ $[\boldsymbol{\mu s}]$	0.53 - 1.15	0.07 - 1.07
$\boldsymbol{\sigma}$ $[\mathbf{10^{24}Sm^{-1}}]$	5.3 - 11.4	0.3 - 5.3
$\boldsymbol{\gamma}$	0.53 - 1.14	0.07 - 0.95
$\mathbf{T_O}$ / $\mathbf{T_I}$ [eV]	30 eV / 10 eV	
I ($\frac{\mathbf{T_O}}{\mathbf{T_I}}$ =2.0) [A]	210 - 260	50 - 260

Table 8 Comparison of plasma parameters and resulting divertor currents for flow through flux tubes in confined plasma or through SOL. Input parameter for equation 2.49 and resulting tile current at a divertor temperature ratio of 2:1.

Table 8 gives an overview of plasma parameters for current flow through flux tubes in the confined plasma or SOL. The ranges are obtained by dividing respective field lines in 1° toroidal segments and assigning each its temperature and density according to its grid value from the kinetic EFIT. Non-axisymmetric profile imbalances are hereby neglected, and the assumption is made that the temperature and density in the flux tube correspond to their local environment. Densities are evaluated from Thomson profiles in the kinetic EFITs to amount to $1.5 \cdot 10^{19}\mathrm{m}^{-3}$ near the separatrix and approximately $1.0 \cdot 10^{19}\mathrm{m}^{-3}$ in the far-out SOL (see table 8). Aside from the connection length (taken from MAFOT), the most substantial difference results from the temperature in SOL and confined plasma. They are assumed to be 10-60 eV (SOL path) and 60-400 eV in average along the field line, which is in accordance with contemporary available 2D Thomson divertor spectroscopy on DIII-D [159]. With these assumptions, one obtains a γ-range (equation 2.49) of 0.1-1.1 for the SOL path and a range of 0.5-1.1 for the flux tube. The resulting parallel current I_{par} for a single tile is shown in figure 41 for different values of the γ parameter due to dependence on the temperature ratio $\frac{T_O}{T_I}$. With a lower γ value, a higher temperature difference between the strike points is necessary to drive the same current. The Langmuir probe measurement on the TCV tokamak measuring the initial heat pulse has resulted in a temperature ratio of 2-3 : 1 [138]. Assuming a peak ion target density of $5.0 \cdot 10^{19}m^{-3}$ and a DIII-D typical 10 eV on the cold and 30 eV on the hot side [159] yields a peak current of 295 A for the flux tube path. Average SOL temperatures of 30 eV ($\gamma = 0.4$) are necessary to drive 200 A; for lower temperatures the achievable peak currents are below the measured values. At approximately 295 A, the predicted ion saturation current is comparable to measured peaks during 121560. While this instantaneous picture favors the flow through the plasma, it does not rule out SOL currents in the near plasma/strike point region with

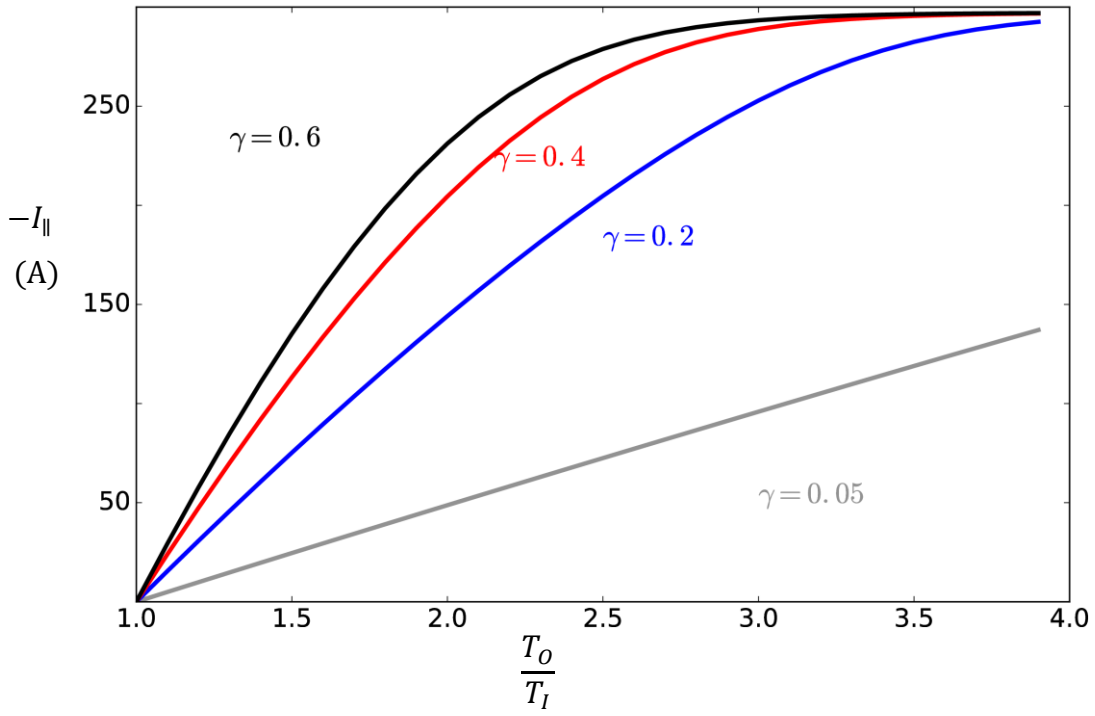

Figure 41 Calculated size of the thermoelectric currents at the end of a 100 m long connecting flux tubes in dependence of the temperature ratio at the end of the tubes for different values of the conductance-like parameter γ. The experimental value is γ= 0.35.

high SOL temperatures (especially in low collisionality, conduction limited SOL cases, with very little temperature gradient).

Considering the magnetic topology and confinement, a current in the plasma edge has a much stronger impact on the plasma than a SOL current as shown in figure 42. In both cases a current of 500 A between tiles of ISP and OSP is simulated. For the flux tube current scenario, 500 A in the large tube near the X-point (marked in figure 40b) correspond to the early phase of the nonlinear ELM where approximately 50 A peak are measure on each tile (and multiple tiles are connected through the same tube due to the distortion in the divertor region). For the SOL current scenario 500 A are an overestimate of the measured peak values of up to 300A. Figure 42 is based on the same equilibrium with error fields as shown in figure 40b (so the degeneracy of the separatrix has already been removed by the error fields). A typical field line within the near separatrix SOL (a) and within a large flux tube (c) is traced and the color code indicates the temperature along the field line. It is obvious, that the SOL field line is shorter, but also colder in comparison to the flux tube field line. For both cases a current of 500 A flowing along the field line between tiles of ISP and OSP is simulated with MAFOT and the new magnetic topology represented by length of divertor connecting field lines (b,d). Compared to figure 40b, minor changes of field topology occur compared to the original error field plasma when assuming SOL currents (a, b), while in the case of flux tube current in the confined plasma (c, d) the divertor foot is widened and more and

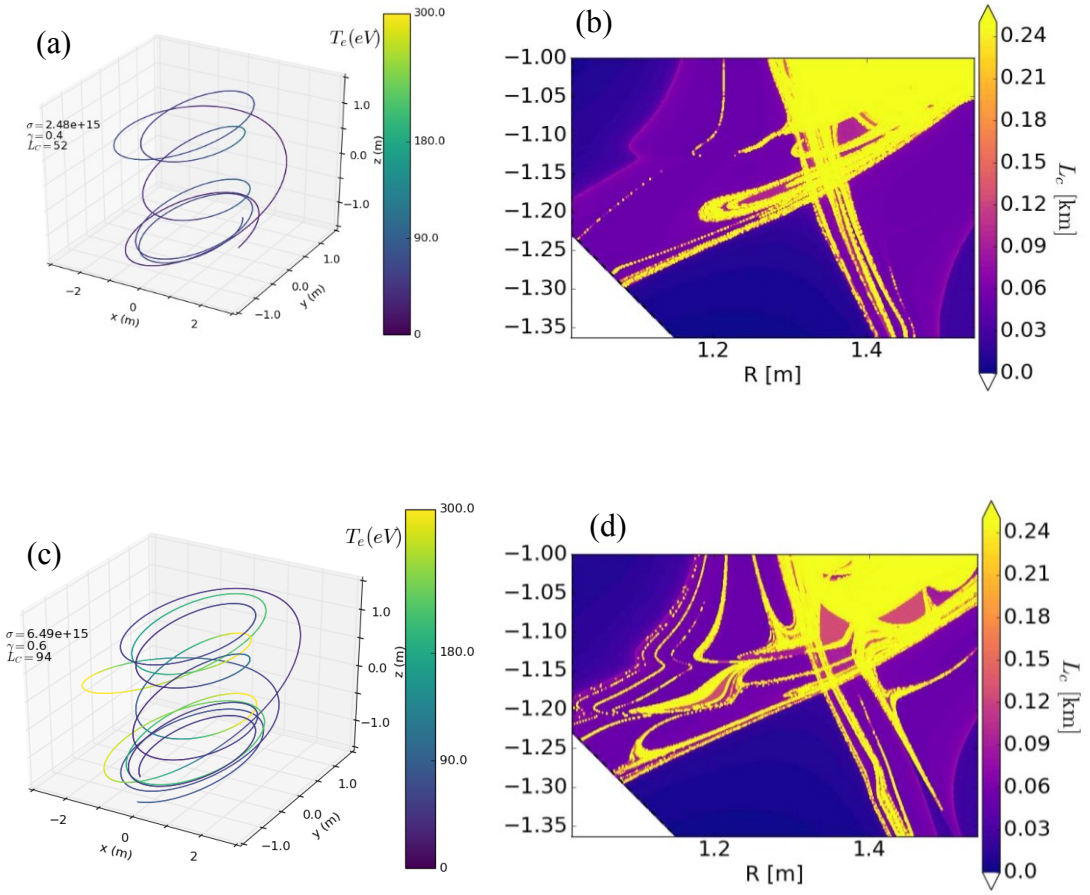

Figure 42 MAFOT connection length L_C calculation of discharge 121560 with a current flow of 500 A and trace of flux tube: a-b) in the near strike point SOL c-d) in a flux tube through the plasma

larger flux tubes are produced in the plasma as a result of the self-amplifying process. The emerging flux tubes due to the current flow in the initial flux tube penetrate deeper into the plasma (also seen in previous MAFOT runs [147]), i.e. regions of even higher temperature and possibly lower resistance. As the current in the flux tubes increases so will the surrounding stochasticity. In addition, size and number of resonant islands (i.e. large flux tubes near resonant surfaces) will increase with the current in the flux tubes, so this becomes the instability drive rather than the pressure gradient that was responsible to the initial (linear) instability onset. The expansion of the stochastic region as more heat is fed into the flux tubes leads to decreasing confinement and stored energy in the plasma and more thermoelectric current drive. This is the explosive nonlinear instability that takes over the dynamics following the rather short linear phase. The nonlinearity is quenched when the expansion of the stochastic region (island growth and overlap) slows down and cuts off the heat flux into the flux tubes. The process can be compared to a Jacob's ladder with the plasma edge representing the air

between the two electrodes (corresponding to the divertor sides). The higher temperature in deeper layers of the pedestal drives the nonlinear growth but finally causes its cessation. The exact mechanism is not understood yet. It is to be expected that after the onset of the ELM currents (i.e. in the oscillatory period) the majority of current will flow in flux tubes as their resistance will be increasingly lower, while the SOL resistance should remain relatively constant. Nevertheless, a fraction of the currents will also flow in the SOL, as shown in [158], among others driven by filaments or radiation [160].
Based on these calculations the consistency of IR heat flux and current measurement during the oscillatory phase presented in section 5.1.2 can be shown a posteriori: Assuming a radial current flow/heat flux width of 0.5 cm in the divertor and that the electron pulse heats the plasma in front of the tile within a distance of 0.03 m, one yields an affected divertor plasma volume (with the same current deposition width properties as above) of 0.17 dm^3. With an average heat pulse temperature of 50 eV (resulting from a mix of high temperature electrons from the pedestal top and low temperature electrons from the separatrix) near the divertor and an initial local ion density of 10^{19} m^{-3} a temperature increase from 10 eV to 20 eV is required to reproduce the typical current spike of 50 A over 0.01 ms. If the hot electrons from the plasma transfer about 25 % of their kinetic energy (assumed 50 eV) to the local plasma (and the rest to the divertor), the electron pulse would need to have $1.4 \cdot 10^{14}$ particles which is less than 0.1 % of all electrons in the confined DIII-D plasma, and the resulting heat flux amounts to 0.15 MW/m^2 which is slightly below the IR noise level of 0.2 MW/m^2. This estimate shows that an initial heat pulse during the ELM sufficing to trigger thermoelectric currents will remain unnoticed by the presently available IR camera.

5.4.3. Inter ELM current flow

While the ECM is dedicated to ELM related currents, it is worth mentioning, that the temperature-ratio/current curve shown in figure 41 is also consistent with inter-ELM measurements and sufficient to explain inter ELM currents. The tile currents amount to 40 A in forward B_T scenarios, which corresponds to a plasma temperature ratio of 1.2 : 1. In forward B_T the outer divertor and the plasma in front of it receive more heat load than the inner divertor on DIII-D and heats up stronger, leading to a net inflow of electrons due to a thermo-current in agreement with the theory [94]. Consistent with the reversal of the divertor heat load asymmetry with B_T direction [85], the tile currents change direction in reversed B_T and are smaller in amount (only 10-20 A are measured). The exact conductivity along the flux tubes will in general be between its two extreme limits:

- as the flux tubes are connected to the divertor/SOL region with much lower temperatures, the low-conductivity/high resistance limit is formed by assuming divertor plasma temperatures in the flux tubes, due to the high parallel transport

along them. This is unrealistic in so far as the low temperature flux tube in the hot confined plasma would lead to very high perpendicular transport ($\gamma = 0.1$)

- the high-conductivity/low resistance limit is formed by assuming temperatures in the flux tube are corresponding to their nested flux surface. This is unrealistic as one would assume a steep gradient in temperature at the transition from confined to SOL plasma ($\gamma = 1.1$)

Within these assumptions for the inter-ELM phase both SOL current flow and current flow through flux tubes are consistent with the measurements. Further quantitative modeling is necessary to understand the effect of temperature profiles on conductivity and the plasma response.

5.5. Validation of the ECM

In order to validate the ECM, a balanced double null discharge (DND) with two X-points is analyzed [133]. In a perfectly balanced DND, the inboard and outboard SOL are topologically separated and there is no field line connection between LFS and HFS. Figure 43 shows the kinetic equilibrium for a reversed B_T discharge with a balanced DND around 2.5 s (119150), and examples of fast TCA signals from upper OSP (a), lower ISP (b) and OSP (c), which are sampled at 200 kHz. The dashed vertical lines mark a 0.03 ms time window after the initial current perturbation. One can see the current spikes simultaneously at lower ISP and OSP. Nonlinear ELM simulations of DIII-D have shown that it takes about 40 Alfvén times (0.015 – 0.03 ms) for the ELM perturbation to spread from the outboard ballooning LFS to the HFS [144].

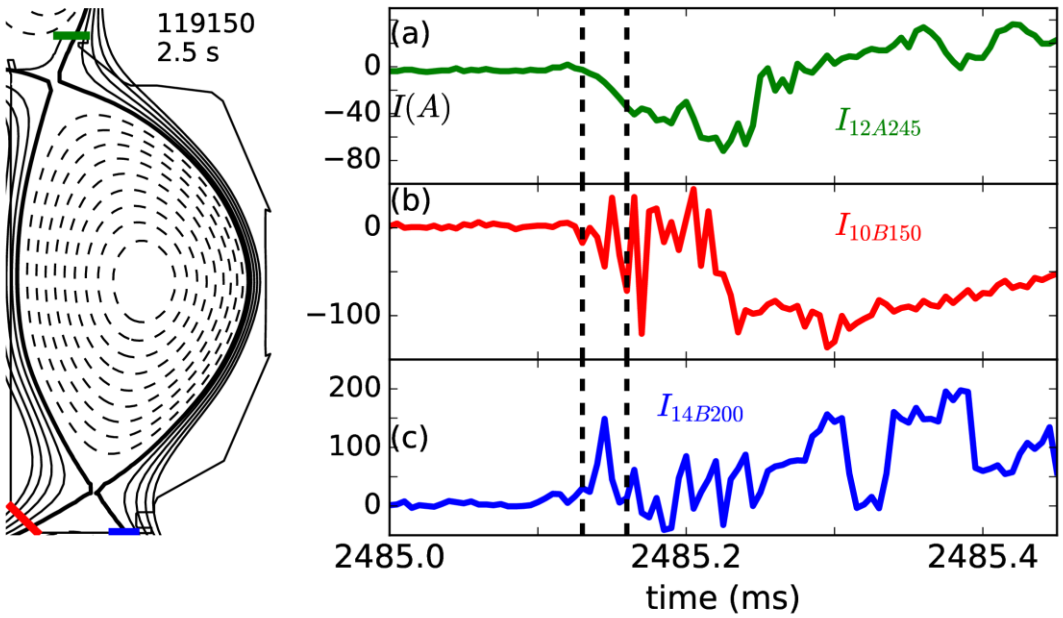

Figure 43 Tile current evolution during 0.5 ms ELM in DN discharge 119150 (EFIT, left): TCA measurements from upper OSP (a), lower ISP (b) and OSP (c). The dashed lines mark the 0.03 ms time window needed for the ELM to spread from LFS to HFS.

This delay has been confirmed experimentally in fast reflectometer density measurements on LFS/HFS on AUG [161]. If one assumes that the tile currents are based solely on currents in the SOL caused by perturbations of the plasma through the ELM, one would expect the current change on the high field side to occur delayed compared to the low field side current, since it takes a discrete time window for the

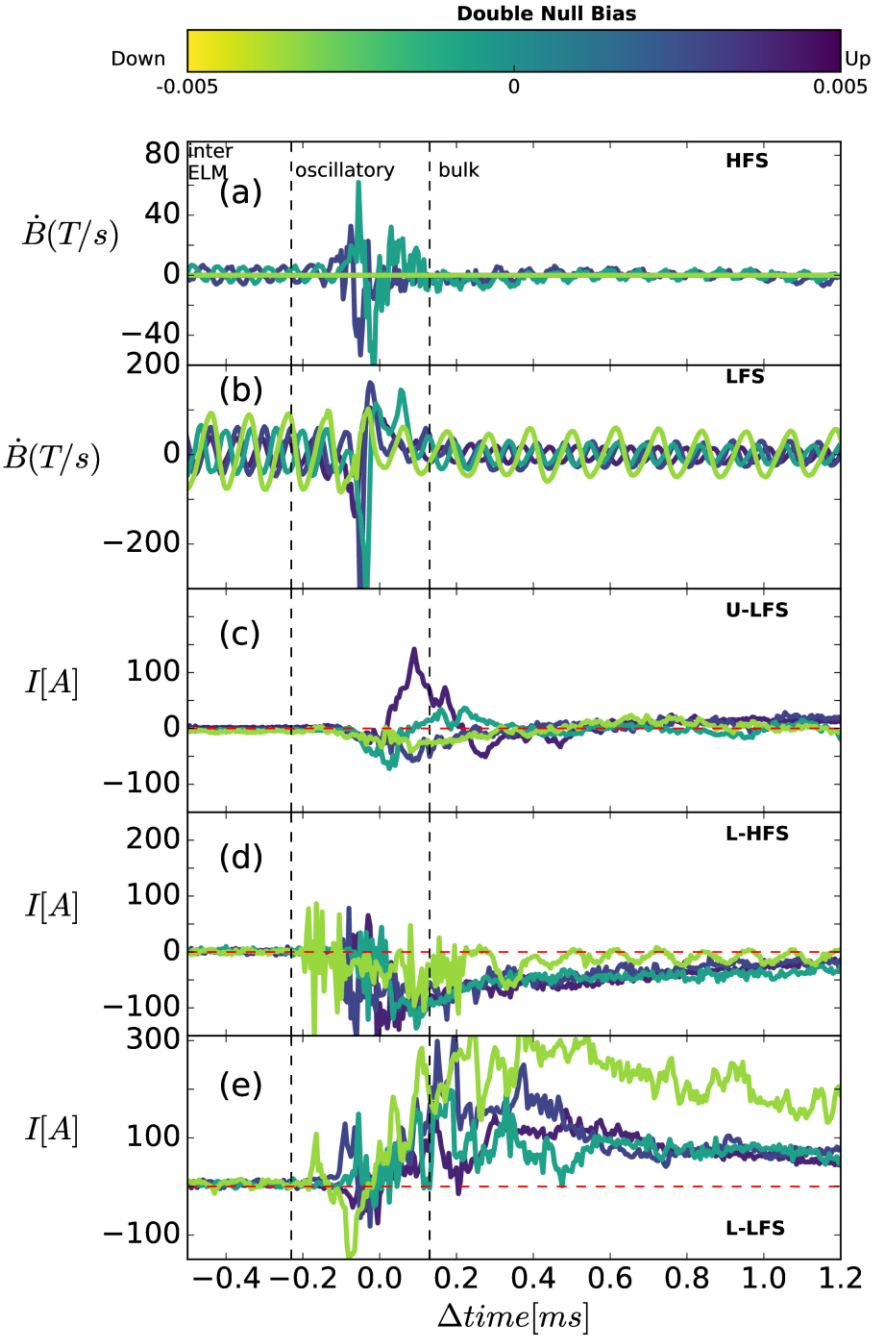

Figure 44 ELM evolution in dependence of magnetic balance on discharge 119150: Magnetic probe signals relative to Dα peak (not shown here) on a) HFS (322°, no data available for biased down case) b) LFS (167°); Tile current measurements on a) upper low field side, lower d) high field side and e) low field side. Typical ELMs for upwards bias (blue), downwards bias (lime green) and balanced DN shapes (turquoise). 0.3 ms oscillatory time window for comparison to purely LSN ELMs.

perturbation to spread from the LFS to the HFS in the plasma. Hence, one would expect delayed tile current onset between inner and outer divertor (e.g. delay of dashed line time frame between peaks of red and blue trace in figure 42). The experimental result of simultaneous rise of ELM currents measured on HFS and LFS cannot be explained solely based on SOL currents but is indicative of a flux tube passing inside the separatrix between the two sides and as such consistent with the ECM.

In this particular discharge, the plasma shape is changed from an upwards biased DN, to a balanced DN and then to a downwards balanced DN over a time window of 3.0 seconds. To rule out the uncertainty about the time point at which the exact DND topology is achieved, figure 45 illustrates for typical ELMs (a selection of 4 ELMs out of 1.5 second time window during the transition was made) how the magnitude of ELM related magnetic perturbation is affected on the HFS and LFS throughout the shape change (a,b). The color code represents the dR_{sep} parameter, a measure for magnetic balance of the shape defined as radial distance at the outer midplane between flux surfaces connected to the upper and lower X-points. A pure LSN plasma implies dR_{sep} values below -0.035 m (light green), a USN plasma has 0.035 m and above (light and dark blue), the perfectly balanced DN scores 0.0 m (turquoise). All signals are shown relative to the peak of the Dα-signal near the lower OSP. Independent of the bias, the tile currents near the strike points of the lower divertor rise simultaneously (d,e). As expected, for an upwards biased DN case the current increase on the upper divertor LFS (U-LFS) is larger than in the other cases (c) and for LSN-bias the current near the lower OSP resembles the oscillatory – bulk phase as in purely LSN cases. The current on the L-LFS in the main phase is unusually large and likely due to a current carrying filament (while not shown here, the current on the neighboring tile is considerably smaller in the main phase). These observations are consistent with the ECM interpretation of tile current, since large, simultaneously occurring tile currents are measured on the HFS, even though virtually all power in this balanced DN shape is delivered to the LFS during ELMs [133]. Additionally, while the magnetic SOL perturbation on the HFS is delayed, there is no delay found in ELM related magnetic probe signals on AUG [161] and DIII-D (a,b), consistent with the ECM predicted perturbations induced by current flow inside the nominal separatrix through LFS and HFS.

The connection length plot of the MAFOT simulation of this discharge in the balanced DN time interval (figure 45a) is similar to the LSN discharges (figure 42) with the exception that there are two X-points. The figure shows that the error fields of the DIII-D coils have strongest effect near these X-points where a number of lobes is formed(a). Adding a filament with only 150 A near the lower X-point (in agreement with the early L-OSP measurement) produces a large number of additional lobes on all strike points, in agreement with the measured currents (b). This effect has already been shown in figure 42d; however (b) demonstrates that flux tube currents near the lower X-point also affect the magnetic topology near the upper X-point. This is because the connecting flux tube (d) is about three times longer than a simple HFS-HFS field line (c) and passes both HFS and LFS. However, since the LFS-HFS field line connects through areas of the hotter plasma the γ-factor is comparable (γ=0.9 vs γ=0.7) based on similar divertor

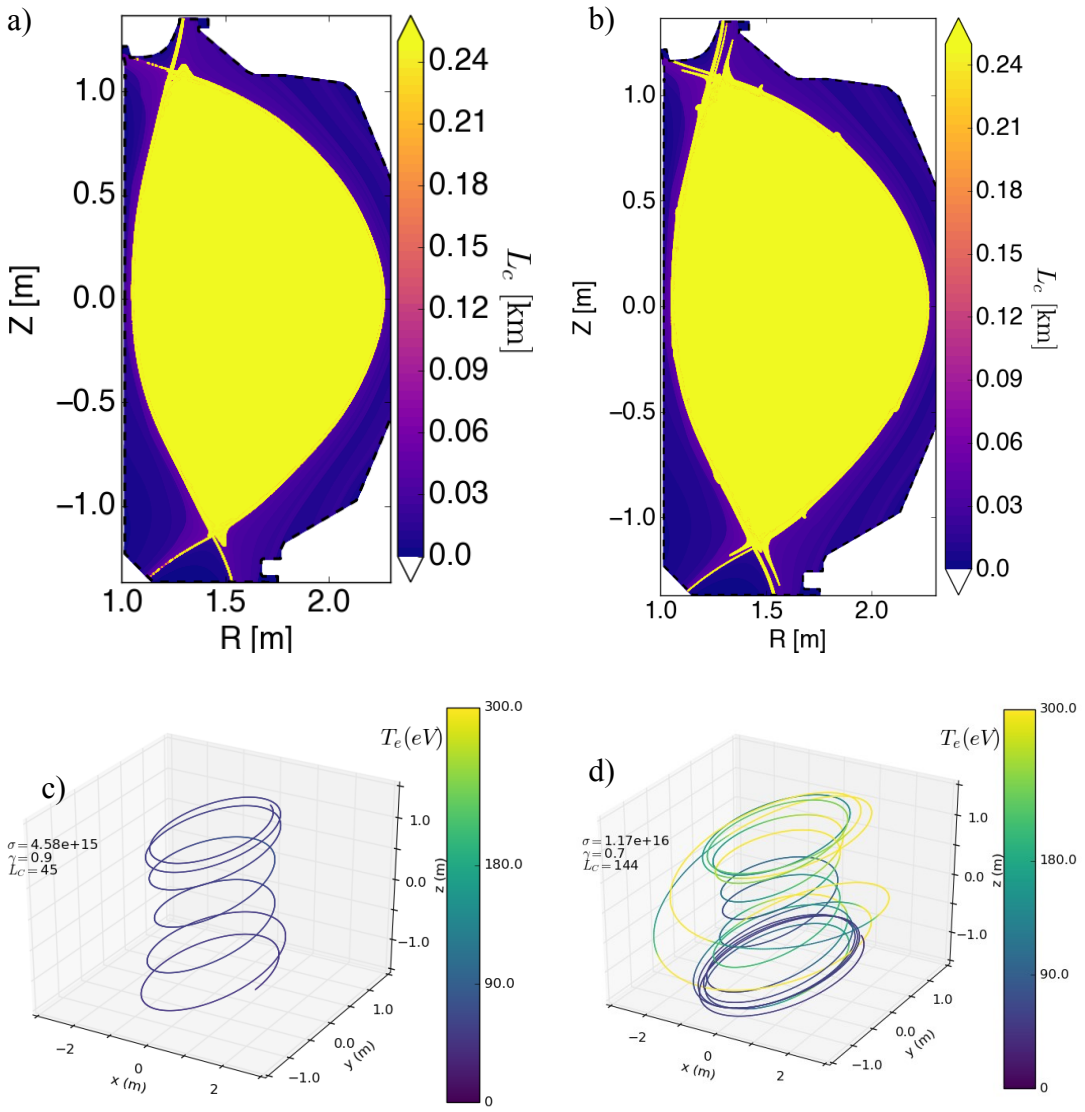

Figure 45 MAFOT connection length L_C calculation of discharge 119150 with a) error fields only b) two filaments with 200 A and 300 A: c) representative field line in the HFS near strike point SOL d) flux tube through the plasma connecting LFS and HFS

plasma assumptions as derived in chapter 5.4. Consequently, the ECM delivers a consistent model for the current origin and impact both in LSN and in DN shape that can explain the explosive nonlinear growth during ELMs. An open question in the ECM is, what exactly causes the current oscillations. A closer look at the oscillatory current phase shows, that there are not many current direction reversals on the tiles, i.e. sign changes of the measured current during the oscillation. For instance, in figure 29 there are a maximum of four reversals at the OSP 135° sensor, but the average is two reversals suggesting a comparatively slower process compared to the cause of the

oscillations itself. Here, several hypothetical oscillation contributors are listed and briefly discussed:

- instrumental effect
  As all tile current monitors are built using the same components, an instrumental effect would show up on all current measurements. Yet, as can be seen for currents near the ISP during the ELM shown in figure 29 while sensors as 10B115 and 10B150 display strong, low frequency oscillations with current reversal, others have very weak, high frequency oscillations (10B200) or long periods of low frequency oscillations without current reversal (10B000), ruling out instrument effects.
- currents generated by plasma movement
  During ELMs the plasma is moving and shifting causing balancing currents
- generation pattern of flux tubes
  as has been shown the self-amplifying mechanism of flux tube growth due to current flow through them will lead to new flux tubes which are distorted toroidally in the divertor. The net sum of currents measured on each tile could resemble the generation pattern of flux tubes as oscillations

To conclude, the analysis of tile currents in a DN shape shows convincingly that a current flow through the confined plasma during ELMs is necessary to explain the instantaneous current flow onset on HFS and LFS. These currents form the base of the ECM as driver for additional growth in the nonlinear phase. So far, the model is based on analysis of static plasma equilibria, whereas fully nonlinear ELM simulations with tile currents are necessary to analyze the dynamics of flux tube formation and destruction.

6. Discussion, summary and outlook

Edge-localized-modes pose a major challenge for future fusion power plants due to their pulsed heat loads on the divertor and plasma facing components. In the foreseen operational regime, the standard H-mode, the repetitive collapse of the plasma edge transport barrier is a ubiquitous phenomenon leading to considerable stored energy losses, albeit contributing to controlling plasma impurity content. Fast infrared cameras facilitate measurement and evaluation of these transient heat fluxes. Improved understanding of the nonlinear ELM phase and heat load scaling with plasma parameters is necessary for designing benign reactor operation scenarios and engineering ELM mitigation techniques. The contributions of this thesis consist of the evaluation of heat load scaling with plasma parameters on the DIII-D tokamak and the development of a model based on ELM currents explaining the origin of an additional driver of growth in the nonlinear phase of the instability.

6.1. Summary and conclusions

A nondimensional shot-by-shot collisionality scan has been carried out on the DIII-D tokamak to investigate the scaling of ELM heat loads with pedestal pressure and collisionality and test the Eich model for ELM energy densities. The dataset collected includes 27 time windows with well diagnosed ELM activity spanning a range from ν_e^*= 0.05 – 2.17 and $p_{e,ped}$ = 3.2 -7.8 kPa. The dataset has been extended to include other H-mode discharges with collisionalities up to 1.2. In general, for large ELMs between 40 % and 60 % of the ELM energy is deposited onto divertor tiles, with peak heat flux only slightly higher at the inner divertor than the outer (ratio in/out: 1.1 : 1). Bolometry measurements during ELM crashes are consistent with a large fraction of ELM energy (up to ~50%) being dissipated through radiation. Hence, the ELM energy balance suggests that the direct heat deposition on the main chamber wall is small in these cases. The main results of the experiment are briefly summarized here:

- As a whole, the measured ELM energy densities appear consistent with the prediction of Eich model. However, a clear correlation between the model prediction and experiment is not found. The measured $\varepsilon_{\parallel}$ covers the range between 0.5-2 times the predicted values.
- The nondimensional collisionality scan did not reveal an increase of $\varepsilon_{\parallel}$ with atl lower ν_e^*. On the contrary, for high collisionalities near the LH power threshold, the Eich model yielded predictions of $\varepsilon_{\parallel}$ values which significantly

underestimated the experimental values.

- The prediction of Eich's model are found to be more accurate when the heating power is much larger than the LH power threshold (> 2X). In particular, for the same pedestal pressure, much larger ELM energies are observed for low-frequency ELMs found for P_{heat}~P_{LH}. This suggest that, to improve the predictive capabilities in this regime, a model should account not only for the pedestal properties at ELM crash, but also for the dynamic evolution of the pedestal towards the ELM crash [162,163].

For the dataset in consideration, an inverse correlation is found between the peak parallel ELM energy density and the most unstable toroidal mode number calculated by linear MHD stability analysis. Considering the scaling $W_{ELM} \sim \frac{1}{\nu}$ derived in [12] through an extensive multi-machine analysis, this result suggests that lower collisionality would be correlated with lower toroidal mode numbers. This is intuitively acceptable, given that low collisionality generally results in low n peeling-ballooning modes, associated with higher bootstrap current. A clear correlation between collisionality and mode number did not emerge from the present dataset. It is interesting to investigate how the observations in the experiments can affect the projection to ITER, regarding the two models considered in this work: Eich's model (ELM energy density scales with $p_{e,ped}$) and Loarte's model (ELM energy scales with $1/\nu_e^*$). The predictions of the two models for ITER have been carried out in section 2, showing a small discrepancy in the non-active phase of ITER operation ($I_P = 7.5$ MA, $B_T = 2.65$ T), and being significantly different during the active phase ($I_P = 15$ MA, $B_T = 5.3$ T).
During the DIII-D experiments two observations were made which can raise concern for future ITER operation:

- First, for plasmas with P_{heat}~P_{LH} ELMs with W_{ELM}/W_{MHD} up to 14 % were robustly documented, which challenges the predictions of both Loarte and Eich's models. Since ITER will operate with P_{heat}>=P_{LH}, this suggests that the model predictions might not be accurate: First, the non-active phase of ITER operation is considered: assuming a magnetic field of 2.65 T, line-averaged density $\bar{n} = 0.8 \cdot 10^{20} \frac{1}{m^3}$ and a plasma surface area of 620 m^2 the projected L-H- threshold is P_{LH}=38 MW. In the optimistic scenario, P_{heat}= P_{OH}+P_{ICRH}+ P_{ECH}+P_{NBI}=73MW (assuming P_{NBI}=30 MW), results in P_{heat} ~ 1.9 P_{LH}. Assuming a plasma energy of 100 MJ for ITER's non-active phase, a 14 % ELM would be 3 times above the currently assumed 4 MJ for uncontrolled type-I ELMs in this phase [21].
- Second, it was shown that the ELM energy density inversely correlates with n_{max}, the toroidal mode number with highest growth rate computed from linear stability. ITER is predicted to operate on the peeling-branch due to its low collisionality where most unstable mode numbers can be single digits. If the

inverse scaling between n_{max} and $\varepsilon_{\parallel}$ is a general result, i.e. confirmed by experiments on other devices, it would provide a way to extrapolate the ELM energy densities from linear stability calculations of ITER operation equilibria.

The investigation of ELM heat load scaling emphasized the widespread need of a more thorough understanding of dynamics in the nonlinear ELM phase. For this purpose, the role of currents flowing into the divertor as potential driver of explosive growth during the instability was elucidated in this work. These ELM currents have been previously observed on mid-size and smaller tokamaks. Here, important new experimental findings will be summarized:

- At the ELM onset, there are divertor currents flowing into and out of tiles near the strike points, before the heat flux increase is measured by IR thermography. Currents of inner and outer strike points display opposite sign, reversing with a change of B_T direction.
- The current flow during ELMs consists of an initial oscillatory phase (<0.3 ms) with high frequency oscillations (5-67 kHz) and a subsequent bulk phase, characterized by large but steady currents
- Current flow is radially strongly localized near the strike points, however small currents are measured in the private flux region during ELMs
- Current peaks between 0.3-0.5 kA per tile are recorded, which amounts to 5 – 20 kA current in the ring. Sign and size of the currents agree with a thermoelectric nature and origin of the currents with the ion saturation current on the colder side as the upper limit
- While no consistent rotation pattern is found, Fourier analysis indicates a mix of low n modes (<3) within the measurement resolution in agreement with nonlinear peeling-ballooning theory
- Correlation between magnetic probes and TCA measurements exists for core modes in the inter-ELM phase and in form of wide frequency response during ELMs
- There is a weak correlation between peak current amplitude in the oscillatory phase near the strike points and ELM size

Thermo-currents during the inter-ELM and ELM phase of comparable size to DIII-D were also measured on AUG with a tile current array located at three toroidal positions [132,164]. The reversal of current flow with change of the $B \times \nabla B$ direction was pointed out on AUG [28]. Additionally, the same paper reports a proportionality between asymmetry of ELM energy deposition between inner and outer divertor and the exchanged charge (integral over the current flows between divertor legs, with both measured against ground). For reversed $B \times \nabla B$ drift direction the proportionality constant is twice as high, so double the charge is exchanged between divertor sides for a similar ELM size. A slight decrease in current amplitude was observed with $B \times \nabla B$ drift reversal in this work too, however the inter ELM amplitude has decreased as well:

Hence, this effect might be due to different plasma temperature conditions in front of the divertor consistent with reduced heat flux measurements in matching reversed B_T cases.
Based on these experimental findings and previous work a new model was developed elucidating the origin, role and effect of currents during ELMs. Potentially addressing mechanisms for additional nonlinear growth as sought for in large scale simulations the model describes the drive of explosive growth provided by currents and is hence named the ELM current model (ECM). While the measurements agree well with the predictions of the model it is at present still based on ad-hoc simulations. The successive stages of the ECM and the experimental findings or simulation results, which the stages are based upon are outlined in the following

- after exceeding the peeling-ballooning stability threshold, loss of energy and particles sets in at the pedestal; the electron heat pulses lead to a rise of plasma temperature in front of the divertor as measured by Langmuir probes on TCV
- thermoelectric currents flow from the hot divertor plasma to colder parts on the other divertor side through flux tubes in the confined plasma. The current size agrees well with calculations based on flux tube areas on the tiles predicted by the MAFOT code and a model for thermoelectric current flow along field lines developed by Staebler with the ion saturation current as upper limit.
- these flux tubes are produced by error fields and the ballooning mode at the plasma edge in a competing process causing different rotation patterns in the tile current array. In a self-amplifying mechanism, more and larger flux tubes are produced due to thermoelectric currents in the tubes. The growth in number and size of the flux tubes can be confirmed by MAFOT simulations and outcomes have been verified with comparisons of IR footprints. The current flow through the plasma edge also explains the high correlation between power spectral densities of TCA and magnetics.
- The increasing stochastization caused by current flow in the flux tubes facilitates access to deeper layers of the pedestal causing additional heat and particle transport
- when the pedestal has regained stability due to a nonlinear saturation mechanism and the arrival of ions in the divertor has balanced thermal gradients, the drive for the thermoelectric current ceases and the transition to the filamentary phase sets in with the pedestal recovery

While the tile current size is also consistent with SOL currents in vicinity of the separatrix, ELM current measurements in balanced DN scenarios cannot be explained by pure SOL currents: Simulation results of finite time (~40 Alfvén times) for the magnetic ELM perturbation to spread from LFS (where the outboard ballooning sets in first) to HFS disagree with the measured simultaneous onset of HFS and LFS currents. The ECM provides a mechanism for simultaneous current onset through flow in confined plasma flux tubes.

6.2. Future Work

The experimental results described in this work challenge the present-day models of ELM heat load scaling and strongly motivate further experimental and modeling research. Future work in this area should focus on ELM activity close to the LH threshold, with particular emphasis on the role of pedestal micro-instabilities in determining the pedestal evolution towards the ELM crash.
Furthermore, effort should be put in testing the relation between the most unstable linear mode number and ELM energy density, in other plasma conditions and other tokamaks. If confirmed and understood, the scaling could provide an effective tool to estimate the size of ELM events on present machines and ITER, without the need of challenging nonlinear MHD simulations. Two very important results in the ELM heat load scaling analysis concern the role of LH proximity and linear mode structure. A comparison to H-modes in other tokamaks will show, to what extent these results can be reproduced, and help to improve the knowledge of ELM physics. Since ITER will be operating in a low collisionality, close to LH threshold environment, these studies are urgently needed.
While the ELM current model presented in this thesis is consistent with experimental data, it is based on instantaneous field line tracing and current calculations. Remaining questions comprise of the influence of error fields on potential locking and the trigger mechanism: Can one detect changes in the ELM behavior by varying the size of the error fields and induce locking? Does the growth of the peeling ballooning mode itself contribute to the generation of current-carrying flux tubes? What role does the plasma response play in the cycle? Can the increase of stochasticity break up flux tubes? What is the exact saturation mechanism? In order to further understand the impact of the tile currents on transport and evolution of type I ELMs it is important to implement tile currents as boundary condition into nonlinear simulations such as JOREK. Quantitative modeling will also lead to a better understanding of how the flux tube resistance in deeper layers of the pedestal behaves given the strong dependence of conductivity on its temperature ($\sigma \sim T_e^{1.5}$). This way, the hypotheses of the ECM could be tested and in a second step, the effects of manipulating tile currents could be estimated. This is a major physics question unfolding into two directions:

- If using insulated tiles (that is not only against their neighbors but also against the torus and maybe only temporarily), can the characteristics of ELMs (e.g. currents in oscillatory phase) be affected and ultimately ELM mitigation be achieved as a potential stochasticity-enhancing mechanism is suppressed?
- Can tile biasing be used to drive significant helical current through the edge of the confined plasma to impact the ELM crash or general ELM behavior?

Theoretical considerations indicate the possibility to drive currents near the plasma edge in order to suppress ELMs [165]. Most of the previous bias experiments on mid-size tokamaks used axisymmetric setups in the form of a ring or symmetrically

distributed probes [166–168]. Given the results of current size and non-asymmetric distribution in this thesis, it is understood that the results seen were local and had no global effect on ELMs. An experiment to test manipulation of tile currents would have to be based on a non-axisymmetric setup to drive helical currents. The differences between DC biasing and feedback on magnetic activity on ELM crashes would have to be explored experimentally. In contrast to RMP ELM suppression, QH-mode plasmas or ELM pacing, that all come with operational constraints, using tile insulation or biasing – if successfully demonstrated - might offer a path to mitigation of ELM heat loads on the divertor independent of plasma conditions.

Appendix

A. DIII-D magnetic configuration

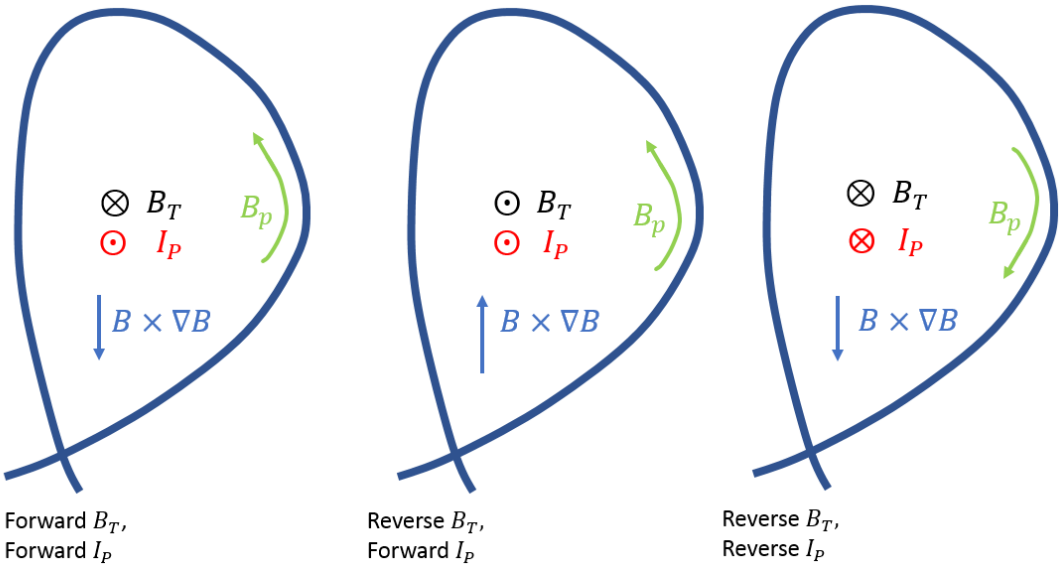

Figure 46 Overview of magnetic configurations of DIII-D analyzed in this thesis. Direction of I_P, B_T, B_p and the $B \times \nabla B$ drift. Favorable $B \times \nabla B$ drifts for the LH-transition point towards the divertor.

DIII-D is the worldwide only tokamak that can alter both magnetic field and plasma current direction, affecting the direction of the B × ∇B drift and poloidal field direction, respectively (figure 46). Hereby the L-H transition power threshold can be manipulated as well as drifts in the SOL. Since the injection direction with regards to the vessel is fixed for the majority of neutral beams, reversing the current will affect the amount of injectable power in the co- and counter I_P direction and consequently torque and rotation profiles. While the standard profile on DIII-D is forward B_T and I_P (left), QH modes for instance were initially started in a reversed I_P setup to obtain the necessary velocity shear at the plasma edge, before a way was found to provide the edge torque by the RMP coils [169].

B. Surface layers in the THEODOR code

Since surface layer assumptions can result in large corrections to the computed heat flux, determining the appropriate values is a crucial step in the IR analysis[170]. The importance of the surface layer parameter α_{surf} (equation 3.7) strongly depends on wall and divertor materials as they influence the amount of sputtering. This term describes the process of particle ejection from a solid target due to bombardment with energetic particles, i.e. ions and electrons entering from SOL or along strike lines in tokamaks. In tungsten machines sputtering and surface layer effects are negligible so α_{surf} can be set as infinite [171]. In machines with low-Z materials (as is DIII-D with its Carbon wall) sputtering yields are large and the surface layer effects need to be considered. To find the best parameter for α_{surf} an optimization was undertaken along three partially competitive objectives:

1. The energy balance during the ELMs and the discharge as a whole must be physical, i.e. there cannot be more energy in the divertor than injected by ohmic and external heating
2. At the end of the discharge, the energy in the divertor must remain constant as the total arriving power is zero.
3. The temporal shape of the deposited energy should resemble fast increases during ELMs and a slow rise in the inter ELM phases. The heat flux trace of each ELM should consist of a large initial spike, followed by a valley during which the pedestal is restored.

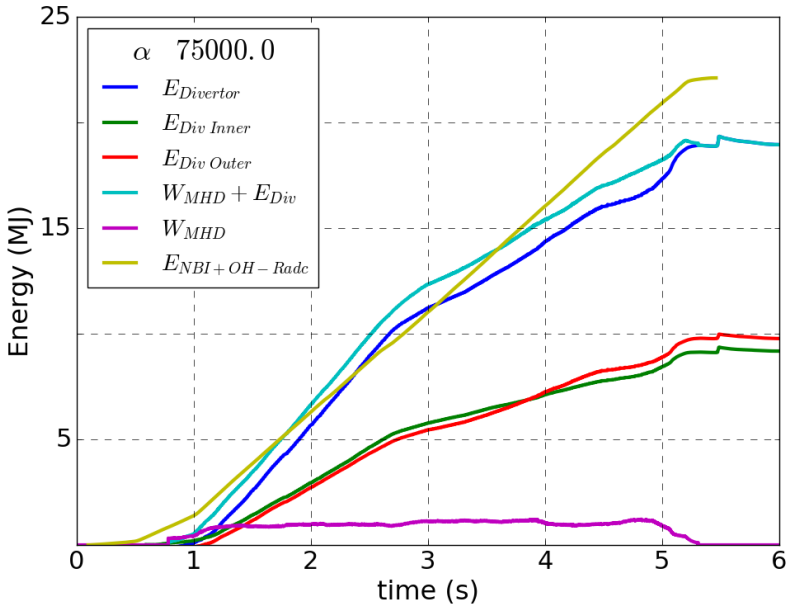

Figure 47 Energy balance of discharge 166022: Total heating, plasma and divertor energy (inner, outer and combined). The heating energy (yellow) is close to the sum of divertor and plasma energy (light blue) for this $\boldsymbol{\alpha_{surf} = 75000}$.

An example for an upper limit determined by discharge energy balance is shown in figure 47 with α_{surf}=75000[8]. This is discharge 166022 from a divertor recycling experiment with low type I ELM frequencies [172]. Throughout the discharge the net injected energy (consisting of external heating subtracted by plasma radiation) balances with the sum of plasma and total divertor energy. Due to non axisymmetry of heat flux deposition and radiation distribution and power flux to the wall an error bar of 20 % should be applied to both measurements. The energy balance during ELMs offers another gauge for α_{surf} (figure 48): unphysical divertor energies are obtained in this discharge for α_{surf} values above 300000. The x-axis represents the plasma energy loss W_{ELM} and the y-axis the total divertor energy. The two solid lines limit the expected range of 50 -100 % of the plasma energy loss W_{ELM}. A good solution is yielded for α_{surf}=75000.

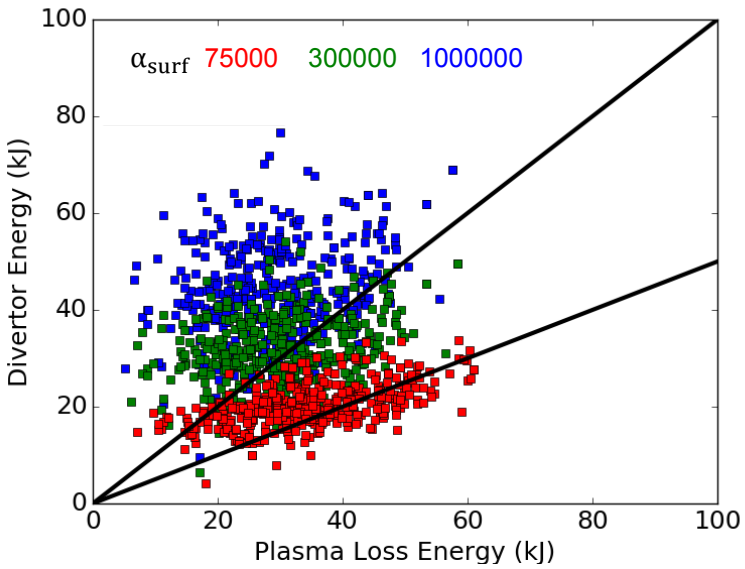

Figure 48 ELM energy balance for discharge 159720: Divertor energy vs plasma loss W_{ELM} for different values of surface layer parameter $\boldsymbol{\alpha_{surf}}$. The black solid lines limit the expected data area for the divertor energy (50-100 % of W_{ELM})

Regarding objective 2 - obtaining no net heat flux at the end of the discharge when the confined plasma has already ceased to exist - figure 49a illustrates the effect of feeding wrong surface layer parameters into THEODOR. In reality, the surface layers produce additional radiated energy causing a faster cooling of the divertor. Underestimating this effect with a too high α_{surf} (red trace) leads to a decrease in calculated energy as the faster cooling is interpreted as negative heat flux by the code. On the other hand, overestimation leads to an increase of energy, as the overestimated radiation power

[8] the unit of α_{surf} is W/m^2K but it is convention to refer to the surface layer value without the unit.

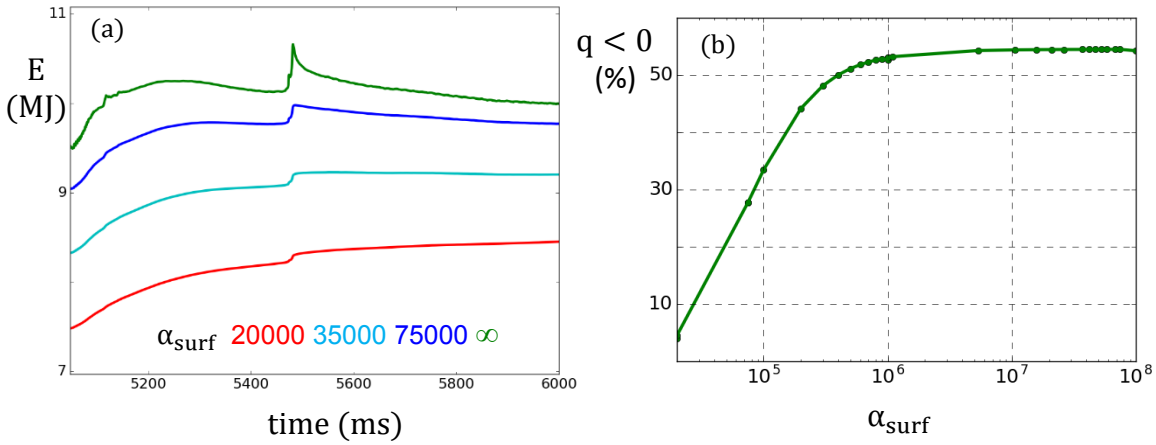

Figure 49 Impact of surface layers on heat fluxes for discharge 166022 a) IR energy trace at the end of discharge for different $\boldsymbol{\alpha_{surf}}$ values. The plasma terminates at 5.5s b) Percentage of negative heat fluxes in the IR data grid in dependence of $\boldsymbol{\alpha_{surf}}$

leads to a pseudo heat flux in THEODOR to match calculated and expected temperatures (blue trace). Hence the amount of negative heat fluxes is directly proportional to the value of α_{surf} (figure 49b). Ideally one would like to have little to no negative heat fluxes, unless these are unavoidable due to the IR noise level.
The effect of wrongly estimating surface layers on the temporal shape (objective 3) for ELMs is similar: Additional radiation from the surface particles are interpreted as heat flux spikes if the layers are underestimated, the improved conductivity and faster cooling as negative heat fluxes and vice versa.
For the discharges analyzed in this thesis, α_{surf}=75000 was determined to be the optimal value for meeting the objectives listed above. Consistent usability of this surface layer value supports the validity of experimental data. The impact of surface layers also depends on the material properties as can be seen in the heat diffusion equation 3.6. Hence, an overview of DIII-D divertor material properties used in the THEODOR calculation of this work is given in table 9 for reference.

Temp [°C]	**0**	**500**	**1000**
Diffusivity D [mm^2/s]	81	20	11
Conductivity κ [W/mK]	97	57	40
Thickness [cm]	5.28	5.28	5.28

Table 9 Summary of DIII-D divertor material properties used in the THEODOR at different temperatures

The diffusivity D is the ratio of conductivity and the product of specific heat capacity and density (equation 3.6)

$$D = \frac{\kappa}{\rho c_p} \tag{B.1}$$

IR codes with an implicit algorithm for determination of surface layer properties as ALICIA aim to reduce uncertainty imposed by manual choice of the α_{surf} parameter and are being tested on DIII-D [173].

C. Mode number derivation

In equation 5.1 V_{mod} takes the form of

$$V_{mod} = \begin{bmatrix} 1 & \sin A & \cos A & \dots & \sin nA & \cos nA \\ 1 & \sin B & \cos B & \dots & \sin nB & \cos nB \\ \dots & \dots & \dots & \dots & \dots & \dots \\ 1 & \sin E & \cos E & \dots & \sin nE & \cos nE \end{bmatrix} \quad \text{(C.1)}$$

Whereby A,.... E represent the angles in machine coordinates of the different TCA and n is the highest desired mode number for analysis. The V_{mod} dimensions are number of TCA x (2x maximum mode number+1). The tile current array is consequently represented as

$$\overrightarrow{I_{TCA}} = [I_A \; I_B \; \dots\dots \; I_E \quad] \quad \text{(C.2)}$$

The solution $\vec{S}$ of equation 5.1

$$\vec{S} = {V_{mod}}^{-1} \cdot \overrightarrow{I_{TCA}} \quad \text{(C.3)}$$

is then found using a matrix solver. Its length is $j = 2n_{max} + 1$ with n_{max} the highest resolved mode number and it is split in the various mode contributions.

$$\overrightarrow{S_{reconstr}} = \begin{bmatrix} 1 \\ S[1] + iS\,[2] \\ \dots \\ S[j-2] + iS\,[j-1] \end{bmatrix} \quad \text{(C.4)}$$

out of which then amplitude and phase of the various modes can be extracted by known methods. The change of the phase over time indicates the rotation of the mode.

Acknowledgements

One's life has value so long as one attributes value to the life of others, by means of love, friendship, indignation and compassion.

Simone de Beauvoir

Throughout the journey of this PhD I felt inspired, motivated and supported by a large number of people. Especially when facing challenges their help contributed to the success of this work.

First of all, I could always rely on academic supervision and guidance of Professor Hartmut Zohm. Hartmut, your ability to understand and illuminate the most complicated physics never ceased to amaze me, and yet you are able to see the joy of life beyond research and treat everyone with respect and genuine kindness. This is a very rare combination. Similarly, while you granted me large independence and freedom for my research, it felt good to me to know you in my corner whenever I needed help or advice.

The freedom in research brought many advisors, who I owe a lot. In chronology, I have started with Dr. Raffi Nazikian and Dr. Tony Leonard on pedestal stability and divertor physics, then Dr. Alessandro Bortolon on ELM heat loads and finally Dr. Todd Evans and Professor Rick Moyer on ELM divertor currents. Raffi, you have taught me about inspiring leadership and the need for pragmatism in decision making. I admire your dedication and your ability to get things done. You were willing to pay the Princeton tuition for me, which I will not forget. Tony, you possess a tremendous knowledge in multiple physics areas and you have always taken time for a discussion and helpful advice. Alessandro, you taught me how to write papers accurately down to selecting the proper word. I thank you for all the time you have invested in correcting my drafts and making suggestions. Todd, the part of this thesis I am most proud of was inspired by you. When I walked into your door first, asking you to explain some details of your model to me I did not expect that one of the most accomplished plasma physicists could also be the most modest and kindest. For about one year I have been in your office almost every day to discuss ELM currents and fusion research and I learned so much words can’t do it justice. Rick, without you helping me on my visa issues, this PhD would have been in serious trouble. Beyond your rich physics knowledge, I highly enjoyed all discussions with you on science management and politics.

There are multiple people who I am deeply indebted to as they helped me in decisive parts of the thesis work or who I suspect always did so in the background but never told me: Dr. Richard Buttery for getting my PhD on track and giving constant advice throughout, Dr. Rich Groebner for meticulous and thorough reviews and his genuine kindness and humbleness, Dr. Brian Grierson for creating clear work flows and time management (and offering quick fixes), Dr. Craig Petty, Dr. Carlos Paz-Soldan (for saving the experiment as physics operator), Dr. Max Fenstermacher, Dr. Dave Hill, Dr. Wayne Solomon, Dr. Philipp Snyder and Lupe Cerda for being a total sun shine.
I admire your visions for the DIII-D program and the enthusiasm with which you drive them and set the climate of performance in a familiarly environment.

For supporting me in learning the ELITE, OMFIT and the MAFOT code I am indebted to Professor Gustavo Canal, Dr. Thomas Osborne, Dr. Orso Meneghini, Dr. Sterling Smith and Dr. Andreas Wingen. I thank all of you for taking the time to guide me and point out the errors in my code, even though you often had more pressing research issues to dedicate your time to. For their help with infrared data and hardware I owe tremendous gratitude to Dr. Mike Makowski and Dr. Charles Lasnier. While I am grateful to all diagnosticians facilitating these experimental studies, Dr. Eric Hollmann Dr. Jon Watson and Dr. Colin Chrystal went out of their way to obtain critical data for me.

For great discussions about physics, politics and beyond I would like to thank Dr. Andrea Garofalo, Dr. George McKee, Dr. Brent Covele, Dr. Brendan Lyons, Dr. Robert Wilcox, Dr. Arash Ashourvan, Dr. Auna Moser, Dr. Florian Laggner, Dr. Morgan Schafer and Dr. Dan Thomas. My evening workout sessions were infused with humor and enriched by life and business advice through Linden and Paul, with no locker room talk at all.

As studying physics does not answer questions of our existential human nature, I am glad to have found some people who were willing to join for the occasional drink. Alex and Lisa – my favorite couple of the world– thank you for all the great times and your thoughts on academia and life. Exploring Princeton together with you was one of the happiest years of my life, infused and provided by your kind-heartedness and social intuition (Lisa), curiosity and philosophy (Alex). That year would be unthinkable without you, Andrea, who kept humoring and challenging me throughout the PhD: Whatever you set your mind to, you don't lose focus until you excel, as if it were an art. Evan, my best drinking buddy, thanks for hanging out with me in Barelymash and little Italy while enriching my life with your bojackian stories. Despite your intelligence you never lost touch to the ground and you always assume the best of your friends. When you were supposed to help carrying my freshly bought couch and I caught you sitting on it right on the sidewalk in downtown while sipping a drink by yourself like Steven Glansberg, I knew you were in for the long haul. For all the great times in San Diegan bars, concerts or apartment party's I am beyond grateful for Theresa, Tyler, Jeremy and Mike. You followed so many of my rather spontaneous invitations, you

were awesome hosts yourself and made me laugh throughout the PhD. Fredi, you are one of the funniest people and the only of my friends who fathered twins, thanks for the great road trips and discussions on the stock market and raising children, showing me the worlds beyond physics. Speaking of friends with a big heart, I would also like to say thanks to Chris who while busy impressing doctors at Stanford always loyally kept in touch and visited, so I never felt like he left. I am very proud of your accomplishments and will not forget the legendary days of Schwabing. This is also where I reunited with another good friend, whose life was strangely intertwined with mine - from the military service to the frat life: Erol, I have always admired your honesty and integrity. Thanks for your encouragement throughout my PhD and never getting tired of walking down memory lane with me. The common admiration for Thomas Bernhard and Charles Bukowski has been a theme throughout the PhD connecting me and Bernd, whose perspicacity and loyalty is unmet. I almost fell off my chair when reading your emails advising me on life issues; no surprise the Bavarian ministers rely on you for their speeches. For their patience with my spontaneous scheduling or late-night phone calls, their kindness and candor (even though I spent most of the year on the other side of the globe) I will keep the time with you, Fabian, Patrick and Reemi in treasured memory.

As they say, ‘behind every great man there is a great woman’: In my case, it took three women to get me through this PhD. The reason for mentioning only one bar in the paragraph above – which you, the interested reader will have noticed – is because I met Kara, at that very place. Kara, you have enriched my life with your happiness, management skills and total support however crazy you thought my ideas were (some of them, I will admit with the gift of hindsight might have actually been wild). I am proud of your job accomplishments and also of your knowledge of all TV shows. I owe at least one stipend to the help of you, Feodora. You pushed me and supported me unconditionally. From the stimulating discussions to the downtown celebrations, your intelligence and adeptness are intriguing. In an unlikely succession of events I was fortunate to meet you, Cady, my ethereal muse. You have a different way of looking at the world than most of us and I thank you for sharing it. From trying to find gluten free food in Stresa to spending the so-called literature week in Palm Desert without a single read: there was not a dull moment in life at your side.

While the three years of this PhD were challenging at times, I had the strongest support from my family. So, I would like to thank my mum, for humorizing me throughout the PhD and my dad for sharing his approaches on handling work trouble. Both my parents have always valued achievement and have done the utmost possible financially and time-wise to get me and my sisters where we are today. In particular I am grateful for your visit and our trip to Vegas, with mum totally enjoying the music of J. Cash while on the trip and dad sharing his gambling philosophy. If I only am half as good a parent as they, I will have done well. I am very grateful to my sister Susanne for her compassionate support and hosting in Regensburg. Stay as funny and woke as you are satirizing Saturn’s position as a largely underestimated influence on people’s weight

while impressing us on your way to becoming a real doctor. A big shout-out also goes to my sister Elena. Parallel to studying the law and communication science you were there when our parents needed help. I want to thank you for your empathetic companionship and your insightful advice throughout the PhD. You seek truth and not righteousness, which impressed me so often along my way as if I were learning from you. Both of you have both grown up to be independent and strong women, and I am so unspeakably proud of you.

In the attentive and aware moments throughout this PhD I could feel the gentle whisper. And so, I will conclude these acknowledgements in deep awe and gratitude:

Glory be to the Father
and to the Son
and to the Holy Spirit.
As it was in the beginning
is now,
and ever shall be,
world without end.
Amen.

Bibliography

[1] Kardashev N S 1964 Transmission of Information by Extraterrestrial Civilizations *Sov. Astron.* **8** 217–21

[2] Huba J D 2013 NRL PLASMA FORMULARY Supported by The Office of Naval Research *Plasma Phys.*

[3] Irving Langmuir Researchlaboratory B, EIXCTRIc Co G and NsCTADY S 1928 OSCILLA TI&NS IN IONIZED GASES *Nat. Phys. Rev. Naturwiss. Bethe, Ibid. Andrewes Proc. Roy. Soc* **14** 317–705

[4] Spong D A, Heidbrink W W, Paz-Soldan C, Du X D, Thome K E, Van Zeeland M A, Collins C, Lvovskiy A, Moyer R A, Austin M E, Brennan D P, Liu C, Jaeger E F and Lau C 2018 First Direct Observation of Runaway-Electron-Driven Whistler Waves in Tokamaks *Phys. Rev. Lett.* **120**

[5] Lawson J D 1955 Some Criteria for a Useful Thermonuclear Reactor *Publ. Culham, United Kingdom At. Energy* 1–12

[6] (LLNL) T C S 1981 *Summary of Results from the Tandem Mirror Experiment (TMX)*

[7] Spitzer L 1981 The Stellarator Concept *IEEE Trans. Plasma Sci.* **9** 130–41

[8] Rutherford P 1980 The tokamak: 1955–80 *Nucl. Fusion* **20** 1086–92

[9] Shimomura R A and P B and Y 2002 <The ITER design.pdf> *Plasma Phys. Control. Fusion* **44** 519

[10] Smirnov V P 2010 Tokamak foundation in USSR/Russia 1950-1990 *Nucl. Fusion* **50**

[11] Peacock N J, Robinson D C, Forrest M J, Wilcock P D and Sannikov V V. 1969 Measurement of the electron temperature by Thomson scattering in Tokamak T3 *Nature*

[12] Pedersen T S, Otte M, Lazerson S, Helander P, Bozhenkov S, Biedermann C, Klinger T, Wolf R C, Bosch H S, Abramovic I, Äkäslompolo S, Aleynikov P, Aleynikova K, Ali A, Alonso A, Anda G, Andreeva T, Ascasibar E, Baldzuhn J, Banduch M, Barbui T, Beidler C, Benndorf A, Beurskens M, Biel W, Birus D, Blackwell B, Blanco E, Blatzheim M, Bluhm T, Böckenhoff D, Bolgert P, Borchardt M, Böttger L G, Brakel R, Brandt C, Bräuer T, Braune H, Burhenn R, Buttenschön B, Bykov V, Calvo I, Cappa A, Carls A, De Carvalho B B, Castejon F, Cianciosa M, Cole M, Costea S, Cseh G, Czarnecka A, Molin A Da, De La Cal E, De La Pena A, Degenkolbe S, Dhard C P, Dinklage A, Dostal M, Drevlak M, Drewelow P, Drews P, Dudek A, Durodie F, Dzikowicka A, Von Eeten P, Effenberg F, Endler M, Erckmann V, Estrada T, Fahrenkamp N, Fellinger J, Feng Y, Figacz W, Ford O, Fornal T, Frerichs H, Fuchert G, Garcia-Munoz M, Geiger B, Geiger J, Gierse N, Gogoleva A, Goncalves B, Gradic D, Grahl M, Groß S, Grote H, Grulke O, Guerard C, Haas M, Harris J, Hartfuß H J, Hartmann D, Hathiramani D, Hein B, Heirnich S, Henneberg S, Hennig C, et al 2016 Confirmation of the topology of the Wendelstein 7-X magnetic field to better than 1:100,000 *Nat. Commun.*

[13] Wolf R C, Ali A, Alonso A, Baldzuhn J, Beidler C, Beurskens M, Biedermann C, Bosch H S, Bozhenkov S, Brakel R, Dinklage A, Feng Y, Fuchert G, Geiger J, Grulke O, Helander P, Hirsch M, Höfel U, Jakubowski M, Knauer J, Kocsis G, König R, Kornejew P, Kràmer-Flecken A, Krychowiak M, Landreman M, Langenberg A, Laqua H P, Lazerson S, Maaßberg H, Marsen S, Marushchenko M, Moseev D, Niemann H, Pablant N, Pasch E, Rahbarnia K, Schlisio G, Stange T, Sunn Pedersen T, Svensson J, Szepesi T, Trimino Mora H, Turkin Y, Wauters T, Weir G, Wenzel U, Windisch T, Wurden G, Zhang D, Abramovic I, Äkàslompolo S, Aleynikov P, Aleynikova K, Alzbutas R, Anda G, Andreeva T, Ascasibar E, Assmann J, Baek S G, Banduch M, Barbui T, Barlak M, Baumann K, Behr W, Benndorf A, Bertuch O, Biel W, Birus D, Blackwell B, Blanco E, Blatzheim M, Bluhm T, Böckenhoff D, Bolgert P, Borchardt M, Borsuk V, Boscary J, Böttger L G, Brand H, Brandt C, Bràuer T, Braune H, Brezinsek S, Brunner K J, Brünner B, Burhenn R, Buttenschön B, Bykov V, Calvo I, Cannas B, Cappa A, Carls A, Carraro L, Carvalho B, Castejon F, Charl A, Chernyshev F, et al 2017 Major results from the first plasma campaign of the Wendelstein 7-X stellarator *Nucl. Fusion*

[14] Stix T H 1972 Heating of toroidal plasmas by neutral injection *Plasma Phys.*

[15] Litvak A G, Permitin G V., Suvorov E V. and Frajman A A 1977 Electron-cyclotron heating of plasma in toroidal systems *Nucl. Fusion*

[16] Jacquinot J 1999 Deuterium-tritium operation in magnetic confinement experiments: Results and underlying physics *Plasma Phys. Control. Fusion* **41**

[17] Wagner F, Becker G, Behringer K, Campbell D, Eberhagen A, Engelhardt W, Fussmann G, Gehre O, Gernhardt J, Gierke G V., Haas G, Huang M, Karger F, Keilhacker M, KÏber O, Kornherr M, Lackner K, Lisitano G, Lister G G, Mayer H M, Meisel D, MÏller E R, Murmann H, Niedermeyer H, Poschenrieder W, Rapp H, Röhr H, Schneider F, Siller G, Speth E, Stäbler A, Steuer K H, Venus G, Vollmer O and Ÿ Z 1982 Regime of improved confinement and high beta in neutral-beam-heated divertor discharges of the ASDEX tokamak *Phys. Rev. Lett.* **49** 1408–12

[18] Zohm H 1996 Edge localized modes (ELMs) *Plasma Phys. Control. Fusion* **38** 105–28

[19] Leonard A W 2014 Edge-localized-modes in tokamaks *Phys. Plasmas* **21**

[20] Jackson G L, Winter J, Taylor T S, Greenfield C M, Burrell K H, Carlstrom T N, DeBoo J C, Doyle E J, Groebner R J, Lao L L, Rettig C, Schissel D P and Strait E J 1992 Very high confinement discharges in DIII-D after boronization *Phys. Fluids B* **4** 2181–8

[21] Loarte A, Huijsmans G, Futatani S, Baylor L R, Evans T E, Orlov D M, Schmitz O, Becoulet M, Cahyna P, Gribov Y, Kavin A, Sashala Naik A, Campbell D J, Casper T, Daly E, Frerichs H, Kischner A, Laengner R, Lisgo S, Pitts R A, Saibene G and Wingen A 2014 Progress on the application of ELM control schemes to ITER scenarios from the non-active phase to DT operation *Nucl. Fusion* **54**

[22] Evans T E, Moyer R A, Burrell K H, Fenstermacher M E, Joseph I, Leonard A W, Osborne T H, Porter G D, Schaffer M J, Snyder P B, Thomas P R, Watkins J G and West W P 2006 Edge stability and transport control with resonant magnetic perturbations in collisionless tokamak plasmas *Nat. Phys.*

[23] Evans T E, Moyer R A, Thomas P R, Watkins J G, Osborne T H, Boedo J A, Doyle E J, Fenstermacher M E, Finken K H, Groebner R J, Groth M, Harris J H, La Haye R J, Lasnier C J, Masuzaki S, Ohyabu N, Pretty D G, Rhodes T L, Reimerdes H, Rudakov D L, Schaffer M J, Wang G and Zeng L 2004 Suppression of large edge-localized modes in high-confinement DIII-D plasmas with a stochastic magnetic boundary *Phys. Rev. Lett.* **92**

[24] Lang P T, Conway G D, Eich T, Fattorini L, Gruber O, Günter S, Horton L D, Kalvin S, Kallenbach A, Kaufmann M, Kocsis G, Lorenz A, Manso M E, Maraschek M, Mertens V, Neuhauser J, Nunes I, Schneider W, Suttrop W and Urano H 2004 ELM pace making and mitigation by pellet injection in ASDEX upgrade *Nucl. Fusion* **44** 665–77

[25] Burrell K H, Garofalo A M, Solomon W M, Fenstermacher M E, Osborne T H, Park J-K, Schaffer M J and Snyder P B 2012 Reactor-relevant quiescent H-mode operation using torque from non-axisymmetric, non-resonant magnetic fields *Phys. Plasmas* **19** 056117

[26] Moyer R A, Paz-Soldan C, Nazikian R, Orlov D M, Ferraro N M, Grierson B A, Knölker M, Lyons B C, McKee G R, Osborne T H, Rhodes T L, Meneghini O, Smith S, Evans T E, Fenstermacher M E, Groebner R J, Hanson J M, La Haye R J, Luce T C, Mordijck S, Solomon W M, Turco F, Yan Z and Zeng L 2017 Validation of the model for ELM suppression with 3D magnetic fields using low torque ITER baseline scenario discharges in DIII-D *Phys. Plasmas* **24**

[27] Fenstermacher M E, Leonard A W, Snyder P B, Boedo J A, Brooks N H, Colchin R J, Gray D S, Groebner R J, Groth M, Hollmann E M, Lasnier C J, Osborne T H, Petrie T W, Rudakov D L, Takahashi H, Watkins J G and Zeng L 2003 ELM particle and energy transport in the SOL and divertor of DIII-D *Plasma Phys. Control. Fusion* **45** 1597–626

[28] Eich T, Kallenbach A, Pitts R A, Jachmich S, Fuchs J C, Herrmann A and Neuhauser J 2007 Divertor power deposition and target current asymmetries during type-I ELMs in ASDEX Upgrade and JET *J. Nucl. Mater.* **363–365** 989–93

[29] Alfvén H 1942 Existence of electromagnetic-hydrodynamic waves [7] *Nature* **150** 405–6

[30] Freidberg J 2014 *Ideal MHD* vol 9781107006

[31] Wesson J 2004 *Tokamaks*

[32] Zohm H 2015 *Magnetohydrodynamic Stability of Tokamaks*

[33] Shafranov V D 1963 Equilibrium of a toroidal plasma in a magnetic field *J. Nucl. Energy. Part C, Plasma Physics, Accel. Thermonucl. Res.* **5** 251–8

[34] Grad H and Rubin H 1958 Hydromagnetic equilibria and force-free fields *J. Nucl. Energy* **386** 190–7

[35] Lao L L, John H S, Stambaugh R D, Kellman A G and Pfeiffer W 1985 Reconstruction of current profile parameters and plasma shapes in tokamaks *Nucl. Fusion* **25** 1611–22

[36] Mc Carthy P J, Horton L, Kallenbach A and Kurzan B 2003 ELM-resolved interpretive MHD equilibria on ASDEX Upgrade using SOL tile currents and kinetic data *St. Petersbg.* **27** 7–11

[37] Troyon F, Gruber R, Saurenmann H, Semenzato S and Succi S 1984 MHD-limits to plasma confinement *Plasma Phys. Control. Fusion*

[38] Greenwald M 2002 Density limits in toroidal plasmas *Plasma Phys. Control. Fusion*

[39] Luce T C 2017 A simplified analytic form for generation of axisymmetric plasma boundaries *Plasma Phys. Control. Fusion* **59**
[40] Luce T C 2013 An analytic functional form for characterization and generation of axisymmetric plasma boundaries *Plasma Phys. Control. Fusion* **55** 095009
[41] Hirshman S P and Whitson J C 1983 Steepest-descent moment method for three-dimensional magnetohydrodynamic equilibria *Phys. Fluids*
[42] Iter Physics Basis Editors, Iter Physics Expert Group Chairs Co-Chairs, Iter Joint Central Team Physics Integration Unit, Editors I P B, Chairs I P E G, Co C, Team I J C and Physics Integration U 1999 Chapter 1: Overview and summary *Nucl. Fusion* **39** 2137
[43] Burrell K H, Carlstrom T N, Doyle E J, Finkenthal D, Gohil P, Groebner R J, Hillis D L, Kim J, Matsumoto H, Moyer R A, Osborne T H, Rettig C L, Peebles W A, Rhodes T L, StJohn H, Stambaugh R D, Wade M R and Watkins J G 1992 Physics of the L-mode to H-mode transition in tokamaks *Plasma Phys. Control. Fusion*
[44] Burrell K H 1997 Effects of E×B velocity shear and magnetic shear on turbulence and transport in magnetic confinement devices *Phys. Plasmas*
[45] Biglari H, Diamond P H and Terry P W 1990 Influence of sheared poloidal rotation on edge turbulence *Phys. Fluids B*
[46] Manz P, Ramisch M and Stroth U 2009 Physical mechanism behind zonal-flow generation in drift-wave turbulence *Phys. Rev. Lett.*
[47] Schmitz L, Zeng L, Rhodes T L, Hillesheim J C, Doyle E J, Groebner R J, Peebles W A, Burrell K H and Wang G 2012 Role of zonal flow predator-prey oscillations in triggering the transition to H-mode confinement *Phys. Rev. Lett.*
[48] Ryter F, Angioni C, Beurskens M, Cirant S, Hoang G T, Hogeweij G M D, Imbeaux F, Jacchia A, Mantica P, Suttrop W and Tardini G 2001 Experimental studies of electron transport *Plasma Phys. Control. Fusion* **43**
[49] Snyder P B, Wilson H R, Ferron J R, Lao L L, Leonard A W, Osborne T H, Turnbull A D, Mossessian D, Murakami M and Xu X Q 2002 Edge localized modes and the pedestal: A model based on coupled peeling-ballooning modes *Physics of Plasmas* vol 9 pp 2037–43
[50] Groebner R J, Baker D R, Burrell K H, Carlstrom T N, Ferron J R, Gohil P, Lao L L, Osborne T H, Thomas D M, West W P, Boedo J A, Moyer R A, McKee G R, Deranian R D, Doyle E J, Rettig C L, Rhodes T L and Rost J C 2001 Progress in quantifying the edge physics of the H mode regime in DIII-D *Nucl. Fusion* **41** 1789–802
[51] Sauter O, Angioni C and Lin-Liu Y R 1999 Neoclassical conductivity and bootstrap current formulas for general axisymmetric equilibria and arbitrary collisionality regime *Phys. Plasmas* **6** 2834–9
[52] Zarnstorff M C and Prager S C 1984 Experimental observation of neoclassical currents in a plasma *Phys. Rev. Lett.* **53** 454–7
[53] Belli E A and Candy J 2008 Kinetic calculation of neoclassical transport including self-consistent electron and impurity dynamics *Plasma Phys. Control. Fusion* **50**
[54] Dunne M G and G. M 2013 Inter-ELM evolution of the edge current density profile on the ASDEX upgrade tokamak
[55] Taylor T S, St. John H, Turnbull A D, Lin-Liu V R, Burrell K H, Chan V, Chu M S, Ferron J R, Lao L L, La Haye R J, Lazarus E A, Miller R L, Politzer P A, Schissel D P and Strait E J 1994 Optimized profiles for improved confinement and stability in the DIII-D tokamak *Plasma Phys. Control. Fusion* **36**

[56] Hawryluk R J 1981 AN EMPIRICAL APPROACH TO TOKAMAK TRANSPORT *Physics of Plasmas Close to Thermonuclear Conditions* pp 19–46
[57] Pankin A, McCune D, Andre R, Bateman G and Kritz A 2004 The tokamak Monte Carlo fast ion module NUBEAM in the national transport code collaboration library *Comput. Phys. Commun.* **159** 157–84
[58] Wagner F 2007 A quarter-century of H-mode studies *Plasma Physics and Controlled Fusion* vol 49
[59] Chang C S, Ku S, Tynan G R, Hager R, Churchill R M, Cziegler I, Greenwald M, Hubbard A E and Hughes J W 2017 Fast Low-to-High Confinement Mode Bifurcation Dynamics in a Tokamak Edge Plasma Gyrokinetic Simulation *Phys. Rev. Lett.* **118**
[60] Martin Y R and Takizuka T 2008 Power requirement for accessing the H-mode in ITER *J. Phys. Conf. Ser.* **123**
[61] Gohil P, Evans T E, Fenstermacher M E, Ferron J R, Osborne T H, Park J M, Schmitz O, Scoville J T and Unterberg E A 2011 L-H transition studies on DIII-D to determine H-mode access for operational scenarios in ITER *Nucl. Fusion*
[62] Herrmann A 2002 Overview on stationary and transient divertor heat loads *Plasma Physics and Controlled Fusion* vol 44 pp 883–903
[63] Wade M R, Burrell K H, Leonard A W, Osborne T H and Snyder P B 2005 Edge-localized-mode-induced transport of impurity density, energy, and momentum *Phys. Rev. Lett.*
[64] Colchin R J, Hillis D L, Maingi R, Klepper C C and Brooks N H 2003 The filterscope *Review of Scientific Instruments*
[65] Connor J W 1998 A review of models for ELMs *Plasma Phys. Control. Fusion* **40** 191–213
[66] Miller R L, Chu M S, Greene J M, Lin-Liu Y R and Waltz R E 1998 Noncircular, finite aspect ratio, local equilibrium model *Phys. Plasmas* **5** 973–8
[67] Lortz D 1975 The General "Peeling" Instability *Nucl. Fusion* **15** 49–54
[68] Wesson J A 1978 Hydromagnetic stability of tokamaks *Nucl. Fusion* **18** 87–132
[69] Cooper A 1992 Variational formulation of the linear MHD stability of 3D plasmas with noninteracting hot electrons *Plasma Phys. Control. Fusion* **34** 1011–36
[70] Hegna C C 1998 The physics of neoclassical magnetohydrodynamic tearing modes *Phys. Plasmas* **5** 1767
[71] Hegna C C 1996 Nonlinear tearing mode interactions and mode locking in reversed-field pinches *Phys. Plasmas* **3** 4646–57
[72] Greene J M and Chance M S 1981 The second region of stability against ballooning modes *Nucl. Fusion*
[73] Osborne T H, Ferron J R, Groebner R J, Lao L L, Leonard A W, Mahdavi M A, Maingi R, Miller R L, Turnbull A D, Wade M and Watkins J 2000 The effect of plasma shape on H-mode pedestal characteristics on DIII-D *Plasma Phys. Control. Fusion* **42**
[74] Huysmans G T A and Czarny O 2007 MHD stability in X-point geometry: Simulation of ELMs *Nuclear Fusion* vol 47 pp 659–66
[75] Park W, Belova E V., Fu G Y, Tang X Z, Strauss H R and Sugiyama L E 1999 Plasma simulation studies using multilevel physics models *Phys. Plasmas* **6** 1796–803

[76] Snyder P B, Wilson H R and Xu X Q 2005 Progress in the peeling-ballooning model of edge localized modes: Numerical studies of nonlinear dynamics *Physics of Plasmas* vol 12 pp 1–7

[77] Krebs I, Hölzl M, Lackner K and Günter S 2013 Nonlinear excitation of low-n harmonics in reduced magnetohydrodynamic simulations of edge-localized modes *Phys. Plasmas* **20** 082506

[78] Pamela S, Eich T, Frassinetti L, Sieglin B, Saarelma S, Huijsmans G, Hoelzl M, Becoulet M, Orain F, Devaux S, Chapman I, Lupelli I, Solano E and Contributors J E T 2015 Non-linear MHD simulations of ELMs in JET and quantitative comparisons to experiments *Plasma Phys. Control. Fusion* **58**

[79] Pamela S J P, Huijsmans G T A, Eich T, Saarelma S, Lupelli I, Maggi C F, Giroud C, Chapman I T, Smith S F, Frassinetti L, Becoulet M, Hoelzl M, Orain F and Futatani S 2017 Recent progress in the quantitative validation of JOREK simulations of ELMs in JET *Nucl. Fusion* **57**

[80] Loarte A, Bosch S, Chankin A, Clement S, Herrmann A, Hill D, Itami K, Lingertat J, Lipschultz B, McCormick K, Monk R, Porter G D, Shimada M and Sugihara M 1999 Multi-machine scaling of the divertor peak heat flux and width for L-mode and H-mode discharges *J. Nucl. Mater.* **266** 587–92

[81] Stangeby P C 2000 Tutorial on some basic aspects of divertor physics *Plasma Phys. Control. Fusion* **42**

[82] Linke J, Loewenhoff T, Massaut V, Pintsuk G, Ritz G, Rödig M, Schmidt A, Thomser C, Uytdenhouwen I, Vasechko V and Wirtz M 2011 Performance of different tungsten grades under transient thermal loads *Nucl. Fusion* **51**

[83] Leonard A W, Groebner R J, Mahdavi M A, Osborne T H, Fenstermacher M E, Lasnier C J and Petrie T W 2002 ELM energy scaling in DIII-D *Plasma Physics and Controlled Fusion* vol 44 pp 945–54

[84] Loarte A, Lipschultz B, Kukushkin A S, Matthews G F, Stangeby P C, Asakura N, Counsell G F, Federici G, Kallenbach A, Krieger K, Mahdavi A, Philipps V, Reiter D, Roth J, Strachan J, Whyte D, Doerner R, Eich T, Fundamenski W, Herrmann A, Fenstermacher M, Ghendrih P, Groth M, Kirschner A, Konoshima S, Labombard B, Lang P, Leonard A W, Monier-Garbet P, Neu R, Pacher H, Pegourie B, Pitts R A, Takamura S, Terry J and Tsitrone E 2007 Chapter 4: Power and particle control *Nucl. Fusion* **47**

[85] Pitts R A, Andrew P, Arnoux G, Eich T, Fundamenski W, Huber A, Silva C and Tskhakaya D 2007 ELM transport in the JET scrape-off layer *Nucl. Fusion* **47** 1437–48

[86] Eich T, Andrew P, Herrmann A, Fundamenski W, Loarte A and Pitts R A 2007 ELM resolved energy distribution studies in the JET MKII Gas-Box divertor using infra-red thermography *Plasma Phys. Control. Fusion* **49** 573–604

[87] Eich T, Sieglin B, Scarabosio A, Fundamenski W, Goldston R J and Herrmann A 2011 Inter-ELM power decay length for JET and ASDEX Upgrade: Measurement and comparison with heuristic drift-based model *Phys. Rev. Lett.* **107**

[88] Kukushkin A S, Pacher H D, Pacher G W, Janeschitz G, Coster D, Loarte A and Reiter D 2003 Scaling laws for edge plasma parameters in ITER from two-dimensional edge modelling *Nucl. Fusion* **43** 716–23

[89] Pitts R A, Carpentier S, Escourbiac F, Hirai T, Komarov V, Kukushkin A S, Lisgo S, Loarte A, Merola M, Mitteau R, Raffray A R, Shimada M and Stangeby P C 2011 Physics basis and design of the ITER plasma-facing components *Journal of Nuclear Materials* vol 415

[90] Eich T, Sieglin B, Thornton A J, Faitsch M, Kirk A, Herrmann A and Suttrop W 2017 ELM divertor peak energy fluence scaling to ITER with data from JET, MAST and ASDEX upgrade *Nucl. Mater. Energy* **12** 84–90

[91] Gunn J P, Carpentier-Chouchana S, Dejarnac R, Escourbiac F, Hirai T, Komm M, Kukushkin A, Panayotis S and Pitts R A 2017 Ion orbit modelling of ELM heat loads on ITER divertor vertical targets *Nucl. Mater. Energy* **12** 75–83

[92] Loewenhoff T, Bürger A, Linke J, Pintsuk G, Schmidt A, Singheiser L and Thomser C 2011 Evolution of tungsten degradation under combined high cycle edge-localized mode and steady-state heat loads *Physica Scripta T* vol T145

[93] Kirk A, Dunai D, Dunne M, Huijsmans G, Pamela S, Becoulet M, Harrison J R, Hillesheim J, Roach C and Saarelma S 2014 Recent progress in understanding the processes underlying the triggering of and energy loss associated with type i ELMs *Nucl. Fusion* **54**

[94] Staebler G M and Hinton F L 1989 Currents in the scrape-off layer of diverted tokamaks *Nucl. Fusion* **29** 1820–4

[95] Hinton F L and Hazeltine R D 1976 Theory of plasma transport in toroidal confinement systems *Rev. Mod. Phys.* **48** 239–308

[96] Boedo J, McLean A G, Rudakov D L and Watkins J G 2018 A review of direct experimental measurements of detachment *Plasma Phys. Control. Fusion* **60**

[97] Stangeby P C 1990 Comment: Currents in the scrape-off layer of diverted tokamaks: Power to the divertor plates *Nucl. Fusion* **30** 1153–5

[98] Luxon J L 2002 A design retrospective of the DIII-D tokamak *Nucl. Fusion* **42** 614–33

[99] Aymar R, Barabaschi P and Shimomura Y 2002 The ITER design *Plasma Phys. Control. Fusion* **44** 519–65

[100] Schneider P A, Barrera Orte L, Burckhart A, Dunne M G, Fuchs C, Gude A, Kurzan B, Suttrop W and Wolfrum E 2015 Pedestal and edge localized mode characteristics with different first wall materials and nitrogen seeding in ASDEX Upgrade *Plasma Phys. Control. Fusion*

[101] Hutchinson I H, Boivin R, Bombarda F, Bonoli P, Fairfax S, Fiore C, Goetz J, Golovato S, Granetz R, Greenwald M, Horne S, Hubbard A, Irby J, LaBombard B, Lipschultz B, Marmar E, McCracken G, Porkolab M, Rice J, Snipes J, Takase Y, Terry J, Wolfe S, Christensen C, Garnier D, Graf M, Hsu T, Luke T, May M, Niemczewski A, Tinios G, Schachter J and Urbahn J 1994 First results from Alcator-C-MOD *Phys. Plasmas*

[102] Hughes J W, Snyder P B, Reinke M L, LaBombard B, Mordijck S, Scott S, Tolman E, Baek S G, Golfinopoulos T, Granetz R S, Greenwald M, Hubbard A E, Marmar E, Rice J E, White A E, Whyte D G, Wilks T and Wolfe S 2018 Access to pedestal pressure relevant to burning plasmas on the high magnetic field tokamak Alcator C-Mod *Nucl. Fusion* **58** 112003

[103] Strait E J 2006 Magnetic diagnostic system of the DIII-D tokamak *Rev. Sci. Instrum.*

[104] King J D, Strait E J, Boivin R L, Taussig D, Watkins M G, Hanson J M, Logan N C, Paz-Soldan C, Pace D C, Shiraki D, Lanctot M J, La Haye R J, Lao L L, Battaglia D J, Sontag A C, Haskey S R and Bak J G 2014 An upgrade of the magnetic diagnostic system of the diii-d tokamak for non-axisymmetric measurements *Rev. Sci. Instrum.*

[105] Holcomb C T, Makowski M A, Jayakumar R J, Allen S A, Ellis R M, Geer R, Behne D, Morris K L, Seppala L G and Moller J M 2006 Motional Stark effect diagnostic expansion on DIII-D for enhanced current and Er profile measurements *Review of Scientific Instruments*
[106] Hutchinson I H 2002 Principles of Plasma Diagnostics: Second Edition *Plasma Phys. Control. Fusion*
[107] Prunty S L 2014 A primer on the theory of Thomson scattering for high-temperature fusion plasmas *Phys. Scr.*
[108] Carlstrom T N, Campbell G L, DeBoo J C, Evanko R, Evans J, Greenfield C M, Haskovec J, Hsieh C L, McKee E, Snider R T, Stockdale R, Trost P K and Thomas M P 1992 Design and operation of the multipulse Thomson scattering diagnostic on DIII-D (invited) *Rev. Sci. Instrum.*
[109] Glass F, Carlstrom T N, Du D, McLean A G, Taussig D A and Boivin R L 2016 Upgraded divertor Thomson scattering system on DIII-D *Rev. Sci. Instrum.*
[110] Grierson B A, Burrell K H, Chrystal C, Groebner R J, Haskey S R and Kaplan D H 2016 High resolution main-ion charge exchange spectroscopy in the DIII-D H-mode pedestal *Rev. Sci. Instrum.*
[111] Haskey S R, Grierson B A, Stagner L, Chrystal C, Ashourvan A, Bortolon A, Boyer M D, Burrell K H, Collins C, Groebner R J, Kaplan D H and Pablant N A 2018 Active spectroscopy measurements of the deuterium temperature, rotation, and density from the core to scrape off layer on the DIII-D tokamak (invited) *Rev. Sci. Instrum.*
[112] Chrystal C, Burrell K H, Grierson B A, Haskey S R, Groebner R J, Kaplan D H and Briesemeister A 2016 Improved edge charge exchange recombination spectroscopy in DIII-D *Rev. Sci. Instrum.* **87** 11E512
[113] Planck M 1920 The Theory of Heat Radiation *Nature* **105** 228–228
[114] Sieglin B A 2014 Experimental investigation of heat transport and divertor loads of fusion plasmas in all metal ASDEX upgrade and JET
[115] Herrmann A, Junker W, Gunther K, Bosch S, Kaufmann M, Neuhauser J, Pautasso G, Richter T and Schneider R 1995 Energy flux to the ASDEX-Upgrade diverter plates determined by thermography and calorimetry *Plasma Phys. Control. Fusion* **37** 17–29
[116] Schaffer M J and Leikind B J 1991 Observation of electric currents in diverted tokamak scrape-off layers *Nucl. Fusion* **31** 1750–8
[117] Evans T E, Lasnier C J, Hill D N, Leonard A W, Fenstermacher M E, Petrie T W and Schaffer M J 1995 Measurements of non-axisymmetric effects in the DIII-D divertor *J. Nucl. Mater.* **220**–**222** 235–9
[118] Stillerman J A, Fredian T W, Klare K A and Manduchi G 1997 MDSplus data acquisition system *Rev. Sci. Instrum.* **68** 939–42
[119] Osborne T.H., Beurskens M.N.A., and JET-EFDA D-D and Contributors and I H P S G 2010 Scaling of H-mode Pedestal and ELM Characteristics in the JET and DIII-D Tokamaks *IAEA FEC EXC/2-1*
[120] Petty C C, Luce T C, Burrell K H, Chiu S C, DeGrassie J S, Forest C B, Gohil P, Greenfield C M, Groebner R J, Harvey R W, Pinsker R I, Prater R, Waltz R E, James R A and Wròblewski D 1995 Nondimensional transport scaling in DIII-D: Bohm versus gyro-Bohm resolved *Phys. Plasmas* **2** 2342–8
[121] Wang X, Mordijck S, Doyle E J, Rhodes T L, Zeng L, McKee G R, Austin M E, Meneghini O, Staebler G M and Smith S P 2017 Understanding ECH density pump-out in DIII-D H-mode plasmas *Nucl. Fusion* **57**

[122] Leonard A W, Mahdavi M A, Lasnier C J, Petrie T W and Stangeby P C 2012 Scaling radiative divertor solutions to high power in DIII-D *Nucl. Fusion* **52**
[123] Bortolon A, Maingi R, Mansfield D K, Nagy A, Roquemore A L, Baylor L R, Commaux N, Jackson G L, Gilson E P, Lunsford R, Parks P B, Chrystal C, Grierson B A, Groebner R, Haskey S R, Makowski M J, Lasnier C J, Nazikian R, Osborne T, Shiraki D and Van Zeeland M A 2016 High frequency pacing of edge localized modes by injection of lithium granules in DIII-D H-mode discharges *Nucl. Fusion* **56**
[124] Snyder P B, Osborne T H, Burrell K H, Groebner R J, Leonard A W, Nazikian R, Orlov D M, Schmitz O, Wade M R and Wilson H R 2012 The EPED pedestal model and edge localized mode-suppressed regimes: Studies of quiescent H-mode and development of a model for edge localized mode suppression via resonant magnetic perturbations *Phys. Plasmas* **19**
[125] Liang Y, Koslowski H R, Thomas P R, Nardon E, Alper B, Andrew P, Andrew Y, Arnoux G, Baranov Y, Bécoulet M, Beurskens M, Biewer T, Bigi M, Crombe K, De La Luna E, De Vries P, Fundamenski W, Gerasimov S, Giroud C, Gryaznevich M P, Hawkes N, Hotchin S, Howell D, Jachmich S, Kiptily V, Moreira L, Parail V, Pinches S D, Rachlew E and Zimmermann O 2007 Active control of type-I edge-localized modes with n=1 perturbation fields in the JET tokamak *Phys. Rev. Lett.* **98**
[126] Suttrop W, Eich T, Fuchs J C, Günter S, Janzer A, Herrmann A, Kallenbach A, Lang P T, Lunt T, Maraschek M, McDermott R M, Mlynek A, Pütterich T, Rott M, Vierle T, Wolfrum E, Yu Q, Zammuto I and Zohm H 2011 First observation of edge localized modes mitigation with resonant and nonresonant magnetic perturbations in ASDEX upgrade *Phys. Rev. Lett.* **106**
[127] Snyder P B, Wilson H R, Osborne T H and Leonard A W 2004 Characterization of peeling–ballooning stability limits on the pedestal *Plasma Phys. Control. Fusion* **46** A131–41
[128] Huijsmans G T A and Loarte A 2013 Non-linear MHD simulation of ELM energy deposition *Nucl. Fusion* **53**
[129] Hayashi N, Takizuka T, Aiba N, Oyama N, Ozeki T, Wiesen S and Parail V 2009 Integrated simulation of ELM energy loss and cycle in improved H-mode plasmas *Nucl. Fusion* **49** 095015
[130] Hayashi N, Oyama N, Takizuka T, Aiba N and Ozeki T 2011 Effect of core pressure gradient just inside the top of the pedestal on the energy loss due to the edge localized mode in JT-60U *Nucl. Fusion* **51** 073015
[131] Snyder P B, Groebner R J, Hughes J W, Osborne T H, Beurskens M, Leonard A W, Wilson H R and Xu X Q 2011 A first-principles predictive model of the pedestal height and width: Development, testing and ITER optimization with the EPED model *Nucl. Fusion* **51**
[132] Kallenbach A, Carlson A, Pautasso G, Peeters A, Seidel U and Zehrfeld H P 2001 Electric currents in the scrape-off layer in ASDEX Upgrade *J. Nucl. Mater.* **290–293** 639–43
[133] Petrie T W, Watkins J G, Lao L L and Snyder P B 2003 The role of magnetic geometry on the poloidal distribution of ELM-induced peak particle flux at the divertor targets in DIII-D *Nucl. Fusion*
[134] Leonard A W, Casper T A, Groebner R J, Osborne T H, Snyder P B and Thomas D M 2007 Pedestal performance dependence upon plasma shape in DIII-D *Nuclear Fusion* vol 47 pp 552–62

[135] Solomon W M, Burrell K H, Garofalo A M, Groebner R J, Lasnier C J, Makowski M A, Osborne T H, Reimerdes H, Degrassie J S, Doyle E J, Evans T E, Fenstermacher M E, Jackson G L and Schaffer M J 2012 ELM pacing using modulated non-axisymmetric magnetic fields on DIII-D *Nucl. Fusion* **52**

[136] Knolker M, Bortolon A, Canal G P, Evans T E, Zohm H, Abrams T, Buttery R J, Davis E M, Groebner R J, Hollmann E, Fenstermacher M E, Lasnier C, Leonard A W, Moyer R A, Nazikian R, Osborne T H, Paz-Soldan C and Sieglin B 2018 Investigation of the role of pedestal pressure and collisionality on type-I ELM divertor heat loads in DIII-D *Nucl. Fusion* **58** 096023

[137] Leonard A W 2014 Edge-localized-modes in tokamaksa) *Phys. Plasmas* **21** 090501

[138] Pitts R ., Alberti S, Blanchard P, Horacek J, Reimerdes H and Stangeby P . 2003 ELM driven divertor target currents on TCV *Nucl. Fusion* **43** 1145–66

[139] Takahashi H, Fredrickson E D, Schaffer M J, Austin M E, Evans T E, Lao L L and Watkins J G 2004 Observation of SOL current correlated with MHD activity in NBI heated DIII-D tokamak discharges *Nucl. Fusion* **44** 1075–96

[140] Takahashi H, Fredrickson E D and Schaffer M J 2008 Scrape-off-layer current model for filament structure observed during edge-localized modes in the DIII-D tokamak *Phys. Rev. Lett.* **100**

[141] Loarte A, Saibene G, Sartori R, Campbell D, Becoulet M, Horten L, Eich T, Herrmann A, Matthews G, Asakura N, Chankin A, Leonard A, Porter G, Federici G, Janeschitz G, Shimada M and Sugihara M 2003 Characteristics of type I ELM energy and particle losses in existing devices and their extrapolation to ITER *Plasma Phys. Control. Fusion* **45** 1549–69

[142] UZAWA K, ISHIZAWA A and NAKAJIMA N 2010 Intrinsic Rotation of a Magnetic Island with Finite Width *Plasma Fusion Res.* **5** S1016–S1016

[143] Wenninger R P, Zohm H, Boom J E, Burckhart A, Dunne M G, Dux R, Eich T, Fischer R, Fuchs C, Garcia-Munoz M, Igochine V, Hölzl M, N.c. L, Lunt T, Maraschek M, Müller H W, Park H K, Schneider P A, Sommer F, Suttrop W and Viezzer E 2012 Solitary magnetic perturbations at the ELM onset *Nucl. Fusion* **52**

[144] Sugiyama L E and Strauss H R 2010 Magnetic X-points, edge localized modes, and stochasticity *Phys. Plasmas* **17**

[145] Evans T E, Yu J H, Jakubowski M W, Schmitz O, Watkins J G and Moyer R A 2009 A conceptual model of the magnetic topology and nonlinear dynamics of ELMs *J. Nucl. Mater.* **390–391** 789–92

[146] Wingen A, Evans T E, Lasnier C J and Spatschek K H 2010 Numerical modeling of edge-localized-mode filaments on divertor plates based on thermoelectric currents *Phys. Rev. Lett.* **104**

[147] Wingen A, Evans T E and Spatschek K H 2009 High resolution numerical studies of separatrix splitting due to non-axisymmetric perturbation in DIII-D *Nucl. Fusion* **49**

[148] Evans T E, Moyer R A and Monat P 2002 Modeling of stochastic magnetic flux loss from the edge of a poloidally diverted tokamak *Phys. Plasmas* **9** 4957–67

[149] Roeder R K W, Rapoport B I and Evans T E 2003 Explicit calculations of homoclinic tangles in tokamaks *Phys. Plasmas*

[150] Evans T E, Roeder R K W, Carter J A and Rapoport B I 2004 Homoclinic tangles, bifurcations and edge stochasticity in diverted tokamaks *Contributions to Plasma Physics*

[151] Evans T E, Roeder R K W, Carter J A, Rapoport B I, Fenstermacher M E and Lasnier C J 2005 Experimental signatures of homoclinic tangles in poloidally diverted tokamaks *J. Phys. Conf. Ser.*

[152] Wingen A, Evans T E and Spatschek K H 2011 Effect of thermoelectric current splitting on the magnetic topology in DIII-D *Phys. Plasmas* **18**

[153] Moyer R A, Bykov I, Orlov D M, Evans T E, Lee J S, Teklu A M, Fenstermacher M E, Makowski M, Lasnier C J, Wang H Q, Watkins J G and Wu W 2018 Imaging divertor strike point splitting in RMP ELM suppression experiments in the DIII-D tokamak *Rev. Sci. Instrum.* **89** 10E106

[154] Kirk A, Koch B, Scannell R, Wilson H R, Counsell G, Dowling J, Herrmann A, Martin R and Walsh M 2006 Evolution of filament structures during edge-localized modes in the MAST tokamak *Phys. Rev. Lett.*

[155] Rack M, Wingen A, Liang Y, Spatschek K H, Harting D M and Devaux S 2012 Thermoelectric currents and their role during ELM formation in JET *Nucl. Fusion* **52**

[156] Wingen A, Ferraro N M, Shafer M W, Unterberg E A, Evans T E, Hillis D L and Snyder P B 2014 Impact of plasma response on plasma displacements in DIII-D during application of external 3D perturbations *Nucl. Fusion*

[157] Asdex Upgrade Team T, Faitsch M, Sieglin B, Eich T, Herrmann A and Suttrop W 2017 Divertor heat load in ASDEX Upgrade L-mode in presence of external magnetic perturbation *Plasma Phys. Control. Fusion* **59**

[158] Spolaore M, Kovařík K, Stöckel J, Adamek J, Dejarnac R, Ďuran I, Komm M, Markovic T, Martines E, Panek R, Seidl J and Vianello N 2017 Electromagnetic ELM and inter-ELM filaments detected in the COMPASS Scrape-Off Layer *Nucl. Mater. Energy* **12** 844–51

[159] Stangeby P C, Elder J D, McLean A G and Watkins J G 2017 Experimentally-based ExB drifts in the DIII-D divertor and SOL calculated from integration of Ohm's law using Thomson scattering measurements of Te and ne *Nucl. Mater. Energy* **12** 876–81

[160] Staebler G M 1996 The critical point for the onset of divertor energy flux asymmetry in tokamaks *Nucl. Fusion* **36** 1437–53

[161] Nunes I, Conway G D, Loarte A, Manso M, Serra F and Suttrop W 2004 Characterization of the density profile collapse of type I ELMs in ASDEX Upgrade with high temporal and spatial resolution reflectometry *Nucl. Fusion*

[162] Laggner F M, Wolfrum E, Cavedon M, Mink F, Viezzer E, Dunne M G, Manz P, Doerk H, Birkenmeier G, Fischer R, Fietz S, Maraschek M, Willensdorfer M and Aumayr F 2016 High frequency magnetic fluctuations correlated with the inter-ELM pedestal evolution in ASDEX Upgrade *Plasma Phys. Control. Fusion*

[163] Diallo A, Groebner R J, Rhodes T L, Battaglia D J, Smith D R, Osborne T H, Canik J M, Guttenfelder W and Snyder P B 2015 Correlations between quasi-coherent fluctuations and the pedestal evolution during the inter-edge localized modes phase on DIII-D *Phys. Plasmas*

[164] Kallenbach A, Dux R, Eich T, Fischer R, Giannone L, Harhausen J, Herrmann A, Müller H W, Pautasso G and Wischmeier M 2008 Divertor power and particle fluxes between and during type-I ELMs in the ASDEX Upgrade *Nuclear Fusion* vol 48

[165] Joseph I, Cohen R H and Ryutov D D 2009 Driving toroidally asymmetric current through the tokamak scrape-off layer. I. Potential for edge localized mode suppression *Physics of Plasmas* vol 16

[166] Schaffer M J, Mahdavi A, Klepper C C, Hill D N and Rensink M E 1992 Effect of divertor bias on plasma flow in the DIII-D scrape-off layer *Nucl. Fusion* **32** 855–61
[167] Zweben S J, Maqueda R J, Roquemore A L, Bush C E, Kaita R, Marsala R J, Raitses Y, Cohen R H and Ryutov D D 2009 Biased electrodes for SOL control in NSTX *J. Nucl. Mater.* **390–391** 417–20
[168] Zweben S J, Campanell M D, Lyons B C, Maqueda R J, Raitses Y, Roquemore A L, Scotti F and Takahashi H 2012 Local effects of biased electrodes in the divertor of NSTX *Plasma Phys. Control. Fusion* **54**
[169] Burrell K H, Osborne T H, Snyder P B, West W P, Fenstermacher M E, Groebner R J, Gohil P, Leonard A W and Solomon W M 2009 Quiescent H-mode plasmas with strong edge rotation in the cocurrent direction *Phys. Rev. Lett.*
[170] Lott F, Kirk A, Counsell G F, Dowling J, Taylor D, Eich T and Herrmann A 2005 Thermographic power accounting in MAST *Journal of Nuclear Materials*
[171] Sieglin B, Eich T, Scarabosio A, Arnoux G, Balboa I, Devaux S, Herrmann A, Hoppe F, Hölzl M, Kallenbach A, Lang P, Matthews G F, Marsen S, Pamela S, Rack M and Wenninger R 2013 Power load studies in JET and ASDEX-Upgrade with full-W divertors *Plasma Phys. Control. Fusion* **55**
[172] Abrams T, Unterberg E A, McLean A G, Rudakov D L, Wampler W R, Knolker M, Lasnier C, Leonard A W, Stangeby P C, Thomas D M and Wang H Q 2018 Experimental validation of a model for particle recycling and tungsten erosion during ELMs in the DIII-D divertor *Nucl. Mater. Energy* **17** 164–73
[173] Iglesias D, Bunting P, Esquembri S, Hollocombe J, Silburn S, Vitton-Mea L, Balboa I, Huber A, Matthews G F, Riccardo V, Rimini F and Valcarcel D 2017 Digital twin applications for the JET divertor *Fusion Eng. Des.*
[174] Oeffentlichkeitsarbeit M P I fuer 2004 Tokamak Scheme
[175] Zohm H and Wagner F 2010 Tokamaks *50 Jahre Forsch. für die Energ. der Zukunft* 26

List of Publications

Parts of this dissertation have been published as articles in the following journals (some of which were still in the review/submission process during the publication of this thesis) and as conference contributions:

Refereed Journals

[1] Knolker M, Bortolon A, Canal G P, Evans T E, Zohm H, Abrams T, Buttery R J, Davis E M, Groebner R J, Hollmann E, Fenstermacher M E, Lasnier C, Leonard A W, Moyer R A, Nazikian R, Osborne T H, Paz-Soldan C and Sieglin B 2018 Investigation of the role of pedestal pressure and collisionality on type-I ELM divertor heat loads in DIII-D Nucl. Fusion 58 096023

[2] Knolker M, Evans T E, Wingen A., Bortolon A, Chrystal C, Laggner F, Moyer R A, Nazikian R, Zohm H, Observation of Divertor Currents during type-I ELMs on the DIII-D tokamak, Nuclear Materials and Energy, Volume 18, 2019, Pages 222-226

[3] Knolker M, Evans T E, Wingen A., Bortolon A, Moyer R A, Nazikian R, Zohm H, ELM currents on DIII-D, internal review, to be submitted to Nuclear Fusion

Conferences

[1] Knolker M, Bortolon A, Evans T E, Leonard A W, Nazikian R, Zohm H, Test of the Eich model for ELM energy densities in DIII-D, 45th EPS 2018 Prague, July 2nd-6th 2018, O4.108

[2] Knolker M, Bortolon A, Canal G, Evans T, Abrams T, Leonard A, Nazikian R, Zohm H, Isolating the influence of pedestal pressure and collisionality on type-I ELM energy densities on DIII-D, 59th APS-DPP 2017, Milwaukee, October 23rd-27th, BO4.00006

[3] Knolker M, Bortolon A, Canal G, Diallo A., Evans T, Leonard A, Nazikian R, Zohm H, ELM heat flux scaling of the inner and outer divertor in DIII-D, ITPA SOL/Div, York, England, June 1st, 2017 – given by A.W. Leonard due to visa restrictions

[4] Knolker M, Ahn J, Bortolon A, Leonard A W, Nazikian R, Zohm H, The influence of pedestal parameters on ELM energies and heat fluxes for DIII-D, 58th APS-DPP 2016, San Jose, October 31st – November 4th, PP10.00066

[5] Knolker M, Evans T E, Wingen A., Bortolon A, Laggner F, Moyer R A, Nazikian R, Zohm H, Divertor current measurements during type I ELMs in DIII-D, PSI 2018 Princeton, July 2nd-6th, P51-11

Acknowledgement and disclaimer for publications

This thesis is based upon work supported by the U.S. Department of Energy, Office of Science, Office of Fusion Energy Sciences, under Award Numbers DE-FC02-04ER54698, DE-FG02-07ER54917 and DE-FG02-05ER54809. This research used resources of the DIII-D National Fusion Facility, which is a DOE Office of Science User Facility. I gratefully acknowledge the support of the DIII-D Team for tokamak, auxiliary heating, and diagnostic systems operation.

List of Figures